MECHANOTRANSDUCTION AND WATER TRANSPORT IN RAT PROXIMAL TUBULE

by

PENG GUO

A dissertation submitted to the Graduate Faculty in Engineering in partial fulfillment of the requirements for the degree of Doctor of Philosophy, The City University of New York

2003

UMI Number: 3103113

ProQuest Information and Learning Company
300 North Zeeb Road
P.O. Box 1346
Ann Arbor, MI 48106-1346

This manuscript has been read and accepted for the Graduate Faculty in Engineering in satisfaction of the dissertation requirement for the degree of Doctor of Philosophy.

9/15/03
Date

Dr. Sheldon Weinbaum

Chair of Examining Committee

9/15/2003
Date

Dr. Mumtaz Kassir

Executive Officer

Dr. Alan Weinstein

Dr. Stephen Cowin

Dr. David Rumschitzki

Dr. Bingmei Fu

Supervisory Committee

The City University of New York

Abstract

MECHANOTRANSDUCTION AND WATER TRANSPORT

IN RAT PROXIMAL TUBULE

by

Peng Guo

Mentor: Professor Sheldon Weinbaum, Co-mentor: Professor Alan Weinstein

Two long-standing mysteries in rat kidneys are explored in this dissertation: the afferent mechanism in glomerulotubular balance and the contribution of the paracellular pathway to the transepithelial water and solute transport. In the proximal tubule of rat kidneys, Na^+ and HCO_3^- reabsorption vary proportionally with changes in axial flow rate. This feature is a critical component of glomerulotubular balance, but the basic mechanism by which the tubule epithelial cells sense axial flow rate remains unexplained. We propose that the microvilli constituting the brush border in rat proximal tubule are physically suitable to sense the flow rate and translate this information into reabsorption. To examine this hypothesis quantitatively, we develop a hydrodynamic model to predict the force and torque distribution along a single microvillus and its resulting elastic bending deformation. This model predicts that the microvilli appear as a set of stiff bristles and are suitable to act as a mechanosensors of fluid flow and thus the afferent mechanosensory mechanism in glomerulotubular balance.

Water and solute traverse rat proximal tubule epithelium via both transcellular and paracellular routes. The tight junction (TJ) complex forms the major barrier in the paracellular route and its contribution to transepithelial water and solute transport has never been satisfactorily resolved. We first use a compartment model with revised parameter values to provide an estimation of the TJ water permeability and the TJ reflection coefficient for salts. A more general dual pathway model, large slit breaks formed by widely dispersed discontinuities and numerous small circular pores in the TJ strand, is then proposed for water and solute transport across the TJ strands. The dimensions of dual pathways are determined using the theoretically estimated values for the TJ water permeability and the TJ reflection coefficient for salts together with the TJ sucrose and NaCl permeability. It is predicted that the TJ water permeability is 21.2 percent of the transepithelial water permeability and that the small pores account for 91.2 percent of NaCl permeability, but only a few percent of the TJ water flux which crosses the TJ primarily through large slit breaks. The dimensions of dual pathways are consistent with the latest information on TJ ultrastructure.

天行健, 君子以自强不息;
地势坤, 君子以厚德载物.

<<易经·象>>

To my parents with respect and love

Acknowledgements

I would like to express my heartfelt gratitude to my mentor, Professor Sheldon Weinbaum, for his abundant encouragement, advice and patience, for always stimulating my confidence and providing me with an environment which allowed me to do research independently, for his leading me to enter biomedical engineering, an interdisciplinary and challenging field of research. I would like to express my deep-hearted thanks to my co-mentor, Professor Alan Weinstein, for his generous support and guidance and his clear and concise explanation of the problems in my research. I also want to thank Dr. Bingmei Fu for kind support.

I am also indebted to Professor Stephen C. Cowin, Professor Susannah P. Fritton, Professor Peter Ganatos, Professor David S. Rumschitzki, Professor Latif M. Jiji for their efforts to teach me a part of what they knew and for their clear and concise explanation of whatever questions I brought to them. I also want to thank Professor Andreas Acrivos for his wonderful teaching of fluid mechanics, to Dean Mumtaz Kassir for his kindly encouragement.

I am very grateful to Ms. Carol Bamberger and Dr. Laurent Mars for their unlimited help. I would like to thank my friends, You LD, Long X, Feng JJ, Liu JJ, Wu QH, Zhang XB, Xu SY and Wang LY for their helpful discussion in academic research. Without them, my life in New York City would be rather dull.

Finally, I wish to dedicate this work to my parents and my family for loving me unconditionally.

Contents

List of Tables

Chapter 2

Chapter 3

List of Figures

Chapter 1

Chapter 2

Chapter 3

Chapter 1 Physiological background

§ 1.1 Introduction to mammalian kidney

The major functions of the kidneys are regulation of body fluid osmolality and volume, regulation of electrolyte balance, regulation of acid-base balance, and the production and secretion of hormones. They also remove the metabolic end products, such as urea and urea acid, and preserve the substances essential to life, such as water, sugars, amino acids and electrolytes (sodium, potassium, bicarbonate and chloride). Thus, the kidneys are regulatory organs to maintain homeostasis in the body by regulating components of the interstitial fluid within a narrow range of values.

In mammalian animals, there are two kidneys. In human beings, the kidney is of the size of a tightly clenched fist and has a shape of a bean, see Fig.1.1. On the medial side of each kidney there is a small area where the renal artery, the renal vein and nerves enter into the kidney. This area is called the hilum. The hilum expands into a cavity called the renal sinus, which is filled with fat and connective tissue, where the renal pelvis is located at the center. Calyces extend to the renal pelvis from the kidney tissue. Those calyces, which directly open to the renal pelvis, are called major calyces. Minor calyces open to major calyces and extend to the kidney tissue.

A kidney can be divided into two parts. The outer part is the cortex and the inner part is the medulla. The medulla can be further divided into the outer medulla (the outer stripe and the inner stripe) and the inner medulla. The medulla consists of a number of renal pyramids which are cone-shaped structures. The bases of the pyramids extend into the cortex and form the medullary rays. The apex of each pyramid will project into the

medulla and empty into the opening of the minor calyx. The cortex can extend to the renal sinus between these pyramids. These extensions are called renal columns.

§ 1.2 Introduction to nephron and proximal tubule

§ 1.2.1 Nephron ultrastructure

The functional unit of the kidney is the nephron. Although there are two types of nephrons, superficial and juxtamedullary, their basic structures are similar, see Fig.1.2. They both have a renal corpuscle (glomerulus and Bowman's capsule), a proximal tubule, a Loop of Henle and a distal tubule. The distal tubule is open to the collecting duct which carries the urine to the calyces. The renal corpuscle, the convoluted proximal tubule and the distal tubule are in the cortex. The total length of a nephron varies from 50-55 mm. The nephron whose renal corpuscle is close to the medulla within the cortex is called the juxtamedullary nephron. This nephron has a longer Loop of Henle which extends further into the medulla than the superficial nephron, see Fig. 1.2. In human beings the ratio of these two nephrons is one to seven.

The glomerulus and the Bowman's capsule together are called the renal corpuscle. The inner layer of the Bowman's capsule (visceral layer) consists of specialized cells called podocytes. The outer layer of the Bowman's capsule is called the parietal layer consisting of a simple squamous epithelium. The glomerulus is supplied by an afferent arteriole and drained by an efferent arteriole. The glomerular capillaries are fenestrated and surrounded by a basement membrane and podocyte processes with gaps between them called filtration slits. The capillary endothelium, the basement membrane and the podocyte epithelium form the filtration barrier.

The focus of this dissertation is the relationship between structure and function as it relates to water and solute movement in rat proximal tubule epithelium. Thus, the ultrastructure of rat proximal tubule is described in detail in the following section.

§ 1.2.2 Proximal tubule ultrastructure

The proximal tubule starts from the cavity of the Bowman's capsule and ends at the descending thin limp of the loop of Henle. On average, the outer diameter of rat proximal tubule is about 45 μm and its entire length is 14mm or so. The cross section of the proximal tubule lumen is roughly a circle of 30 μm diameter. At the inner border there is a unique layer called the brush border where there are many projections called microvilli extending into the lumen, see Fig. 1.3. There is an abrupt transition in the cell structure between the Bowman's capsule and the proximal tubule. The outer layer of the Bowman's capsule (parietal layer) is comprised of a simple layer of squamous epithelium. The cells in the early part of the proximal tubule are cuboidal.

The proximal tubule can be divided into the convoluted part (the proximal convoluted tubule, PCT) and the straight part (the proximal straight tubule, PST). The PCT is located in the cortex and is more torturous while the PST is less convoluted and descends from the medulla ray to the outer stripe of the outer zone of the medulla. There are anatomical differences between these two parts and this transition often occurs at the beginning of the PST.

Segmentation

There are significant differences between the PCT and the PST. The cells in the PCT have a very complex shape and very extensive interdigitation whereas the cells in the PST are much simpler and have little or no interdigitation. The mammalian proximal

tubule, thus, can be further divided into three segments based on distinct differences of the PCT and the PST. The first segment (S1) comprises the beginning of the PCT, the second segment (S2) consists of the remaining portion of the PCT and the beginning of the PST and the third part (S3) the remainder of the PST.

Proximal Tubule Cells

In most adult mammalian animals the PCT epithelium consists of a single layer of cells. The difference in cell ultrastructure depends on species and segments. In rats, there is a single layer of highly polarized cuboidal cells in the epithelium of the PCT. On the luminal side there are many projections into the lumen. These projections are called microvilli and they form a specific layer called the brush border. One also finds occasional cilia, in general, less than one per cell. The basal membranes of the cells are anchored on the basement membrane. The height of the cells is 7-10 microns excluding the brush border. The number of cells in the S2 segment of the rabbit proximal tubule is estimated to be 300 per mm tubule (Welling et al., 1987).

The cell shape is very complex, see Fig 1.4. On the lumen side, there are many primary ridges and apical lateral processes. At the basal side the cells have many basal lateral processes and basal villi which interdigitate extensively between neighboring cells. The area amplification of the lateral cell membrane is nearly the same as that on the lumen side where the brush border provides a forty fold amplification in area of the apical membrane along the S2 segment of rabbit proximal tubule (Welling et al., 1987).

The mammalian proximal tubular epithelial cell has a large, round nucleus and there are abundant mitochondria at the basal side. These mitochondria have an orientation which is perpendicular to the basement membrane. There are many Na-K-ATPases on the

lateral cell membrane. These protein complexes actively transport intracellular sodium into the intercellular space under the presence of intercellular potassium and intracellular ATP. The mitochondria will supply energy to the active transporters.

Tight Junction

Neighboring cells in PCT are attached to each other through specialized intercellular contacts. In the mammalian proximal tubule, the intercellular contact can be divided into four kinds of specific junctions: the tight junction (TJ), the adherent belt, the desmosome and the gap junction. The TJ is the closest to the lumen side. It forms a continuous belt around the cell, seals the paracellular pathway and offers most of the resistance of the paracellular pathway. The structure-function correlation of the TJ is still not fully understood. In Chapter 3 an ultrastructural model is proposed for the tight junction strands using measured water and solutes permeabilities and the latest ultrastructural information on the TJ.

§ 1.2.3 Brush border in rat proximal tubule

On the lumen side of the proximal tubule epithelium there are numerous uniformly spaced microvilli which collectively constitute a layer named the brush border. The thickness of this layer varies from 2.5 micron in the S1 segment, 1.5 μm in the S2 segment and 3 μm in the S3 segment in the rat proximal tubule (Maunsbach and Christensen, 1992). The microvilli form a highly ordered hexagonal array, see Fig 1.5. The diameter of the microvilli is 75 nm and their gap is about 60-90 nm depending on the flow rate in the lumen (Maunsbach et al., 1987). The brush border greatly amplifies the apical surface area contributing to reabsorption. This area amplification is 40 in rat proximal tubule (Maunsbach, 1973).

In electron microscopic pictures, the apical cell membrane of microvilli appears to be a well-defined triple layered structure with an extracellular surface coat. This surface coat, called a glycocalyx, is intimately attached to the outside layer of the cell membrane. The total thickness of the three-layered membrane is 9 nm or so.

There are 6-10 long filaments in the cross-section of a micrvillus that are about 6-7 nm in diameter. These filaments were first observed by Hanssen and Hermann (1962). Later studies showed that these filaments were F-actin filaments (Bendayan, 1983). Two more cytoskeleton proteins, villin and fimbrin, can also be found in the microvilli (Rodman et al., 1986). These investigators also show that there is a very close correspondence between the structural components of the cytoskeleton of the brush border microvilli in the intestine and proximal tubule (Rodman et al., 1986). This organization is especially well characterized for the small intestine, see Fig. 1.6 adapted from Furukawa and Fechheimer (1997) and Mooseker and Tilney (1975). Fig 1.6 is a sketch of the detailed molecular structure of the intestinal microvilli. The cross-linking proteins that contribute to the bundle formation are villin and fimbrin, although fimbrin is less prominent in the kidney microvilli (Rodman et al., 1986). In the intestine the membrane of the microvillus is tethered to the actin bundle by a double helical spiral of protein linkages that have been identified as brush border myosin I (Louvard, 1989). These lateral myosin links on which the membrane rests are periodically spaced at 33 nm intervals along the outer filaments of the actin bundle and create a circular annulus of 20-30 nm thickness between actin filament bundle and the microvillus membrane (Mooseker and Tilney, 1975). These lateral linkages have not yet been identified for kidney microvilli. The actin filaments have a directionality with a barbed end at the apex and the

base that is attached to a terminal web of linker molecules. These linker molecules, tropomysin, fodrin and myosin II, attach the microvilli to a supporting structure of intermediate filaments and microtubules and also to actin filaments associated with the adherens junction. Rodman et al. (1986) have shown that this terminal web is a rather rigid structure that resists even harsh mechanical treatment. A tight junction near the apical margin provides for the polarity of the cell and separates the membrane proteins in the microvilli at the apical surface from those on the basolateral surfaces. In our mechanotransduction model in chapter two, we shall show that these longitudinal filaments offer a significant bending rigidity. A novel beam model is proposed for the rigidity and deflection of the microvilli from the first principles.

§ 1.2.4 Tight junction in rat proximal tubule

The ability to form different flow compartments is a characteristic of epithelia. Solutes, ions and water can move across epithelia through both transcellular and paracellular routes. Although transcellular transport is modulated by ion specific pumps and channels which create unique electroosmotic gradients, paracellular transport is mainly passive. The major barrier in the paracellular route is the tight junction (TJ). The ability of the TJ to seal the paracellular route between neighboring cells is variable and regulated.

A century ago this ability to seal the paracellular route was attributed to a "terminal bar". Electron microscopic images from early 1960 revealed that the terminal bar was composed of several morphologically distinct intercellular junctions. The tight junction is the most apical junction in this junctional complex. The adherent junction is adjacent to the tight junction and below them are desmosomes and gap junctions.

The tight junction has two major functions. First, it acts as a fence to separate proteins and lipid from diffusing freely inside the membrane and thus maintains the polarity of epithelial cells (fence function). Second, it forms a barrier for water and solutes to pass through the paracellular route (barrier function).

The transepithelial electrical resistance varies greatly depending on tissue and cell type. The transepithelial electrical resistance of the mammalian proximal tubule is 5-9 Ωcm^2 (Orci et al., 1981). The resistance of mammalian distal tubule is 350 Ωcm^2, while the value for toad bladder is 2800 Ωcm^2 (Orci et al., 1981; Claude, 1978). Based on the magnitude of the transepithelial electrical resistance, epithelia can be roughly divided into leaky and tight epithelia. The rat proximal tubule is considered quite leaky whereas the toad bladder is considered tight.

TJ Morphology in Electron Microscopic Pictures

In the 1960's the first major advances in TJ morphology were made due to the development of electron microscopic techniques. Basically, the tight junction is a complex of contact points where membrane proteins from neighboring cells adjoin at the apical end of the lateral space. The freeze-fracture images showed that the contact points were fibril-like rows forming a continuous branching network around the cell. There are obvious differences between very tight and very leaky epithelia (Claude and Goodenough, 1973). Very leaky epithelium, for instance the proximal convoluted tubule of rat kidneys as observed using the electron microscopic techniques, is shallow in the apical-basal direction and consists of a typically two-strand complex; occasionally, three strands are present. Vertical segments can be found between the strands and compartment-like structures are formed (Claude and Goodenough, 1973). These strands sometimes exhibit

discontinuities that occasionally exceed 1 micron in length (Orci et al., 1981), see Fig. 1.7. Through typical breaks is the length of one compartment ~ 0.2μm. Very tight epithelia, for instance the frog urinary bladder, have deep complexes along the apical-basal direction that consist of five or more strands (Claude and Goodenough, 1973).

Molecular Structure of the TJ

Our knowledge of the molecular structure of the TJ is still limited. In 1993 the first integral TJ protein was discovered (Furuse et al., 1993). This has led to rapid progress in unraveling the molecular structure of the TJ. Three types of integral proteins, JAM (Junction Adhesion Molecular), occludin and the claudin family, have been demonstrated to be involved in the structure and function of the TJ (Martin-Padura et al., 1998; Tsukita and Furuse, 1998; Tsukita and Furuse, 1999; Tsukita and Furuse, 2000).

Occludin, the first integral protein found in the TJ, is a protein which traverses the cell membrane four times (Furuse et al., 1993). Subsequent studies showed that occludin is a functional component of the TJ (McCarthy et al., 1996) and a possible determinant of the TJ permeability in endothelial cells (Hirase et al., 1997)

Later studies show that occludin is not the only integral protein constituting the TJ strands. When both alleles of the occludin gene in the embryonic stem cell are disrupted, well-developed TJ can be found between adjacent epithelial cells when the occludin-deficient ES cell were differentiated into epithelial cells by embryoid body formation (Saitou et al., 1998). This strongly implied that occludin was not necessarily required for the TJ formation and there were still unidentified TJ integral proteins which can form the TJ without occludin. Two novel integral proteins, claudin-1 and claudin-2, were then identified (Furuse et al., 1998A). Gradually, a number of proteins were found to be

involved in the formation of the TJ. They are now referred to as the claudin family (Heiskala et al., 2001; Morita et al., 1999).

More than 20 proteins have thus far been identified in the claudin family (Heiskala et al., 2001). Claudin-1 and claudin-2 are the first two proteins to be identified and of special interest in TJ formation (Furuse et al., 1998A). When the cDNAs of claudin-1 or claudin-2 genes were transfected into the mouse L fibroblasts lacking the TJ, well-developed TJ networks were found to be similar to the TJ strand network in situ in freeze-fracture replicas of the contact sites between cells (Furuse et al., 1998B). Thus, claudin-1 or claudin-2 can reconstitute the TJ through a homophilic interaction.

Since there are more than two claudins, one wishes to know whether these heterogeneous claudins form heteromeric TJ strands and whether claudins interact between each of the paired strands in a heterophilic manner. Indeed, claudin-1 and claudin-2 can form homopolymers in L-fibroblast transfectants and reconstitute the TJ strands in a homophilic interaction between the paired strands (Furuse et al., 1998B). In addition, distinct species of claudins can form TJ strands as heteropolymers (Furuse et al., 1999). Further, the claudin-3 strand can associate laterally with the claudin-1 or the claudin-2 strand to form paired strands, but the claudin-1 strand did not interact with the claudin-2 strand when two L filbroblasts singly expressing claudin-1, claudin-2 or claudin-3 were cocultured (Furuse et al., 1999). Thus, distinct species of claudins can interact with each other in a heterophilic manner between TJ strands in their lateral association (Furuse et al., 1999). In summary, claudins can form the paired strands in a head-to-head manner, homophilic or heterophilic, in these fibroblasts singly expressing one claudin. Claudins from one cell can form a strand in a side-by-side manner when two

types of claudins are contransfected into L fibroblast cells and form a network with the other strand from another cell. This model of assembly of claudins could increase the diversity of the structure and function of the TJ strands. Interestingly, claudin-1 and claudin-2 do not interact between paired strands (Furuse et al., 1999).

Not only can claudins form the TJ strands but they can also form specific channels in the TJ. It is demonstrated that claudin-16 (paracellin-1) can form channels for the uptake Mg^{2+} in the ascending limp of the Loop of Henle (Simon et al., 1999).

Claudins in Proximal Tubule

It is hypothesized that the distributions of different claudins account for the diversity of the TJ properties. For example, claudin-1 and claudin-4 are found to be abundant in MDCK-I cells which have a very tight junction while claudin-2 expression is restricted to MDCK-II cells which have a much leakier TJ than MDCK-I cells (Furuse et al., 2001). When claudin-2 was introduced into MDCK-1 cells, a conversion of the TJ from a very tight type to a leaky one was observed (Furuse et al., 2001). It is likely that the introduced claudin-2 with claudin-1 in the TJ strands facilities the transport of water and ions because claudin-1 strand and claudin-2 strand from two L fibroblasts can not form paired strands (Furuse et al., 1999). In rat proximal tubule, it is found that claudin-2 exists throughout the proximal tubule and in a contiguous early segment of the thin descending limb of long-looped nephrons in mouse kidneys (Enck et al., 2001). Thus, it is likely that claudin-2 is responsible for the leakiness of the TJ in rat proximal tubule.

The integral proteins in the TJ interact with the peripheral membrane proteins in the plasma, including actin filament (F-actin)-directly binding scaffold proteins (ZO-1, -2, and -3) (Fanning et al., 1999), non-actin filament-binding scaffold proteins (MAGI-1)

(Patrie et al., 2002), and cell polarity molecules (ASIP/PAR-3 and PAR-6) (Ebnet et al., 2001; Gao et al., 2002). The TJ morphology and function can be affected by the cytoskeleton and many physiological factors, such as extracellular Ca^{2+} (Ma et al., 2000B), kinases (Walsh et al., 2001), cytochalasin B (Ma et al., 2000A), cytokines (Walsh et al., 2000) via the interactions between the integral proteins and the peripheral proteins.

§ 1.3 Glomerulotubular balance and its possible underlying mechanism

§ 1.3.1 Ultrafiltration in the glomerulus

The formation of urine begins with the filtration of plasma water and its nonprotein components from the glomerular capillaries into the Bowman's capsule. This filtration is an ultrafiltration, i.e., the blood cells and protein macromolecules remain in the blood because they can hardly traverse the walls of the filtration barrier. In fact, very little protein is filtered and what is filtered can be reabsorbed afterward. This ultrafiltration is demonstrated by the micropipette experiment in which the filtrate in the Bowman's capsule was collected and carefully analyzed. The collected fluid contains nearly no protein and has approximately the same composition as plasma in respect to glucose, electrical conductance, osmolality, pH value and other solutes.

The filtration barrier in the glomerulus is comprised of the capillary endothelium, the basement membrane and the epithelium formed by a layer of highly specialized cells called podocytes. The capillary endothelium is very leaky and has a larger filtration coefficient than the extrarenal capillaries. Microscopic observations show that there are many fenetrae in the endothelium with a diameter of 70-100nm. These fenetrae are

covered by bush like filamentous structures (Rostgaard and Qvortrup, 1997). The basement membrane consists of three filamentous layers, *lamina rara interna, lamina densa and lamina rara externa.* The first and third of these layers are fused with the capillary endothelium and the podocyte epithelium. The epithelium attaches to the basement membrane by foot processes. Adjacent foot processes are separated by filtration slits of 25-60 nm in size. The filtration slits are bridged by thin diaphragms which appear to have small interstices of 7×14 nm in dimension. The detailed structure of the filtration slits is still under debate (Edwards et al., 1997).

Starling forces are the most important determinants of glomerular ultrafiltration. At normal flow conditions the hydrodynamic pressure in the capillary, 60 mmHg, is higher than the hydrodynamic pressure in the Bowman's capsule, 20 mmHg. The oncotic pressure in the capillary is 30 mmHg, whereas the oncotic pressure in the Bowman's capsule is zero because very little albumin can filter across the glomerulus filtration barrier. The net filtration pressure, thus, is 10 mmHg. This net filtration pressure can vary from 4 to 12 mmHg as the flow is up or down regulated.

For a single nephron the filtration rate varies typically from 15nl/min-60nl/min. Assume that the average filtration rate of one nephron is 30 nl/min and there are 1 million nephrons in one kidney working simultaneously, the total filtration rate of the two kidneys is 86.4 liters per day. The total volume excreted out of body is 1 litre per day. Thus, most of the filtrate is reabsorbed.

§ 1.3.2 Reabsorption in proximal tubule

Reabsorption occurs along the entire tubular system. Generally speaking, reabsorption helps the preservation of the substances which are essential to normal

functions, e.g., water, glucose and other sugars, amino acids and electrolytes. Many of these substances such as glucose and amino acids are primarily reabsorbed in the proximal tubule whereas others, such as water and sodium, are also reabsorbed in the more distal tubules of the nephron.

The most obvious examples of the reabsorbed substances are water, sodium, chloride and bicarbonate. For these substances more than 99 percent of the filtered load is reabsorbed. Glucose is another example. Glucose can filter freely across the glomerular filtration barrier and appears in the Bowman's capsule at the same concentration as that in plasma. The fact that there is nearly no glucose in the urine indicates that glucose must be reabsorbed. Micropuncture studies show that more than 99 percent of the filtered glucose is reabsorbed in the proximal tubule and nearly all of this occurs in the first half of the proximal tubule. This reabsorption of glucose in the proximal tubule is against the concentration gradient and involves a sodium-cotransporter protein that mediates secondary active transport.

Water can be reabsorbed along the entire tubule. In the proximal tubule nearly 2/3 to 3/4 of the filtered volume is reabsorbed and this fraction is constantly maintained in the physiological range of the filtration rate. This constant reabsorption is called glomerulotubular balance. It is one of the most important mysteries unsolved in kidney function. In Chapter 2 a new hypothesis is proposed that the microvilli in the brush border serve as the afferent mechanosensors in glomerulotubular balance. An elastohydrodynamic mathematical model is presented to quantitatively examine this hypothesis.

§ 1.3.3 Glomerulotubular balance

It has been known for more than three decades that the reabsorption rate is proportional to the filtration rate. This linear relation between the glomerular filtration rate and the reabsorption rate in the proximal tubule is called "glomerotubular balance". Schnermann et al. (1968) first demonstrated this in rats using the micropuncture technique. Their classical experimental result is shown in Fig. 1.8.

In Fig. 1.8 inulin is used as the marker molecule. Inulin is small in size and it is neutral. Thus, it can freely filter into the Bowman's capsule from the glomerular capillaries. In addition, it can be neither reabsorbed nor secreted and its absolute amount will not change along the tubule. If the concentration of inulin in some part of the tubule is more than that in plasma, some volume must be absorbed. The reabsorption fraction can be obtained in term of the ratio of these two concentrations in the tubule and in the plasma. Let r denote the ratio of C_{PT}, the inulin concentration at the end of the proximal tubule, to C_{PL}, the inulin concentration in plasma,

$$r = \frac{C_{PT}}{C_{PL}}. \tag{1.1}$$

The reabsorption ratio κ can be expressed in term of r.

$$\kappa = 1 - \frac{1}{r}. \tag{1.2}$$

In their experiment, Schnermann et al. (1968) found that the ratio r remained the same despite the four fold increase in glomerular filtration rate. This ratio is 2.27 and the corresponding fractional reabsorption rate is 56 percent.

Many factors may attribute to this balance. To name one, is the peritubular oncotic force. It is shown that in order to achieve a perfect glomerulotubular balance there must be a mechanism by which alteration in plasma flow, independent on

peritubular Starling forces, can influence proximal reabsorption (Weinstein, 1992). The impact of the changes in plasma flow in the lumen of the proximal tubule has been approached by examination of the effect of the luminal flow rate on the tubular reabsorption. When one talks about the perfusion and the reabsorption in the proximal tubule, it is "perfusion-reabsorption" balance.

§ 1.3.4 Perfusion-reabsorption balance and flow-dependent reabsorption

In fact, experiments show that the flow rate does regulate the reabsorption of glucose, amino acids, bicarbonate and other ions (Liu et al., 1988; Wong et al., 1995; Alpern et al., 1983). The flow rate is also shown to regulate the transporter activity in the lumen (Preisig, 1992)

§ 1.3.5 Possible underlying mechanisms

Three possible underlying mechanisms may contribute to the "perfusion-reabsorption" balance. The first is unstirred layer effects.

1) Unstirred layer

One hypothesized mechanism for the flow-dependent reabsorption is the possible existence of an unstirred layer. In this hypothesis there is a concentration gradient in the brush border which will drive the passive osmotic volume flow. The experiment in Basmadjian et al. (1980) showed that this effect was unlikely because they found that the flow rate in the brush border is 10^{-4} of the flow rate in the lumen. Thus, diffusion is dominant in the brush border.

2) Shear stress

Another possible mechanism is shear flow induced mechanotransduction. Shear stress is widely recognized to induce NO release, Ca^{++} transients and vascular remodeling

in vascular endothelium (Lehoux et al. 2002). However, in the brush border of the proximal tubule, the microvilli are densely packed and, thus, it is reasonable to conclude that the magnitude of the shear stress at the base of the brush border is insignificant compared to the shear stress present in capillaries.

3) Microvilli as mechanosensors - our new hypothesis

Another candidate for the mechanotransduction mechanism is that the microvilli themselves act as the mechanotransducers. This hypothesis will be quantitatively examined in Chapter 2. We shall also examine in our model the magnitude of the shear stress at the base of the brush border.

§ 1.4 Water and solute transport across rat PCT

Although much progress has been made in respect to the molecular structure of the TJ, our knowledge of the TJ as a transport barrier is still inadequate and rather controversial. In fact, there is still a long controversy as to how much the paracellular pathway contributes to the transepithelial water transport in rat proximal tubule. Before this problem is explored, one needs to know the possible transport routes across epithelia.

§ 1.4.1 Transcellular and paracellular routes

The rat proximal tubule epithelium is a very leaky epithelium. Water and solutes can traverse rat proximal tubule via both transcellular and paracellular routes, see Fig. 1.9. In the transcellular route, water and solutes first traverse the apical cell membrane, cross the cytoplasma and leave the cell via either the intercellular space through the lateral cell membrane or the basal cell membrane and then enter the interstitium after crossing the basement membrane. In the paracellular route, water and solutes first traverse the tight

junction complex, enter the intercellular space and then cross the basement membrane. It is not clear what fraction of water and solute is reabsorbed via the transcellular route and what fraction is reabsorbed via the paracellular route. In Chapter 3 a compartment model and a new dual pore-slit model are combined to predict the TJ water permeability and the contribution of the paracellular route to the transepithelial water transport.

Transcellular and paracellular routes differ greatly for water and solute passage. The transcellular route is regulated by functionally distinct transporters and channels. For example, water can traverse the apical cell membrane via water channels formed by aquaporins (Kwon et al., 2001). This water channel has little capacity to allow for the passage of small ions. Sodium can traverse the apical cell membrane via sodium-hydrogen transporters (Vallon et al., 2000). Intracellular sodium is depleted via the Na-K-ATPases on the lateral cell membrane. In contrast, the paracellular route is a passive pathway. Neutral molecules are transported via the paracellular pathway following their chemical gradient, while ions follow the electrical-chemical potential gradient established by active transport. The paracellular pathway lacks the diversity and molecular discrimination of the transcellular pathway.

§ 1.4.2 Intercellular space

In rat proximal tubule the intercellular space starts from the tight junction and ends at the basement membrane and, thus, has a depth similar to the height of the cells. The width of the intercellular space varies along the lateral space and is dependent on the osmotic water flow and the intercellular hydrostatic pressure. Osmotic water flow in the direction from lumen to peritubular space causes significant dilation of the lateral intercellular space in proximal tubule. Osmotic water flow from the peritubular space to

the lumen causes a significant decrease in the width of the lateral intercellular space. Augmented water flow into the intercellular space causes a pressure increase in the space and greatly expands the lateral intercellular space. Increased luminal osmotic pressure removes water from the lateral space and thus collapses the spaces.

Transport across rat proximal tubule is nearly iso-osmotic. Iso-osmotic water reabsorption by an epithelium can be explained by intraepithelial osmosis secondary to active transport of sodium. Curran and MacIntosh (1962) first suggested a three-compartment model to describe iso-osmotic transport. The lateral intercellular space represents the intraepithelial middle compartment and the site of the solute-solvent coupling (Diamond, 1964). In this study, a compartment model is applied to describe the transport across rat proximal tubule and to provide an estimation of the water permeability of the TJ. In this model the lateral intercellular space is a well-stirred compartment bounded by a basement membrane and a composite luminal barrier consisting of the cell barrier and the TJ barrier (Weinstein, 1984).

§ 1.4.3 The TJ permeability

The transepithelial electrical resistance (TER) of various epithelia has been measured and it was found that there were two types of epithelia, tight epithelia such as toad bladder and toad skin, and leaky epithelia such as proximal tubule and small intestine. As noted earlier, there are typically two tight junction strands in leaky epithelia and five or more in tight epithelia (Claude and Goodenough, 1973). Claude (1978) hypothesized that the transepithelial electrical resistance was related to the number of strands in the TJ. He proposed an empirical correlation between the number of strands and the TER. This correlation is the following:

$$R = R_{min} \times p^{-n} \quad (1.3)$$

Here R is the transepithelial electrical resistance of the tight junction, R_{min} is the minimum resistance without any strands in the tight junction, n is the number of junctional strands, and p is a constant whose value, 0.426, is obtained by curve fitting the data. The relation between TER and the number of strands is nonlinear. One possible interpretation of this data is that there are small pores in the tight junction strands which flicker open or closed in a dynamical manner (Claude, 1978). However, this pore pathway is largely a conjecture until the integral proteins in the TJ were identified and the interaction of the TJ integral proteins was revealed (Furuse et al., 1999; Tsukita and Furuse, 2000). In Chapter 3 a dual pathway model comprised of infrequent large slit breaks and numerous small circular pores is proposed to model the TJ strands. The possible formation of the small pores is also discussed.

The contribution of the paracellular pathway to the transepithelial water transport in rat proximal tubule is rather controversial. Preisig and Berry (1985) suggested by indirect nonelectrolyte-permeable pore flux measurement that the osmotic water permeability of the nonelectrolyte-permeable pathway within the paracellular route is less than 2% of the transepithelial osmotic water permeability. Weinstein (1984) argued that the water permeability of the TJ was required to be of the same order as that of the transcellular route to satisfy the measured transepithelial reflection coefficient for NaCl. In Chapter 3 a compartment model with revised parameter values is used to provide a new estimate of the TJ water permeability in the paracellular route.

§ 1.5 Brief introduction to researches in Chapter 2 and 3

In Chapters 2 and 3 we will explore two long standing mysteries: the afferent mechanism in glomerulotubular balance and the contribution of the paracellular route to the transepithelial water permeability. In Chapter 2, we hypothesize that the microvilli constituting the brush border are suitable to sense the flow rate and translate this information into reabsorption. Thus, microvilli are capable to act as mechanotransducers and serve as the afferent mechanism in glomerulotubular balance. In Chapter 3 we use a compartment model with revised parameter values to describe rat proximal tubule epithelium and predict the water permeability of the TJ. We find that the water permeability of the TJ is 21.2 percent of the transepithelial water permeability. In addition, we propose a dual pore/slit model for the ultrastructure of the TJ strands which comprises of large slit breaks and small circular pores. The dimensions of the large slit breaks and small circular pores are then determined by the estimated TJ water permeability, the measured TJ solute permeability and the overall transepithelial reflection coefficient for NaCl. We find that the dual pathway model is more realistic and fits conceptually into recent updated views of the molecular structure of the TJ strands and the junction particle patterns observed in freeze-fracture electron micrograph studies of the TJ complex.

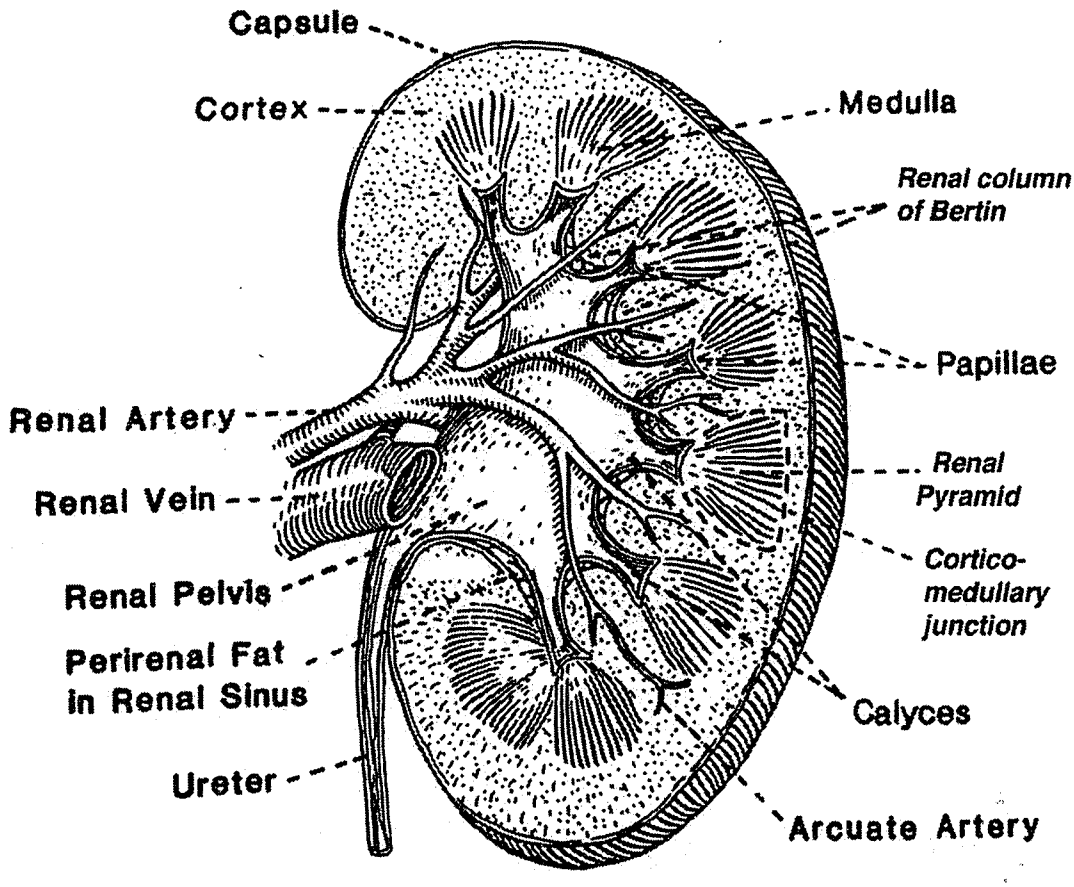

Figure 1.1 Diagram of human kidney.

From

http://membranebiology.mgh.harvard.edu/KidneyImages/Kidneyanatomy/HumanKidney.html

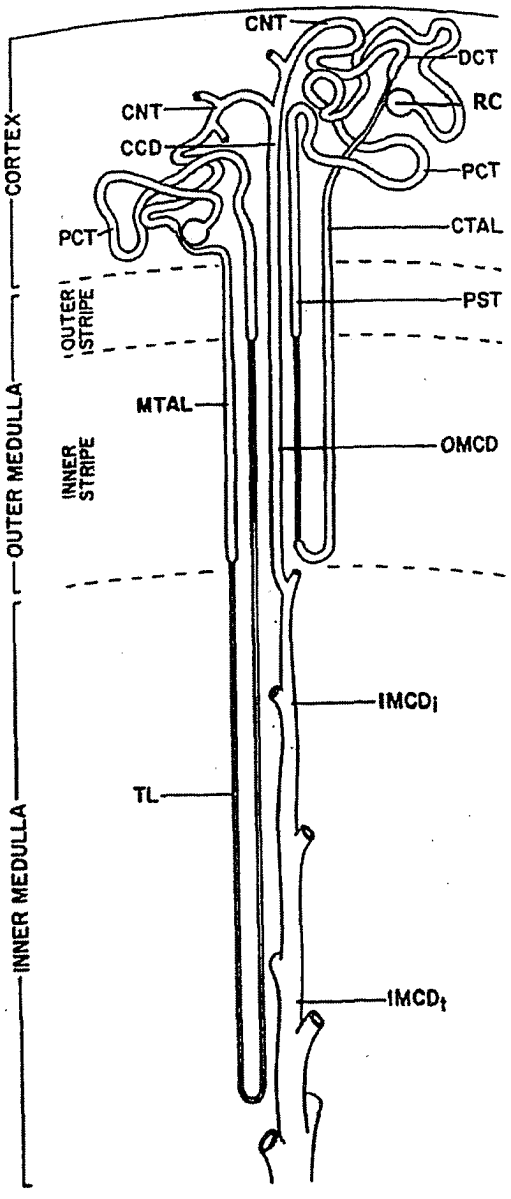

Abbreviation:

RC, Renal Corpuscle;

PCT, Proximal tubule S1 and S2 segments;

CTAL, Cortical thick ascending limb of Henle;

DCT, Distal convoluted tubule;

CNT, Connecting tubule;

CCD, Cortical collecting duct;

PST, Proximal tubule S3 segment;

OMCD, Outer medullary collecting duct;

MTAL, Medullary thick ascending limb of Henle;

OMCD, Outer medullary collecting duct;

IMCDi, IMCDt, Inner medullary collecting duct (initial portion and terminal portion);

TL, Thin ascending limb of Henle.

Figure 1.2 The ultrastructure of the nephrons and the distribution of urinary tubule segments in kidney. From: http://membranebiology.mgh.harvard.edu/KidneyImages/Kidneyanatomy/NephronDiagram.html.

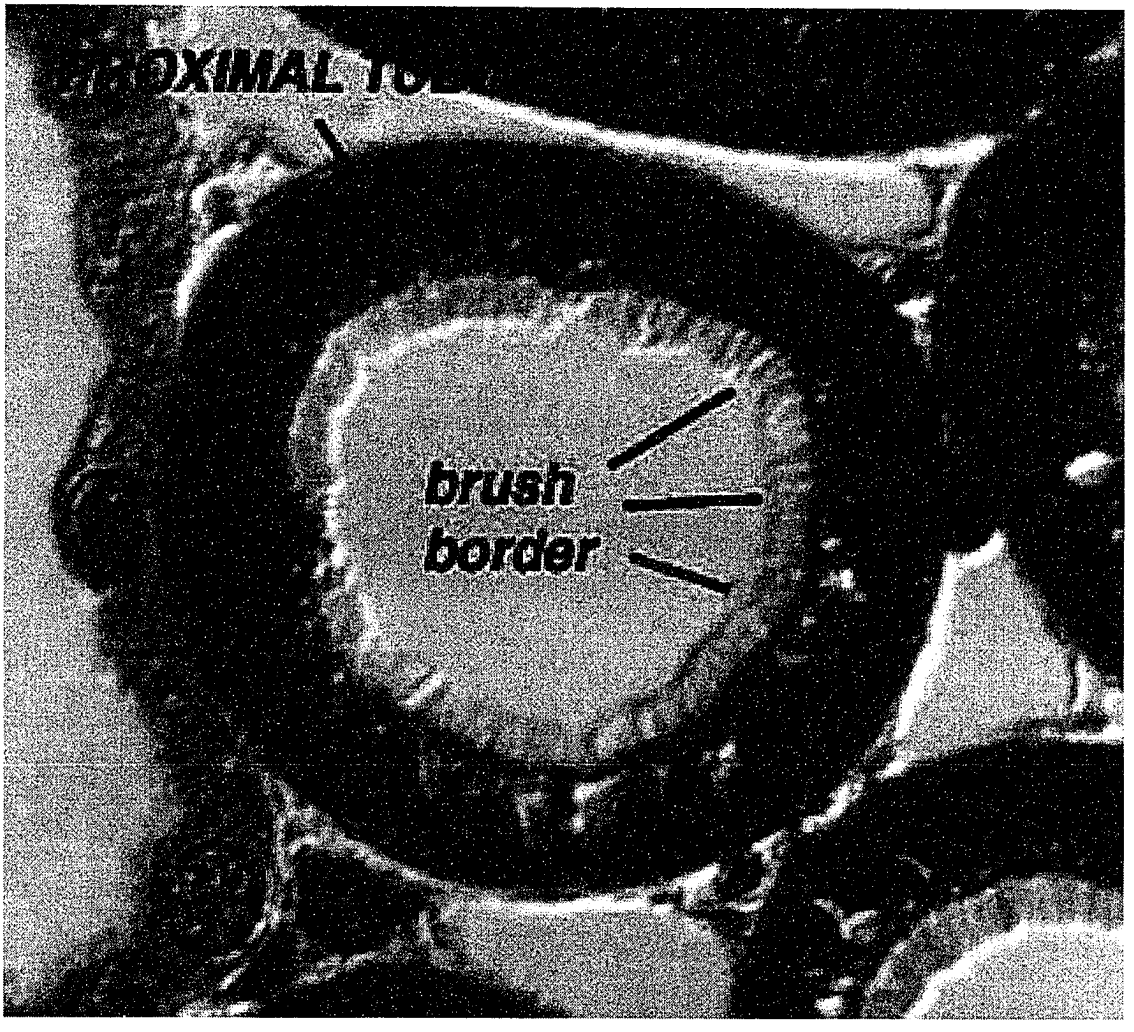

Figure 1.3 Electron microscopic picture of the cross-section of the S1 segment of the proximal tubule. The tubule lumen is roughly a circle. There are many projections into the lumen called microvilli. These apical microvilli are arranged into an elaborate brush border to increase membrane area for reabsorption. In this thesis, these microvilli are also viewed as mechanotransducers. From http://membranebiology.mgh.harvard.edu/KidneyImages/Kidneyanatomy/ProximalTubuleS1.html.

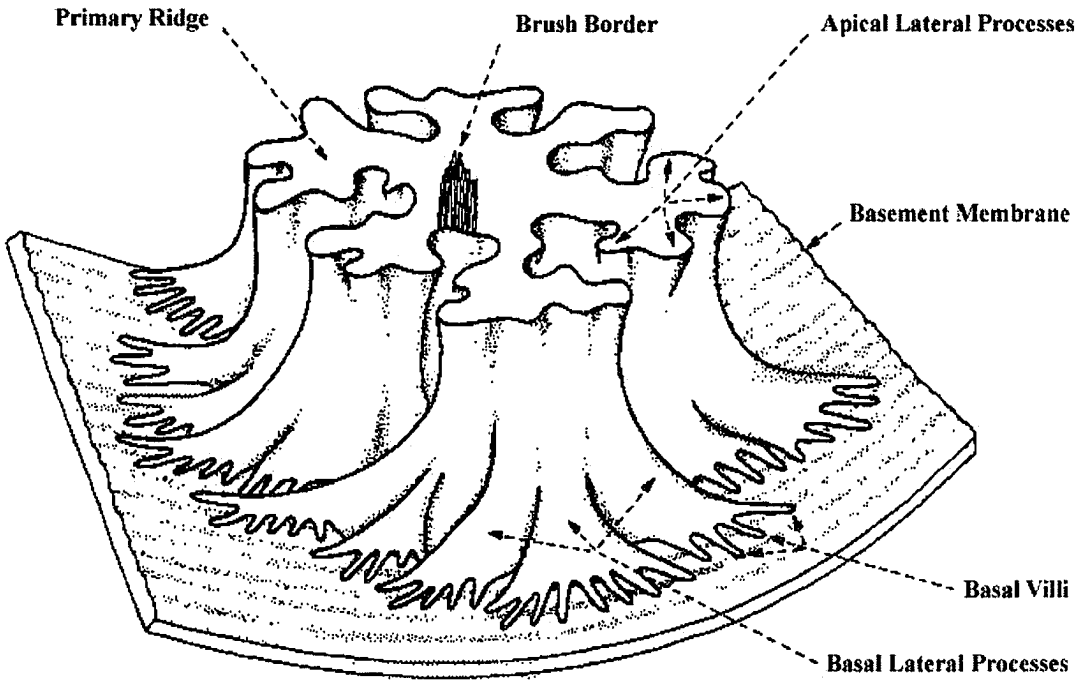

Figure 1.4 Diagram of three-dimensional appearance of a typical cell from the convoluted part of rat proximal tubule. In this diagram, only a small part of the brush border is shown. There are many primary ridges and apical lateral processes in the lumen side. There are basolateral processes and basal villi at the base of the cell. There is a transition from apical type to basal type channels appearing to be complete within the most basal 10-15 percent of the cell height. Note that the cell boundary at the apical side is very torturous. From Maunsbach and Christensen, 1992.

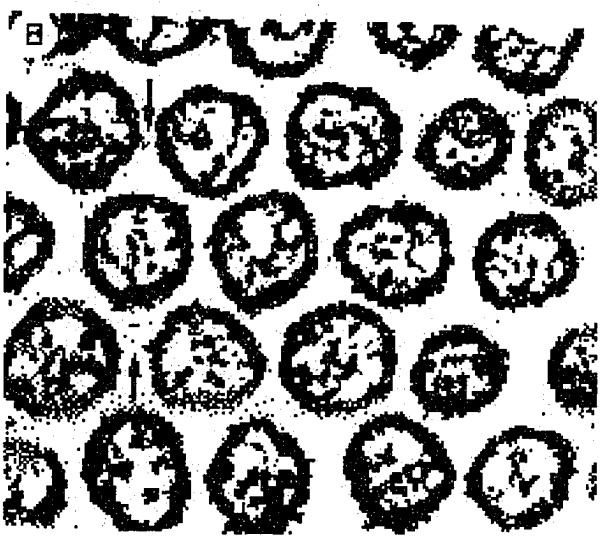

Figure 1.5 Electron microscopic picture of the cross-section of microvilli in brush border from cells in the convoluted part of rat proximal tubule. The microvilli form a hexagon array. The plasma membrane of microvilli is triple-layered with irregular cell coat attached to the outer leaflet. The thin filaments present in the microvilli are F-actin filaments. There are 6-10 F-actin filaments of diameter 6-7 nm. From Maunsbach and Christensen, 1992.

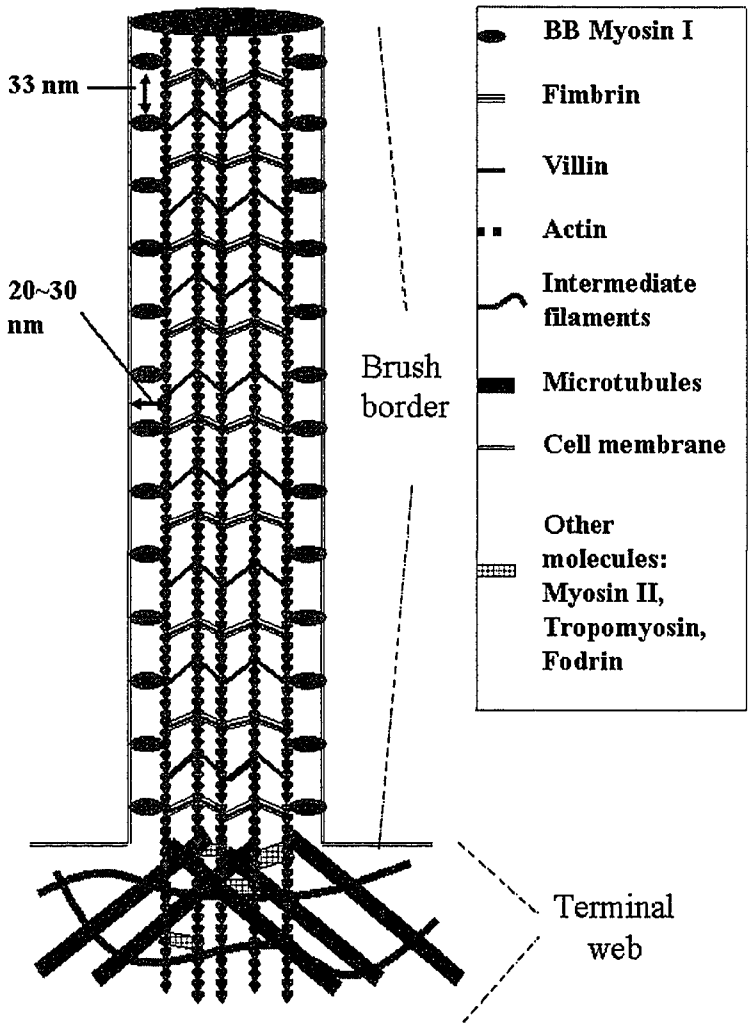

Figure 1.6 Sketch of the cytoskeleton inside an intestinal microvillus. The microvillus is rooted in the terminal web. The ultrastructure of the microvillus in rat proximal tubule is similar to that of the intestinal microvillus. From Weinbaum et al., 2001.

Figure 1.7 Freeze-fracture electron microscopic pictures of the tight junction in rat proximal tubule. (A) The luminal and lateral cell membranes of an epithelial cell from proximal tubule are separated by the tight junction. The tight junction fibrils are arranged in a parallel or a honeycomb pattern. It consists of a typically two-strand complex, occasionally three strands are present. Vertical segments can be found between the strand and compartment-like structure is formed. (B) The tight junction appearance under saline load. There is a decrease in the complexity of the strands. (C) E-face of the tight junction during saline load. Large slit breaks in the strands are apparent whose size is of 200 nm. From Orci et al., 1981.

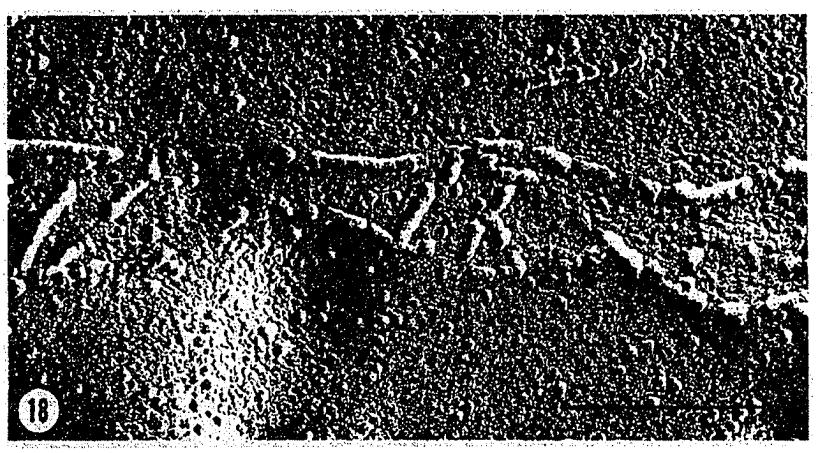

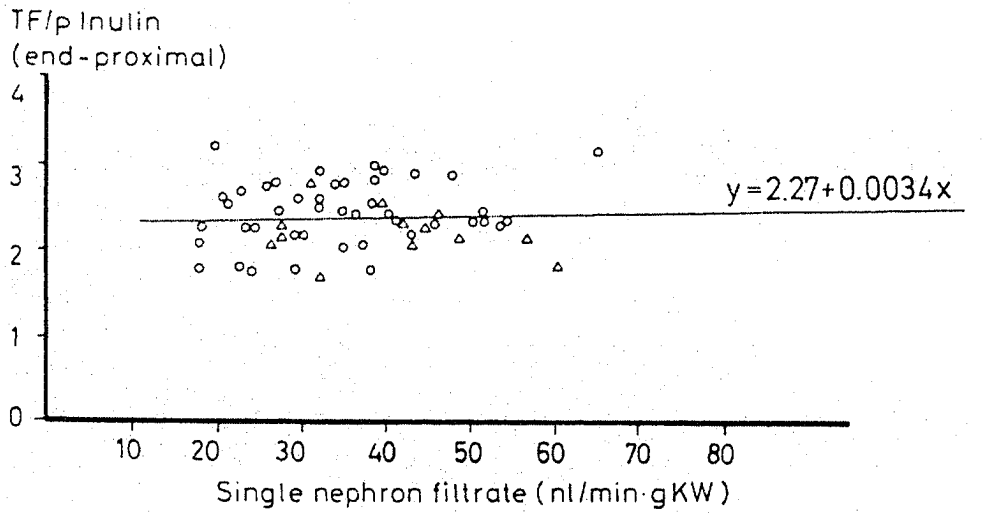

Figure 1.8 Experimental result in Schnermann et al. (1968). The ratio of inulin concentration between the end of the proximal tubule and the plasma is nearly a constant, 2.27, despite the three time increase in the single nephron filtration rate. The corresponding reabsorption rate is 58 percent. From Weinstein, 1992.

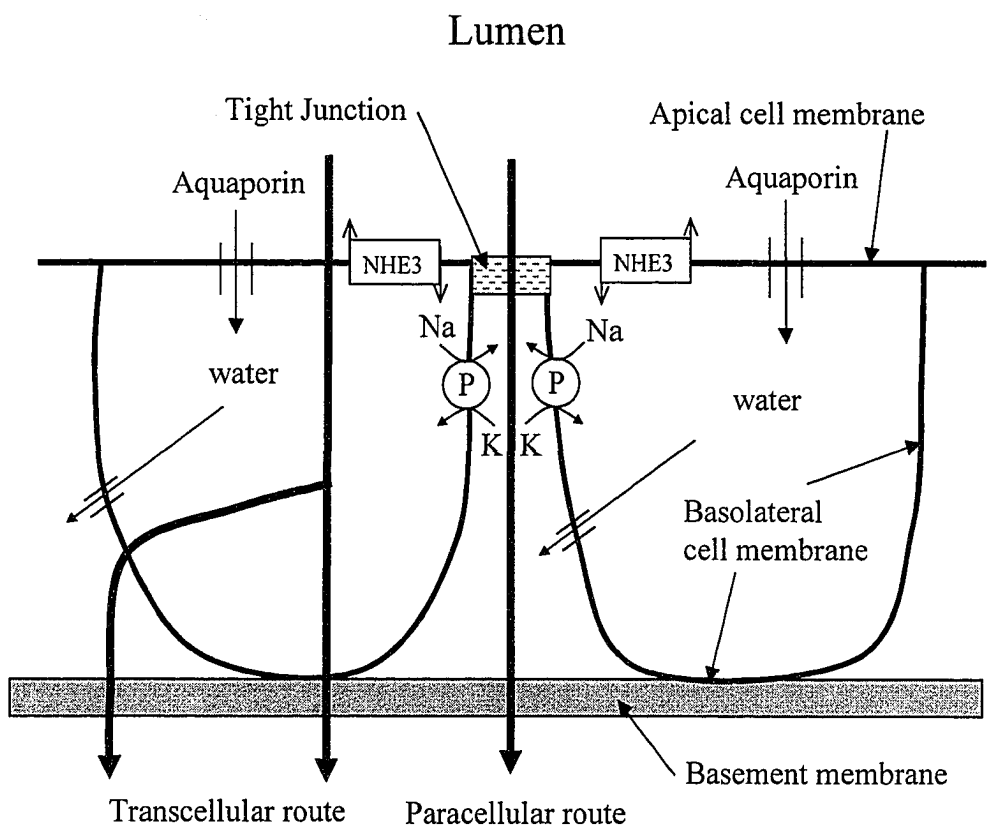

Figure 1.9 Diagram of transcellular and paracellular routes in rat proximal tubule. In the transcellular route water can transport across both the apical cell membrane and the basolateral cell membrane via aquaporins. Most of sodium (Na) transport across the apical membrane is via the sodium-hydrogen transporters (NHE3). Intracellular sodium is depleted via the sodium-potassium pumps (P) on the basolateral cell membrane under the presence of intercellular potassium (K).

Chapter 2 Mechanotransduction in rat proximal tubule

§ 2.1 Introduction

Perhaps the most important characteristic of solute and water transport in the proximal tubule is the observation that reabsorption varies proportionally with delivered load, i.e. with the glomerular filtration rate (Gertz and Boylan, 1973). In large measure this "glomerulotubular balance" derives from a "perfusion-absorption balance", that is, the capability of the proximal tubule epithelial cells to sense changes in luminal flow rate, and translate this signal into changes in volume reabsorption (Wilcox and Baylis, 1985). This system is remarkably precise, since the fraction of filtered fluid reabsorbed by the proximal tubule is nearly constant over the entire physiological range of flow (Schnermann et al., 1968). In this paper we shall propose a new role for the microvilli as a mechanosensory system, which not only senses fluid shear and drag forces, but has the capability of greatly amplifying the mechanical stresses that are felt on the intracellular cytoskeleton. To quantitatively explore this hypothesis we shall develop a mathematical model to predict the hydrodynamic forces and torques on the microvilli, their distribution along the length of the microvillus and the bending deformation of the F-actin microfilaments in the microvilli due to this hydrodynamic loading. These hydrodynamic forces and torques will also be related to the flow-dependent spacing of the microvilli that has been measured (Maunsbach et al. 1987).

The efferent limb of the control of proximal tubule fluid reabsorption appears to be reasonably well established. Volume reabsorption is driven by Na^+ reabsorption and this reabsorption rate is determined by Na^+ entry across the luminal membrane in which

the Na^+/H^+ antiporter is the most important entry step (Weinstein, 1992). The afferent limb, namely the mechanism by which the proximal tubule senses axial flow rate is unknown, and in this regard attention has been focused on the brush border of proximal tubule cells, since this is the interface with the tubule lumen. These two to three-micron, densely packed luminal projections not only greatly amplify luminal membrane surface area (Welling and Welling, 1975), they define a region near the luminal cell surface, whose geometry can change with changes in perfusion conditions (Maunsbach et al., 1987). A number of workers have considered the possibility that changes in axial flow might produce changes in solute ion concentration within the brush border region, and that such ion concentration changes could somehow be sensed by the cell (Basmadjian et al., 1980). However, all model calculations attempting to estimate such solute gradients have indicated that this diffusion is so rapid as to preclude any significant concentration difference within the brush border (Krahn and Weinstein, 1996).

One possibility, which has not been previously proposed or quantitatively explored, is that the microvilli can serve a mechanosensory role in the afferent limb of proximal tubule perfusion-absorption balance. This possibility is suggested by the axial cytoskeletal structure of the microvilli reported by Hassen and Hermann (1962). Subsequent studies (Rostgaard and Thuneberg, 1972; Maunsbach, 1973) showed that each microvillus contains a distributed array of 6-10 long axial microfilaments of 7 nm diameter, which immunocytochemical analysis showed were F-actin microfilaments (Bendayan, 1983). These filaments we hypothesize would provide a structural rigidity to the microvilli that could enable them to resist bending when subject to hydrodynamic

forces and thus capable of serving as a mechanotransducer, much like the hair cells in the inner ear.

A logical mechanosensory candidate for most cells subject to fluid flow is fluid shear stress. There is an extensive literature on the biochemical and ultrastructural effects of fluid shear on cells since the study by Dewey et al. (1980) first demonstrated that vascular endothelial cells could be grown in culture and exposed to fluid shear under carefully controlled conditions. A wide variety of ultrastructural and intracellular biochemical responses to fluid shear have been documented involving Ca^{++}, second messengers and NO release (Davies, 1995). Vascular endothelial cells are exposed to fluid shear stresses that are typically 10-20 dynes/cm^2 on the arterial side of the circulation and 1-2 dynes/cm^2 on the venous side. If the surface of the brush border cells did not have microvilli, the fluid shear stress would vary from about 1 to 5 dynes/cm^2 for Poiseuille flow over the normal range of flow rates, which lies in the same range as for vascular endothelium. However, the presence of the microvilli produces a unique flow structure in the vicinity of the brush border wherein the fluid shear stress at the base of the microvilli is several hundred times smaller than the drag forces on the microvilli themselves. The dynamics of this fluid flow and the forces generated by both the fluid shear stresses acting near the tips of the microvilli and the axial flow past the main body of the microvillus will be examined. In particular, we are interested in the force and torque (bending moment) distribution on each microvillus, and we hypothesize that it is the bending moment produced by these forces that acts as a mechanical transducer for the sensing of the axial fluid flow along the tubule. These hydrodynamic forces will then be used as input into an elastic model for the bending deformation of the actin cytoskeleton

of the microvillus to predict the displacement of the microvilli tips. We speculate that this bending moment is transmitted to the cytoskeleton in the cell interior where it is converted into a biochemical response.

§ 2.2 Methods

§ 2.2.1 Ultrastructural model for tubule and the brush border

The idealized ultrastructural model for the proximal tubule is sketched at the cellular and tubular cross-sectional scales in Fig. 2.1. Fig. 2.1A is a schematic of a proximal tubule cell from an S2 segment in the distal part of the convoluted tubule or the beginning of the straight segment (Maunsbach and Christensen, 1992). It is in this region that Maunsbach et al. (1987) examined the effect of flow on proximal tubule ultrastructure. The cells in this segment are characterized by densely spaced microvilli, numerous mitochondria and extensive interdigitation of the lateral membrane near the basal surface. The microvilli are even denser and longer in the S1 segment and significantly less dense in the S3 segment which comprises most of the straight tubule. Of particular interest in this study is how this difference in ultrastucture affects the flow, forces and torques on the microvilli. Fig. 2.1B is our macroscopic model of the entire tubule shown in transverse cross-section. The luminal radius of the tubule excluding the microvilli is R_L and the height of the brush border is L. The total radius of the tubule R_0 is thus $R_L + L$. From a hydrodynamic viewpoint the fluid flow is subtle since the microvilli form a closely spaced array in which there is a small, but non-negligible axial bulk flow through the microvilli which is driven by the axial pressure gradient in the tubule lumen. In addition, there are two thin interaction layers, one near the microvilli

tips and one at the base of the microvilli, where the fluid flow must adjust to satisfy the no-slip boundary conditions at the apical membrane of the proximal tubule cell in Fig. 2.1A or the fluid shear matching condition at the microvilli tips. The interaction layer near the base of the microvilli determines the fluid shearing stress on the apical membrane of the proximal tubule cells and the interaction layer near the tips of the microvilli determines the forces on the tips and, as we show later, provides the dominant contribution to the hydrodynamic torque on the microvillus. A central question in determining the torque is the drag distribution. In essence one wishes to determine how the small forces acting over most of the length of the microvilli due to the pressure driven bulk flow compare with the much larger drag forces that are felt in the highly localized region near the microvilli tips.

Fig. 2.2A is an enlarged sketch of the transverse section of the brush border showing the cross-sectional geometry of the microvilli. Ultrastructural studies have shown that the microvilli form a closely spaced hexagonal array (Maunsbach, 1973) where the open gap Δ between microvilli can vary significantly with fluid flow rate (Maunsbach, et al. 1987), and as previously noted with location on the S1, S2 and S3 segments. This hexagonal array will be further subdivided into repetitive periodic units each containing the equivalent of a single microvillus, as shown in Fig. 2.2B. Ultrastructural studies (Hanssen and Hermann, 1962; Rostgaard and Thuneberg, 1972; Maunsbach, 1973) have shown the existence of longitudinal actin microfilaments of 6 to 7 nm diameter extending the length of the microvillus but no microtubules or intermediate filaments. In our model we assume that these actin filaments provide a structural rigidity that prevents the microvilli from deforming significantly during flow

from a hydrodynamic standpoint. By this we mean that the microvilli can undergo small deformations in which the axial microfilaments might serve as strain transducers, but that these small strains do not significantly affect spacing of the microvilli and hence the fluid dynamic forces and torques acting on them.

§ 2.2.2 Mathematical model for fluid flow in tubular lumen

The hydrodynamic problem for the flow past the microvilli tips is a classical unsolved problem in the fluid mechanics literature. Rigorous hydrodynamic solutions have been obtained for the two-dimensional Stokes flow past periodic fiber arrays which are infinite in extent. One of the best known of these solutions, Sangani and Acrivos (1982), describes the flow transverse to an infinite hexagonal array of circular fibers whose cross-sectional geometry is shown in Fig. 2.2A. The more difficult problem which we wish to analyze in the present study is the three-dimensional flow in the transition region in the vicinity of the microvilli tips. In particular, we wish to examine the flow transition that occurs between the shear flow in the tubule lumen and the fiber-containing region where the flow asymptotically approaches the behavior described by the Sangani and Acrivos solution. This region is of greatest concern to us since it is the primary determinant of the forces and torques on the microvilli.

There have been several prior studies that have examined related interface problems. The one that is the closest to the present study is the model proposed by Mokady et al. (1999) for the shear flow over an endothelial glycocalyx. In this model the endothelial glycocalyx is treated as a layer of porous matrix whose fibers are arranged in a periodic horizontal square array parallel to the underlying solid boundary and transverse to the flow direction. A numerical technique developed in Larson and Higdon (1987) is

used to solve the Stokes equations for viscous flow around each fiber and the decay in the average horizontal velocity as one penetrates the matrix layer. This problem differs from the present one in several fundamental aspects. In our problem the microvilli (the fiber array in Fig. 2.1B) are vertical rather than horizontal, the flow is confined in a circular cylinder rather than unbounded, the fiber fraction is much greater (this is typically 0.01 to 0.02 for the endothelial glycocalyx) and the interface is cylindrical rather than planar. Also, our fiber array is hexagonal rather than square, but this adds no further difficulty since the solutions in Sangani and Acrivos for the infinite fiber array describe both fiber geometries.

The most important difference cited above is the fiber orientation. The force on a horizontal fiber transverse to the flow direction is uniform whereas in our problem the most important feature is the variation of the force along the microvillus length. This type of problem has not been treated previously to the authors' knowledge. The presence of a confining cylindrical boundary at $R = R_0$ creates an axial pressure gradient that drives a small, but important, flow across the microvilli. The magnitude of this flow determines the relative importance of the drag forces over the main body of the microvillus as opposed to the drag force on the microvilli tips in the interface region described above. The problem for the detailed flow around the horizontal fibers in Mokady et al. is two-dimensional, in contrast to the present flow geometry, which is fully three-dimensional. We thus seek a simplified solution approach in which we try to avoid the necessity for obtaining detailed solutions for the three-dimensional velocity field surrounding each microvillus. The key to this simplification is to devise an approach which first describes just the decay in the average velocity with distance from the microvillus tip and then use

this solution in a model which describes the local fluid flow around and the local variation of the axial force along the microvillus.

The simplified solution approach that we have adopted combines effective medium theory (Brinkman equation) and the rigorous hydrodynamic solutions in Sangani and Acrivos for Stokes flow past the infinite hexagonal fiber array. We first consider the solution to the axisymmetric flow problem sketched in Fig. 2.1B. This flow is divided into two regions, a core flow and a flow through the fiber (microvillus) array sketched in Fig. 2.2A. The flow in the core region or lumen is described by the Navier-Stokes equation for unidirectional axial flow in a circular cylinder. For this flow the inertial terms vanish and the simplified equation can be written in axisymmetric (R, Z) coordinates as

$$\frac{dP}{dZ} = \mu \frac{1}{R} \frac{\partial}{\partial R}\left(R \frac{\partial U_c}{\partial R} \right), \tag{2.1}$$

where U_c is the fluid velocity in the core and μ is the fluid viscosity. In the margin region $R_L < R < R_0$ with microvilli, we use a Brinkman equation for flow through a porous media (Bird et al., 1960)

$$\frac{dP}{dZ} = \mu \frac{1}{R} \frac{\partial}{\partial R}\left(R \frac{\partial U_m}{\partial R} \right) - \frac{\mu}{K_p} U_m . \tag{2.2}$$

Here U_m is the local average axial velocity in the microvillus array and K_p is the two-dimensional Darcy permeability for an infinite fiber array. The expression for K_p will be derived shortly using the solution for the drag coefficient for an individual fiber in Sangani and Acrivos. Equation (2.2) differs from equation (2.1) in that it contains a

distributed body force or Darcy term, $\frac{\mu U_m}{K_p}$, due to the drag on the microvilli. The second term in equation (2.2) is the same as the viscous term in equation (2.1). This term is only important near boundaries or interfaces where the gradient in the axial velocity is large. In the region removed from boundaries the Darcy term will dominate except in the limit where the microvilli are sparse. Both the Stokes and Brinkman equations are linear and thus it is a simple matter to include the radial component of the velocity to account for fluid absorption. This absorption can account for as much 70 percent of the filtration flow in the tubule and a substantial decrease in the axial flow and pressure gradient along the proximal tubule. However, as we shall show next, the radial flow produced by the absorption, though it leads to a significant radial velocity and radial pressure gradient in the brush border, has an insignificant effect on equation (2.2) for the axial velocity profile within the brush border and consequently the forces and the bending moments on the microvilli. The radial outflow is along the axes of the microvilli and, thus, does not contribute directly to the drag and torque on the microvilli. The more subtle question is the effect of the radial outflow on the pressure gradient within the brush border.

In the Appendix B we have developed a simple analysis to show the effect of uniform absorption on equation (2.2). The key result is that, although there can be a large drop in pressure across the brush border due to a radial Darcy flow, the axial pressure gradient to lowest order is uniform across the layer. As shown in the Appendix B the radial absorption can be modeled as the flow from a line source of uniform strength. The momentum equation in the radial direction shows that $\frac{\partial}{\partial Z}\left(\frac{\partial P}{\partial R}\right)=0$ if the slow variation of the axial flow is neglected in comparison with the rapid variation of the axial flow in

the R direction within the brush border. Since the order of differentiation can be changed, one finds that $\frac{\partial}{\partial R}\left(\frac{\partial P}{\partial Z}\right)=0$ or that the radial variation of axial pressure gradient across the brush border vanishes although the pressure itself is a function of R. This non-intuitive result is also observed for a viscous stagnation point flow where the pressure varies across the viscous boundary layer, but the streamwise pressure gradient is constant across the layer. It is clear from this result that the axial pressure gradient across the brush border in equation (2.2) can be treated as if it were only a function of Z. For a uniform absorption $\frac{\partial P}{\partial Z}$ decreases linearly, but at each axial location the axial pressure gradient can be treated as if it were uniform across the entire tubule-section.

Equations (2.1) and (2.2) can be cast in dimensionless form by introducing the dimensionless variables

$$R = R_0 \cdot r, \qquad Z = R_0 \cdot z, \qquad U_i = U_0 \cdot u_i, \qquad P = P_0 \cdot p, \tag{2.3}$$

where the characteristic length, velocity and pressure are defined by

$$R_0 = R_L + L, \qquad U_0 = \frac{Q}{A}, \qquad P_0 = \frac{\mu U_0}{R_0},$$

and i = c or m depending on whether one is describing the core flow or brush border flow. Here R_L is the luminal radius, L is the height of the microvilli, Q is the flow in the tubule, A is the cross-sectional area of the tubule, and U_0 is the average velocity.

The dimensionless form of equation (2.2) for axisymmetric flow,

$$\frac{dp}{dz} = \frac{1}{r}\frac{\partial}{\partial r}\left(r\frac{\partial u_m}{\partial r}\right) - \alpha^2 u_m, \tag{2.4}$$

contains a single dimensionless parameter α given by

$$\alpha = \frac{R_0}{\sqrt{K_p}}. \tag{2.5}$$

The denominator, $\sqrt{K_p}$, in the definition of α is a characteristic length describing the thickness of the fiber interaction layers at the base and tip of the microvilli. One can show, Tsay and Weinbaum (1991), that this characteristic thickness is of the same order as the microvillus spacing Δ. Thus, one anticipates that the solution of (2.4) will entail thin regions whose thickness is of order Δ near the base and tip of the microvilli where there will be steep velocity gradients and the velocity must adjust to satisfy boundary and matching conditions. Since Δ is of order 0.1 μm and R_0 is typically 20 to 30μm depending on flow rate, α is of order several hundred. We will, therefore, be interested in the solutions to equation (2.4) in the large α limit.

There are two boundary conditions, one at the center of the tubule, r=0, where we require that the velocity be symmetric,

$$\frac{\partial u_c}{\partial r} = 0, \tag{2.6}$$

and one on the wall (apical membrane), r=1, where we require that the no-slip boundary condition be satisfied,

$$u_m = 0. \tag{2.7}$$

In addition, we require that velocity and shear stress be continuous at the edge, $r = r_L$, of the brush border

$$u_m(r_L) = u_c(r_L), \qquad \tau_m(r_L) = \tau_c(r_L). \tag{2.8}$$

τ_m and τ_c are given by $\mu \frac{\partial U_m}{\partial R}$ and $\mu \frac{\partial U_c}{\partial R}$, respectively.

Equation (2.8) for the continuity of shear stress across the outer edge of the brush border is strictly valid only in the limit of a dilute fiber layer. For the present case the microvilli occupy 25 percent of the brush border volume and cross-sectional area and, thus, the area fraction occupied by the microvilli tips should be considered in the tangential force balance at the brush border edge. The shear force imposed by the core flow is taken up by both the fluid phase and the solid phase, where in equation (2.8) it is attributed entirely to τ_m, the shear force acting on the fluid phase. The effective shear force acting on the fluid phase is only τ_C times the volume fraction of the fluid phase. If the boundary value problem were solved with this shear force one would obtain a smaller slip velocity at the brush border interface, and hence the drag on the microvilli tips would be smaller than calculated herein but one would have to add the shear force acting on the solid phase. This would make for a more cumbersome calculation of the forces and torques acting on the microvilli. By using equation (2.8) as the interface condition we have ascribed the entire force acting on the microvilli tips to the fluid drag and have set the shear force on the solid phase equal to zero. However, the tip interaction layer is at most confined to the outer 180 nm of the brush border. The bending moment due to the fluid drag in this interaction layer acts at the centroid of the velocity profile and not exactly at the microvilli tips but very close to this location. Thus, it does not make a significant difference whether the bending moment due to the shear force acting on the solid phase at the interface is attributed to the solid or the fluid since the point of application of the force is nearly the same. In effect one obtains a larger fluid drag and

torque, but this increment in drag and torque would be nearly the same as that which one would obtain by including the shear force at the interface acting on the solid phase.

§ 2.2.3 Solution for velocity field and mass flow

The general solution to equation (2.4) is given by

$$u_m(r) = \left(-\frac{1}{\alpha^2}\frac{dp}{dz}\right)\left(C_1\frac{I_0(\alpha r)}{I_0(\alpha)} + C_2\frac{K_0(\alpha r)}{K_0(\alpha)} + 1\right), \tag{2.9}$$

where $I_0(r)$ and $K_0(r)$ are zero-order modified-Bessel functions, $\frac{dp}{dz}$ is the dimensionless pressure gradient and C_1 and C_2 are arbitrary integration constants.

The general solution to equation (2.1), which satisfies boundary condition (2.6), can be written in dimensionless form as

$$u_c(r) = \left(-\frac{1}{4}\frac{dp}{dz}\right)(r_L^2 - r^2) - \left(\frac{1}{\alpha^2}\frac{dp}{dz}\right)C_3, \tag{2.10}$$

where C_3 is an integration constant.

The matching conditions (2.7) and (2.8) determine the unknown constants C_1, C_2 and C_3. These expressions for the C_i and their asymptotic expressions, in the limit $\alpha >> 1$ are given by

$$C_1 = -\frac{\frac{K_1(\alpha r_L)}{K_0(\alpha)} + \frac{\alpha r_L}{2}}{\frac{K_1(\alpha r_L)}{K_0(\alpha)} + \frac{I_1(\alpha r_L)}{I_0(\alpha)}} \cong -1 \tag{2.11a}$$

$$C_2 = \frac{\frac{\alpha r_L}{2} - \frac{I_1(\alpha r_L)}{I_0(\alpha)}}{\frac{K_1(\alpha r_L)}{K_0(\alpha)} + \frac{I_1(\alpha r_L)}{I_0(\alpha)}} \cong \frac{\frac{\alpha r_L}{2}}{\frac{K_1(\alpha r_L)}{K_0(\alpha)}} \tag{2.11b}$$

$$C_3 = C_1 \cdot \frac{I_0(\alpha r_L)}{I_0(\alpha)} + C_2 \cdot \frac{K_0(\alpha r_L)}{K_0(\alpha)} + 1 \cong \frac{\alpha r_L}{2} + 1 \tag{2.11c}$$

The dimensional water flux in the tubule is given by

$$Q = \int_0^{R_0} U_i \cdot 2\pi R dR = \int_0^{R_L} U_c \cdot 2\pi R dR + \int_{R_L}^{R_0} U_m \cdot 2\pi R dR . \tag{2.12a}$$

Equation (2.12a) is the integral of the velocity over the entire cross section of the tubule. Since the brush border flow contributes very little to the total flux, the second integral describing this flux can be neglected and equation (2.12a) reduces to

$$Q \cong \int_0^{R_L} U_c \cdot 2\pi R dR = U_0 \cdot \pi {R_0}^2 \cdot \left[\frac{dp}{dz} \left(\left(-\frac{1}{8} \right) {r_L}^4 + \left(-\frac{1}{\alpha^2} \right) C_3 {r_L}^2 \right) \right]. \tag{2.12b}$$

From (2.11) C_3 is of $O(\alpha)$ and the second term of Q in (2.12b) is of order $\frac{1}{\alpha}$ smaller than the first. The first term in (2.12b) is the same as for the Poiseuille flow in a tube of dimensionless radius r_L. The second term in (2.12b) describes a small bulk flow due to the small slip velocity at the microvilli tips.

By introducing the dimensionless water flux,

$$Q_0 = U_0 \cdot \pi {R_0}^2 ,$$

one can write the dimensionless pressure gradient to order $\frac{1}{\alpha}$ as

$$-\frac{dp}{dz} \cong \frac{q}{\left[\frac{1}{8} r_L{}^4 + \frac{1}{\alpha^2} C_3 r_L{}^2\right]}. \tag{2.13}$$

Here q is the dimensionless flux, $\frac{Q}{Q_0}$, and r_L is the dimensionless position of the edge of the brush border.

§ 2.2.4 Darcy permeability coefficient for the brush border

The expression for the two-dimensional Darcy permeability coefficient can be derived by examining a periodic unit in the hexagonal microvillus array shown in Fig. 2.2B. The distributed or body force per unit volume, F, is the Darcy term in equation (2.2).

The total pressure force acting on a periodic unit, ABCD, in Fig. 2.2B, whose length and height are $(2a+\Delta)$ and $(2a+\Delta)\frac{\sqrt{3}}{2}$, respectively, is

$$-\frac{dP}{dZ} \cdot (2a+\Delta) \cdot (2a+\Delta)\frac{\sqrt{3}}{2}, \tag{2.14}$$

while Darcy's law requires that

$$\frac{dP}{dZ} = -\frac{\mu}{K_p} U_m. \tag{2.15}$$

From (2.14) and (2.15) the pressure force acting on the periodic unit ABCD can be written as

$$-\frac{dP}{dZ} \cdot (2a+\Delta) \cdot (2a+\Delta)\frac{\sqrt{3}}{2} = \frac{\mu}{K_p} U_m \cdot (2a+\Delta)^2 \cdot \frac{\sqrt{3}}{2}. \tag{2.16}$$

Note, however, from Fig. 2.2B that this is also the local drag force F per unit length on a single microvillus, since the periodic unit for the hexagonal array comprises a single cylindrical fiber or microvillus. Thus from (2.16), F is given by

$$F = -\frac{dP}{dZ}\cdot(2a+\Delta)^2\cdot\frac{\sqrt{3}}{2} = \frac{\mu}{K_p}U_m\cdot(2a+\Delta)^2\cdot\frac{\sqrt{3}}{2}, \tag{2.17}$$

and K_p can be written in terms of F as

$$K_p = \frac{\mu U_m}{F}\cdot(2a+\Delta)^2\cdot\frac{\sqrt{3}}{2}. \tag{2.18}$$

Sangani and Acrivos (1982) have obtained a numerical solution for the Stokes flow past the periodic fiber array in Fig. 2.2B. They showed that the dimensionless drag, $\frac{F}{\mu U_m}$, can be expressed by

$$\frac{F}{\mu U_m} = \frac{4\pi}{\ln(c^{-\frac{1}{2}}) - 0.745 + c - \frac{1}{4}c^2 + O(c^4)}, \tag{2.19}$$

where c, the solid fraction, is defined by

$$c = \frac{\pi a^2}{(2a+\Delta)^2\frac{\sqrt{3}}{2}} = \frac{\pi}{(2+\frac{\Delta}{a})^2\frac{\sqrt{3}}{2}}. \tag{2.20}$$

Expression (2.19) is valid for c < 0.4. For control flow conditions where Δ =74.1nm and a=45nm, c=0.27. From (2.18), (2.19) and (2.20)

$$\frac{K_p}{a^2} = \frac{\mu U_m}{F}\cdot\frac{\pi}{c} = \frac{\ln(c^{-\frac{1}{2}}) - 0.745 + c - \frac{1}{4}c^2 + O(c^4)}{4c}. \tag{2.21}$$

Equation (2.21) is rigorously valid only for two-dimensional flow. It is, however, also a reasonable approximation for the local drag along a microvillus where U_m is a function of

R. A rigorous justification of this approximation would require a much more complicated three-dimensional analysis similar to that in Tsay and Weinbaum (1991) where the radial pressure gradient and velocity are considered.

§ 2.2.5 Drag and shear force per unit tubule length

The total drag force on the microvilli per unit tubule length is given by

$$F_d = \int_{R_L}^{R_0} \left(-\frac{\mu U_m}{K_p} \right) \cdot 2\pi R dR . \tag{2.22}$$

Equation (2.22) is the integrated drag on all microvilli that lie in the annular region $R_L < R < R_0$ due to thin effective hydrodynamic resistance, the Darcy term $\frac{\mu U_m}{K_p}$ in equation (2.2). Using equations (2.1) and (2.2), one can write (2.22) in the equivalent form

$$F_d = \int_{R_L}^{R_0} \left(-\frac{\mu U_m}{K_p} \right) \cdot 2\pi R dR = \int_{R_L}^{R_0} (\nabla P - \mu \nabla^2 U_m) \cdot 2\pi R dR = \int_0^{R_0} (\nabla P - \mu \nabla^2 U_i) \cdot 2\pi R dR ,$$

where i = c or m in the last integral. The latter integral can be readily evaluated

$$F_d = \int_0^{R_0} (\nabla P - \mu \nabla^2 U_i) \cdot 2\pi R dR = \frac{dP}{dZ} \cdot \pi {R_0}^2 - \tau(R_0) \cdot 2\pi R_0 . \tag{2.23}$$

From (2.23) it is clear that the pressure drop per unit tubule length (first term on r. h. s. of (2.23)) is balanced by the shear force at wall, F_s, (second term on r. h. s. of (2.23)) and the drag force, F_d, on the microvilli per unit tubule length.

The shear force per unit tubule length is given by

$$F_s = \tau(R_0) \cdot 2\pi R_0 . \tag{2.24}$$

From (2.23), the ratio λ of the drag force to the shear force per unit tubule length is expressed by

$$\lambda = \frac{F_d}{F_s} = \frac{\frac{dP}{dZ} \cdot R_0}{2\tau(R_0)} - 1 = \frac{\alpha}{2} \cdot \frac{1}{\left(\frac{I_1(\alpha)}{I_0(\alpha)} + \frac{\alpha}{2} r_L \cdot \frac{K_1(\alpha)}{K_1(\alpha r_L)} \right)} - 1. \tag{2.25}$$

Note that in (2.25) λ depends only on the brush border and microvillus geometry.

§ 2.2.6 Drag and torque distribution on a microvillus

To obtain the drag force distribution f_d acting on each microvillus we divide the total drag on all the microvilli per unit length, F_d in equation (2.22), by n, number of microvilli per unit length of tubule and integrate between R_L, the microvilli tip and any position R

$$f_d = \frac{1}{n} \cdot \int_{R_L}^{R} \left(-\frac{\mu U_m}{K_p} \right) \cdot 2\pi R dR. \tag{2.26}$$

When R is equal to the radius of the tubule, (2.26) gives the total drag force acting on a single microvillus.

From equation (2.26) the local force per unit length of microvillus is given by

$$\frac{df_d}{dR} = \frac{1}{n} \cdot \left(-\frac{\mu U_m}{K_p} \right) \cdot 2\pi R. \tag{2.27}$$

The bending moment per unit length acting on the base of the microvillus is given by

$$\frac{dT}{dR} = \overline{R} \cdot \frac{df_d}{dR},$$

where $\overline{R} = R_0 - R$ is the lever arm of the force element. The integrated torque distribution is defined by

$$T(R) = \int_{R_L}^{R} \overline{R} \cdot df_d = \int_{R_L}^{R} \overline{R} \cdot \frac{1}{n}\left(-\frac{\mu U_m}{K_p}\right) \cdot 2\pi R d\overline{R} . \qquad (2.28)$$

$T(R)$ is the torque acting on a single microvillus between its tip and any position R. When R is equal to the radius of the tubule, (2.28) gives the total torque acting on a single microvillus.

§ 2.2.7 Elastic model for bending of microvillus

Fortunately, there is sufficient information on the structure of the F-actin cytoskeleton of the microvillus and the elastic properties of an individual actin filament to construct from first principles a model for its bending deformation due to its hydrodynamic loading. These ultrastructural studies summarized by Maunsbach (1973) indicate that there are between 6 and 10 long axial microfilaments randomly distributed in each cross-section. Most of the axial microfilaments are clustered in the central region of the microvillus cross-section rather than near its periphery. In our idealized ultrastructural model shown in Fig. 2.3A, we have assumed that on average seven such filaments are arranged in an hexagonal array with six of the filaments equally spaced on a circle that is the half radius of the cross-section. This is a close approximation to the electron micrographs shown in Maunsbach (1973). Each microfilament is 7 nm in diameter. Although the spacing of the transverse linker molecules, fimbrin and α-actinin, is not known to our knowledge, it is reasonable to assume that their primary function is that of spacer molecules that hold the long axial filaments in a nearly parallel array. The bending moment on the microvillus due to the distributed hydrodynamic drag is, therefore, borne entirely by its seven axial elements. This structure is analgous to a reinforced concrete beam in which the bending resistance of the concrete between its

axial steel reinforcing rods is neglected. Fig. 2.3B is a sketch showing the geometry of the deformed microvillus with just its central microfilament.

According to the elementary theory for the bending of beams (Beer and Johnston, 1992), the deflection y of the microvillus, see Fig. 2.3B, satisfies the fourth order equation

$$\frac{d^2}{dx^2}\left(EI\frac{d^2y}{dx^2}\right)=D(x)=\frac{df_d}{dR}. \tag{2.29}$$

Here $x=R_0-R$, E is the Young's modulus of the individual actin filaments, I is the moment of inertia of the cross-section and D(x) is the distributed axial load due to the hydrodynamic drag obtained from equation (2.27). I depends on the orientation of the bending axis. However, one can show that for the geometry in Fig. 2.3A the moment of inertia varies insignificantly with any axis passing through the origin because of the hexagonal symmetry. Since the radius of an actin filament, r_f, is small compared to the radius of the microvillus a, the contribution of each filament to I is the area of the filament $\pi r_f^{\,2}$ times the distance from the axis of rotation. Thus, I for the cross-sectional geometry in Fig. 2.3A is

$$I=4\cdot\left(\pi r_f^{\,2}\cdot\left(\frac{\sqrt{3}}{2}\cdot\frac{a}{2}\right)^2\right)=\frac{3}{4}\pi r_f^{\,2}\cdot a^2. \tag{2.30}$$

The drag force distribution or the beam loading is given by equation (2.27). However, as will be shown in the results section, this loading can be well approximated by the superposition of two simple loads, a uniform load, q_m, over most of the length of the microvillus and a concentrated force, P_m, acting at its tip. This allows us to write a

greatly simplified expression for the loading which enables us to integrate the beam equation analytically. This simplified loading distribution is given by

$$D(x) = P_m \delta(x - L) + q_m . \tag{2.31}$$

Four boundary conditions are needed to define the boundary value problem for the deflection of the microvillus. At x = 0, the base of the microvillus, it is reasonable to assume that the longitudinal actin filaments are anchored to more rigid supporting structures in the intracellular cytoskeleton. These could be either more complex actin networks near the apical membrane, microtubules or intermediate filaments. The nature of this anchoring is not yet known. If this anchoring is relatively inflexible and treated as a rigid support, then the displacement and slope of the microvillus relative to the vertical will vanish,

$$y(0) = 0, \qquad y'(0) = 0. \tag{2.32}$$

At the free end of the beam, x=L, there is no bending moment and the vertical shear force does not vanish. We require that

$$y''(L) = 0, \qquad y'''(L) = -\frac{P_m}{EI}. \tag{2.33}$$

The solution to the boundary value problem defined by equation (2.29), (2.31), (2.32), (2.33) is given by

$$y(x) = \frac{1}{EI}\left(\frac{1}{6}P_m(-x^3 + 3L^2 x) + \frac{1}{24}q_m(x^4 - 4Lx^3 + 6L^2x^2)\right). \tag{2.34}$$

At the free end of the beam, x = L, the maximum deflection is achieved. From (2.34) it is given by

$$y(L) = \frac{1}{EI}\left(\frac{1}{3}P_m L^3 + \frac{1}{8}q_m L^4\right). \tag{2.35}$$

§ 2.3 Results

§ 2.3.1 Velocity field in the tubule lumen

In Fig. 2.4 we have plotted the velocity profiles in the tubule lumen, the transition layer in the vicinity of the microvilli tips and in the brush border. Three curves are required because the velocity scale varies so greatly between regions. This behavior is characteristic of solutions in the large α limit. The solutions in Fig. 2.4 as well as Fig. 2.6 are for a control value of Q of 30 nl/min. The edge of the brush border is located at a dimensionless r of 0.847. The centerline velocity in the lumen is 1.66 mm/s and the profile in the core is a parabola typical of Poiseuille flow except near the interface with the brush border, where the velocity drops to a very small values over a distance of a few tenths of a micron as observed in Fig. 2.4B. At the edge of the brush border, r = 0.847, the velocity is only 4.11 μm/s or roughly 1/400 of the centerline velocity. The velocity then falls off rapidly as one enters the lateral spaces between the microvilli and, as shown in Fig. 2.4C, asymptotically approaches a nearly constant value of only 10 nm/s in the central region of the brush border. As seen in Fig. 2.4B the thickness of the transition region at the microvilli tip where the velocity decays to the nearly vanishing bulk flow velocity is approximately 0.011 in dimensionless r units. This corresponds to a distance of 0.180 μm in physical units or about 7 percent of the microvilli length. This is about 2.4 times the open gap between microvilli, which for the control flow is 74 nm. As observed in Fig. 2.4C, a transition layer of comparable thickness exists at the base of the microvilli where the velocity decays from the miniscule bulk flow velocity in the brush border to

zero at the apical membrane so as to satisfy no slip conditions. Due to the miniscule magnitude of the bulk flow in the brush border, the velocity in Fig. 2.4C is plotted in nm/s where the velocity at the edge of the boundary layer at the apical membrane is about 10 nm/s. There is a slight decrease in the bulk flow velocity across the brush border due to the curvature of the radial coordinate system. This small bulk flow is driven by the axial pressure gradient in the lumen of the tubule.

In Fig. 2.5 we have plotted the tip velocity versus the open gap Δ between microvilli and also the dimensionless drag coefficient given by equation (2.19). It is clear that there is a nearly linear relationship between the tip velocity and Δ. This linearity can easily be derived from asymptotic analysis, see Appendix A. This effective slip velocity at the microvilli tips gives rise to the second term in the expression for Q in (2.12b).

The miniscule bulk flow in the brush border contributes negligibly to the total flow in the tubule. However, it plays a very important role in determining the total force on each microvillus and the torque that it experiences. Similarly, it might seem at first glance that the details of the velocity profile in the thin transition region near the tips of the microvillus are not significant. Since the forces in Stokes flow are proportional to the velocity, it is the integral of this velocity profile that determines the contribution of the tip region to the total force and torque on the microvillus. The central question is how this integrated drag on the tips of the microvilli compares with the much smaller forces due to the bulk flow, but which act over most of the length of the microvillus.

§ 2.3.2 Drag versus shear force

With a bulk flow velocity in the brush border that is five orders of magnitude smaller than the centerline velocity in the tubule, one wonders how the shear force acting

on the apical membrane at the base of the microvilli compares with the drag force on the microvilli. As noted earlier nearly all previous studies on the effect of fluid forces on vascular endothelial cells have examined the effect of fluid shear on the cell's cytoskeleton and intracellular biochemical responses. Since both these forces scale linearly with the velocity, the ratio of the drag force to the fluid shearing force would be independent of the tubule flow rate if the microvilli geometry did not change with flow rate. The ultrastructural study by Maunsbach et al. (1987) revealed that the open separation between the microvilli increased from 62.1 nm to 90.4 nm as the tubule flow was increased from 5 to 45 nm/min. One is thus interested not only in the ratio of the drag to fluid shear force at control conditions, where this separation distance is 74.1 nm, but also how this ratio changes more generally with microvilli spacing. The results of equation (2.25) are plotted in Fig. 2.6. One observes that the ratio of the drag to fluid shear force increases from approximately 360 to 580 as the open spacing between microvilli decreases from 90.4 to 62.1 nm and that there is a rapid fall off in this ratio as the distance between microvilli increases. The density of the microvilli in the S3 segment is approximately one quarter that in the S2 segment and thus could be twice the control value cited above or 150 nm. Even for this large spacing the ratio of the drag to shear force is nearly 200.

§ 2.3.3 Drag and torque distribution on a single microvillus

In Fig. 2.7 we have plotted equation (2.26) for the integrated drag distribution starting at the microvillus tip, r=0.847, to the base of the microvillus. One observes a sharp break in this curve at approximately r = 0.858. At this location the average velocity differs by less than one percent from the bulk flow velocity in the interior of the brush

border. The integrated drag at this location is 73.8 percent of the total drag on the microvillus although this drag acts on only the 7 percent (0.18 μm) of the microvillus length near its tip. In summary, the drag due to the bulk flow in the interior of the brush border contributes approximately 1/4 of the total drag and the flow near the tip 3/4 of the total drag. This highly asymmetric distribution, as we see next, provides for a large amplification in the torque experienced by the microvillus. The total drag force on the microvillus for a control flow of 30 nl/min is 7.38×10^{-3} pN.

In Fig. 2.8 we have plotted equation (2.28) for the integrated torque distribution starting at the microvillus tip proceeding to the base of the microvillus. One again observes a sharp break in this curve at approximately r = 0.858. The integrated torque at this location is 86.2 percent of the total torque on the microvillus although this torque, like the drag, acts only on the 7 percent of the microvillus length near its tip. In summary, the torque due to the bulk flow in the interior of the brush border contributes only about 1/7 of the total torque and the flow near the tip 6/7.

§ 2.3.4 Effect of flow on drag and torque

In Table 2.1 we have summarized the effects of changing the flow rate using the ultrastructural data provided by Maunsbach et al. (1987). One observes that the drag force on the microvilli does not vary linearly with flow rate if the changes in lumen diameter and microvilli separation with flow rate are accounted for. In fact one notes that there is only a slightly more than two fold increase in drag when the flow is increased from 5 to 45 nl/min. If we assume that the length of the microvilli do not change, then, since three quarters of the drag acts near the tips of the microvilli, the torque should increase roughly in proportion to the fluid drag on the microvilli tips. This non-linear

behavior, which is observed in experiments with individual perfused tubules *in situ*, is associated with an increase in hydrostatic pressure in the lumen of the tubule. This increase in tubule lumen pressure will cause a distension of the perfused nephron since neighbouring nephrons will not be at elevated transepithelial hydrostatic pressure. *In vivo*, this distension probably does not occur since neighbouring nephrons would all be at the same transepithelial pressure.

§ 2.3.5 Bending deformation of the microvillus

The bending deformation of the microvillus and the deflection of its tip are given by equations (2.34) and (2.35) respectively. The two key parameters in these expressions are the moment of inertia, I, given by equation (2.30) and the Young's modulus E of the individual actin filaments in the microvillus cross-section shown in Fig. 2.3A. Realistic values for both of these parameters are available. In calculating I we have used the measured values, r_f=3.5nm and a = 45 nm (Maunsbach, 1973). The Young's modulus for an F-actin microfilament has been estimated from its bending modulus. This has been determined from force measurements obtained by the micromanipulation of single actin filaments by Kishino and Yanagida (1988). The calculated value for E is 1.44×10^9dynes/cm^2. In Fig. 2.9 we have plotted the deformed shapes of microvilli of four different lengths from 1.5 to 3.0 μm for a control flow of 30 nl/min when the open gap Δ between microvilli is 74.1 nm. Equation (2.35) shows that the maximum deflection of the microvilli, which is primarily determined by the concentrated drag forces near its tip, is proportional to the third power of the microvilli length. This accounts for the large increase in the maximum deflection with microvilli length. For a microvillus of 2.5μm length in an S2 segment the tip deflection is 3.78 nm, whereas for a 1.5μm microvillus,

the tip deflection is about one fifth this value. Thus at a control flow rate of 30nl/min the maximum tip deflection varies from about one to five percent of the microvilli diameter 90nm.

As noted earlier while the length of the microvilli decrease as one proceeds from the S1 to the S2 and S3 segments, the spacing of the microvilli increase and Δ for the S3 segment is about twice that for the S2 segment (Welling and Welling 1975). One can show from (2.23) that the hydrodynamic loading of an S3 microvillus at its tip, P_m, is roughly four times that for the S2 microvillus. This suggests that the length of the microvilli may decrease as their spacing increases so that the deflection of the microvilli tips does not vary greatly along the length of the tubule.

§ 2.4 Discussion

Glomerulotubular balance was first established in rat kidney via micropuncture (Schnermann et al., 1968), where spontaneous variation in glomerular filtration (over a range of flows from 15 to 60nl/min) was accompanied by a constant fractional proximal reabsorption. During periods of low filtration, this aspect of proximal tubule transport insures preservation of adequate delivery of sodium to the distal nephron (preserving acid and potassium excretion). The mechanisms for balanced tubular reabsorption appear to include both peritubular capillary effects and luminal factors (Earley and Schrier, 1973; Gertz and Boylan, 1973; Haberle and von Baeyer, 1983; Wilcox and Baylis, 1985). With respect to peritubular factors, any increase in filtration fraction must result in an increased peritubular protein concentration, and increased peritubular capillary protein concentration enhances proximal reabsorption (Brenner et al., 1969; Green et al., 1974).

The mechanism is thought to involve changes in interstitial hydrostatic pressure (Knox and Haas, 1982; Knox et al., 1983), with effects on both the tight junctions (Lewy and Windhager, 1968) and on the cells themselves. Nevertheless, a mathematical model of proximal nephron, which incorporated the observed effect of peritubular Starling forces to modulate reabsorption, demonstrated that the observed constancy of fractional reabsorption could only be achieved when alterations in luminal flow, independent of peritubular Starling forces, could also influence proximal reabsorption (Weinstein, 1990).

The impact of variation in luminal flow rate on tubular reabsorption has been termed "perfusion-absorption balance" (Wilcox and Baylis, 1985). This effect has been best demonstrated in rat microperfusion studies (Bartoli et al., 1973; Haberle et al., 1981; Peterson et al.,1986; Romano et al., 1996). With respect to specific solutes, flow-dependent reabsorption has been found to influence the transport of glucose (Knight et al., 1980), bicarbonate (Chan et al, 1982; Alpern et al., 1983; Liu and Cogan, 1988), and chloride (Green et al., 1981; Wong et al., 1995). One of the best illustrations of this phenomenon is the micropuncture data of Chan et al. (1982), in which a three-fold increase in luminal perfusion rate (with trivial changes in luminal HCO_3^- concentration) produced a doubling of the rate of bicarbonate reabsorption. The underlying mechanism for flow-dependent changes in reabsorption has not been established. One consideration has been an unstirred layer effect within the brush border (Richardson et al., 1973). The morphological observations of Maunsbach et al. (1987) demonstrated that lower tubule flow rates are associated with diminished tubule distention and a compaction of the brush border microvilli. Nevertheless, model calculations indicate it unlikely that there is any appreciable convective stirring within this pile (Basmadjian et al., 1980), nor should the

diffusion barrier between the bulk luminal fluid and the cell membrane pose any significant hindrance to Na^+/H^+ exchange (Krahn and Weinstein, 1996). Two relatively recent studies raise the possibility that increases in axial flow velocity recruit new transporters into the luminal membrane. Preisig (1992) examined recovery of cellular pH from an acute acid load in vivo. With increases in luminal flow rate, the pH recovery mediated by Na^+/ H^+ exchange was enhanced. Maddox et al. (1992) subjected rats to acute changes in vascular volume in order to obtain hydropenic, euvolemic, and volume expanded groups, with respective grouping according to decreased, normal, and increased GFR. When brush border membrane vesicles were prepared from each of these groups, and Na^+/H^+ kinetic parameters assessed, it was found that the V_{max} determinations stratified in parallel with GFR.

Ultimately, perfusion-absorption balance must derive from an afferent sensor of fluid flow rate in series with a cascade of effector steps which insert or activate new membrane transporters. The calculations of this paper indicate that the microvilli which constitute the proximal tubule brush border are physically suitable to function as such a sensor. The second component of this system may well be the actin cytoskeleton, which is abundant within and beneath the proximal tubule brush border (Maunsbach and Christensen, 1992). Indeed, the cytoskeleton has been implicated in volume regulation in a variety of cells (Moustakas et al., 1998), and specifically in proximal tubule, cytoskeletal disruption impairs the cell solute loss (volume regulatory decrease) following hypotonic cell swelling (Linshaw et al., 1992). Direct interactions of the cytoskeleton with a variety of membrane transporters, including ion channels, cotransporters, and the Na^+ /K^+-ATPase, have been identified (Cantiello, 1997). Thus,

specific interaction between the proximal tubule cytoskeleton and the apical cell membrane Na^+/H^+ exchanger remains a critical feature to demonstrate, in order to maintain plausibility for this scheme of signal transduction. Such a connection is provided by the proposal of Lamprecht et al. (1998) in which the Na^+/H^+ exchanger is linked via NHERF to ezrin, a kinase anchoring protein, which is attached to the actin cytoskeleton. Indeed, gross disruption of the actin cytoskeleton has recently been shown to impair function of the proximal tubule Na^+/H^+ exchanger, when expressed in other cells (Kurashima et al, 1999). It is not known, however, whether more subtle changes, such as perturbation of cytoskeletal stresses, can also affect this transporter. It must also be acknowledged that more extensive feedback loops may be important, from flow changes to membrane transporter density via gene activation. Such responses have been identified in renal tubular cells in culture, in which changes in shear stress have been implicated in increased number of microvilli, and in increased abundance of integral membrane proteins (Kaysen et al., 1999). Obviously, this response can not be invoked to account for acute (micropuncture) observation of perfusion-adaptation balance.

The analysis in the present study indicates that from both a hydrodynamic and structural standpoint, the microvilli are ideally suited to serve as mechanotransducers. Previously, it has been widely believed that the primary role of the brush border was to greatly amplify the luminal membrane area required for water and solute exchange. This does not explain why the microvilli have such striking uniformity in length, why the spacing between microvilli is so regular, why the microvilli decrease in length as their density decreases, what determines the density and distribution of the axial actin microfilaments in the microvilli and how these microfilaments are anchored to the

intracellular cytoskeleton near the apical membrane. These questions lead to a new view of the brush border epithelial cells not only as a transport organ, but as a cell with specialized ultrastructural components that could have mechonosensory functions.

We first consider the hydrodynamic function of the brush border. Except for the thin interaction region near the microvilli tips, the axial velocity within the brush border is five orders of magnitude smaller that the average axial velocity within the lumen of the tubule. In contrast, one can estimate that if half the filtrate is reabsorbed along the entire length (1cm) of the proximal tubule, then the radially directed average velocity along the axes of the microvilli is 0.24 μm/s. This is a tiny fraction ($0.15x10^{-3}$) of the axial velocity in the lumen. The radially directed flow due to reabsorption is, therefore, about 24 times the axially directed bulk flow within the brush border, but this radial flow produces no drag or torque on the microvilli since it is directed along the microvillus axis. The miniscule axial bulk flow contributes negligibly to the total flow in the tubule, yet it determines the nature of the hydrodynamic forces on both the microvilli and the apical membrane.

The nearly vanishing axial bulk flow velocity in the brush border in Fig. 2.4C was previously predicted in Basmadjian et al. (1980), using a semi-empirical Carman-Kozeny equation to estimate the hydraulic resistance. This semi-empirical relation was widely used before the more accurate solution of Sangani and Acrivos (equation 2.19) was derived. In this earlier study Basmadjian and coworkers derived an expression for the ratio of the flow in the brush border to the flow in the core. For control flow in the present study this ratio is approximately 5×10^{-6}, a value that is similar to the prediction in Basmadjian et al. for a dense microvillus array. These investigators were primarily

interested in unstirred layer effects due to the axial flow rather than the forces and torques due to the flow in the thin transition layer near the microvilli tips. This thin boundary layer, which is the primary focus of the present study, was neglected since it contributed insignificantly to the transport processes in the brush border.

Fig. 2.6 shows that, despite the very small axial bulk flow through the brush border, the drag forces on the microvilli are at least 200 times greater than the shear forces acting on the underlying apical membrane. Proximal tubule epithelial cells would never be able to detect fluid shear forces in the same manner as vascular endothelial cells, although the flow rate in the tubule is quite similar to the flow rate in a blood vessel of comparable diameter. One of the remarkable features of the circulation is that, although the blood vessels undergo more than 20 generations of branching, the fluid shear stress is nearly constant throughout the entire arterial side of the vasculature (Kamiya et al., 1984). Furthermore, relatively modest changes in fluid shear stress are readily detected by endothelial cells (Davies, 1995). These wall shear variations lead to short term biochemical responses and, in large vessels, endothelial dependent adaptive remodeling after longer exposure to changes in wall shear stress (Zarins et al., 1987). Proximal tubule epithelial cells thus need a different machinery to sense fluid flow rates, and hydrodynamic drag would appear to be a more logical candidate since it is several hundred times greater than fluid shear.

An unusual feature of the brush border microvilli is their remarkable local uniformity of length. Such uniformity would not be a prerequisite for a transport function associated with unstirred layer effects. It would, however, be essential if the tips of the microvilli all needed to sense the flow at the edge of the brush border. The detailed

velocity profile near the tips of the microvilli in Fig. 2.4B provides an intriguing and rational argument for this structure. One observes that the axial velocity decays over a length that is less than 0.2 μm or roughly twice the open spacing Δ between the tips. A microvillus that is only slightly shorter than its neighbors would experience virtually no axial flow near its tip and the hydrodynamic torque on this microvillus would be only about one-seventh that of its neighbors. There would be a small torque due to the bulk flow in the interior of the brush border, but as noted in Fig. 2.8, this torque is about one seventh that due to the drag at the microvilli tips. The deflection of this microvillus would be much smaller than its neighbors, see equation (2.35).

A quantitative calculation will make this point clear. We start by asking the question: what would be the consequence if the microvilli were heterogeneous in height? Fig. 2.4C shows that the velocity within the brush border is negligible, 10 nm/s, or about 1/400 of the 4.1 μm/s slip velocity at the tips of the microvilli or brush border edge shown in Fig. 2.4B. However, there is a very steep velocity gradient at the brush border edge and if a microvillus were to protrude even one μm into the lumen, one would encounter a velocity that is 150 μm/s, or 37 times the slip velocity at the brush border edge. Since the local force per unit microvillus length scales linearly with this velocity, this microvillus would be subject to a force, torque and tip deformation that was many times greater than its neighbors.

A rough estimate of the increase in this integrated tip force and tip deflection in the above example can be obtained by multiplying the height of the protrusion, 1 μm, by the average velocity on the protrusion, $\approx$ 75 μm/s, or 75 $\mu m^2/s$ and comparing this result with the corresponding calculation for a uniform microvillus. For the latter the thickness

of the fiber interaction layer is only 0.18 μm and the average velocity in this layer is ≈ 2 μm/s giving a product of 0.36 $\mu m^2/s$. The drag force on the tip and hence the torque on the microvillus would be roughly 75/0.36 or more than 200 times that of its neighbors. P_m in equation (2.35) would increase by 200 and the deflection of the 2.5 μm microvillus in Fig. 2.9 would increase from 3.78 nm to 0.75 μm or 750 nm. This displacement is ten times the spacing Δ between the microvilli. This simple calculation shows that small heterogenieties in the height of the microvilli will cause greatly amplified displacements of the microvilli tips and that the tips would be in constant contact with one another when subject to physiological flows.

The arguments just advanced for uniformity in microvilli length also apply for the unusual hexagonal regularity in microvilli spacing sketched in Fig. 2.2A. If this spacing were not regular each microvilli tip would experience a very different drag force. Fig. 2.5 is a plot of equation (2.19) where the solid fraction, c, has been related to the open spacing Δ between the microvilli using equation (2.20). It is evident from this figure that the dimensionless drag coefficient, $F/\mu U$, on the microvillus tip is very sensitive to the spacing Δ and that the stimulus from each microvillus would vary greatly if their distribution were random. Such regularity in ultrastructure would only make sense if the microvilli were relatively stiff and their deformation due to hydrodynamic forces was small compared to their spacing. The uniformity in height and regularity of spacing are, therefore, a necessary condition to minimize the tip deflection so that each microvillus is constrained in its motion to a localized region about its equilibrium position and adjacent tips do not interact.

It is clear from Fig. 2.5 that the drag force coefficient falls off rapidly as the open gap Δ increases. However, Fig. 2.5 also shows that the velocity at the microvillus tip, $U_m(R_L)$, increases nearly linearly with Δ as the microvilli density decreases. The net result is that the drag force per unit length at the microvilli tips is relatively insensitive to Δ and one can show there is a weak minimum (not shown) at Δ=130nm. The depth of the penetration of the tip boundary layer, however, also increases with Δ so that the integrated drag force on the tip increases as Δ decreases. This suggests that several competing factors determine the optimum spacing and length of the microvilli. The amplification of absorptive area along the apical surface decreases from 36 to 15 from the S1 to the S3 segment in mammalian tubules (Maunsbach, 1973) and this correlates with volume reabsorption. However, a given amplification can be achieved by either long microvilli that are less dense or short microvilli that are more dense. It is here that mechanical forces could play an important role. In our hypothesized mechosensory system one would anticipate that either the torque on the microvillus or its tip deflections are the critical measures of flow rate. Thus, if one wanted to keep torque constant one could decrease microvillus length while increasing the separation of the microvilli so as to increase the value of $U_m(R_L)$ and the drag at the microvilli tip. Similarly, a different flow-microvillus length relationship would emerge if one were to maximize deflection of the microvillus tip in equation (2.35). This optimal design requires further study.

From a mechanosensory viewpoint the stimulus could be either the bending deformation of the microvillus or the cytoskeletal structures that anchor the axial actin microfilaments to the intracellular cytoskeleton. We shall examine each of these possibilities. The model for microvillus bending provides insight into the first of these

possibilities. The predicted deformations of the microvilli in Fig. 2.9 are based on realistic models of the actin microfilament structure in Fig. 2.3A, taken from Maunsbach (1973), and a reliable estimate of the Young's modulus of individual F-actin filaments in Kishino and Yanagida (1988). The predicted maximum deflections of the microvilli at normal flow rates, 30 nl/min, are one to five percent of the microvilli diameter depending on microvilli length. The microvilli, therefore, act as remarkably stiff bristles whose deformation under flow is less than 0.2 percent of their length. This supports our initial assumption that the fluid flow through the microvilli and the resulting forces and torques can be calculated neglecting this deformation. Although this bending deformation is small we shall show next that it is sufficient to produce an intracellular biochemical response.

There is a large literature on the biochemical response of cells grown on elastic substrates that are then subjected to stretch. These studies typically show that biochemical responses are elicited only for strains (change in length over initial length) that are one percent or greater. This could be the opening of stretch sensitive ion channels in the membrane or the release of Ca^{++} from intracellular stores. When the microvillus bends there is a relative motion of the axial actin filaments and they slide past one another much like the pages of a paperback book when you bend its cover. The relative motion of the front and back cover is of the same order as the edge deflection and thus the relevant strain is the edge deflection divided by the total thickness of its pages. In the microvillus this relative motion would be transmitted via cross-linking molecules such as ezrin, which link the actin cytoskeleton to proteins in the plasma membrane or fimbrin and α-actinin which link the deforming actin fibers. The order of magnitude of the strain

on these cross-linking molecules would be the tip deformation divided by the microvillus diameter, which was one to five percent. These strains fall in the range where intercellular biochemical responses are elicited on cells stretched in vitro. In the present case a plausible candidate for the membrane protein is NHE3, the Na^+/H^+ exchanger located in the microvillus membrane (Lamprecht et al., 1998).

The second possibility is that the sensory stimulus is the torque exerted on the anchoring elements in the intracellular cytoskeleton. The ultrastructural arrangement of the microvilli is ideally designed to maximize this function. Nearly ninety percent of the torque is produced by drag forces acting at the microvilli tips. The long lever arm accentuates the moments on the intracellular cytoskeleton and the stiffness of the microvilli allows one to transmit this torque without a large deformation that would produce tip-tip interaction. Our basic assumption in solving equation (2.29) is that the microvillus acts like a cantilever beam which satisfies a rigid end condition (2.32), much like the roots of a tree fasten its trunk to the ground.

The total drag force acting on the microvillus for a control flow of 30 nl/min is 7.4×10^{-3} pN. This is about two orders of magnitude smaller than the drag forces applied by laser tweezers in moving proteins laterally in the plane of the membrane. Typically forces less than 0.1 pN are too small to hold the proteins in the laser trap when the tail of the protein interacts with the underlying microfilaments in the membrane skeleton (Sako et al., 1998). Forces of the order of 0.5 pN will cause a large deformation of the F-actin microfilaments that form the fence of the microdomains that restrict the diffusion of the membrane proteins. A significant rebound of the protein is observed if it escapes from the optical trap at a microdomain boundary. Thus, the hydrodynamic forces predicted by our

model are small compared to the dragging forces which create large deformations of the membrane cytoskeleton. This is consistent with our hypothesis that the longitudinal actin filaments do indeed provide sufficient stiffness to prevent the microvilli from undergoing large strains and that the underlying cytoskeleton beneath the apical membrane, which provides the anchoring support, can withstand the bending moments at the base of the microvilli.

If the microvilli are truly uncoupled then each microvillus acts as if it were a tall tree in a dense forest whose tops are blowing in the wind. The tree will experience its largest deflections at its top but is usually felled by toppling due to the large torque exerted on its roots. We believe the secret to the cytoskeletal amplification are the forces experienced by the actin filaments at the roots of the microvillus where it is fastened to the supporting structure in its terminal web, see Fig. 1.6. To determine this amplification let us return to Fig. 2.3A and consider the moment about the three central actin filaments in the midplane of the actin bundle at its base. This resisting moment must balance the torque about the base of the microvillus due to its hydrodynamic loading. As noted in Fig. 2.8, 86 percent of this total torque is due to the contribution P_mL arising from the tip layer interaction. This torque is resisted by the four off axis actin filaments in Fig. 2.3A. Two of the actin filaments are in tension and two are in compression and the lever arm about the three central filaments is $\sqrt{3}\,a/2$. If the force on each actin filament is P_t, where the subscript t stands for terminal web, the total resisting moment at the base is $\sqrt{3}\,P_t a$. Neglecting for the moment the contribution that arises from the distributed loading q_m in the brush border, one finds that if this mement is to resist the hydrodynamic torque at the microvillus tip, $P_t = (P_mL)/(\sqrt{3}\,a)$. a in our model is assumed to be 45 nm whereas L is

2500 nm. The force on the actin filaments at the base of the microvillus is amplified by a factor of 32 and, if the additional torque due to the distributed force q_m in the brush border is also included, this amplifcation factor increases to 38. Although the drag on the microvillus tip is only 0.0055 pN, the force on the microfilaments at the microvillus base are 38 times this or 0.21pN.

The 0.2 pN force just calculated is typical of the forces applied by optical tweezers in moving a protein laterally in the plane of the membrane when it is attached to a small bead in a laser trap. A force of 0.5 pN is required to produce a large deformation in a single actin filament strand in the microdomain fence model of Sako et al. (1998) for the restricted diffusion of proteins in the membrane of the bilayer. A 1.0 pN force is sufficient to release the bead-protein complex from its optical trap at the border of a microdomain. It is also obvious that if the microvilli were non-uniform in height, the forces on the microfilaments at their base would be so large that the supporting structure would easily buckle. P_m would increase 200 fold to 1.1 pN and P_t would be 38 times this, or 42 pN. Individual actin filaments could not support a compressive force of 42 pN.

The foregoing predictions demonstrate the quantitative feasibility of the kidney microvilli acting as a mechanotransducer for the sensing of flow. The model provides a rational explanation as to why the microvilli are so uniform in height and spacing and also provides an amplification mechanism that is required if the small drag forces acting on the microvilli tips are be transmitted as much larger tensile and compressive forces acting on the cytoskeletal elements in the terminal web region of the microvillus. The requirements of this mechanosensory system would appear to require that the microvilli

behave as relatively stiff bristles which are capable of small deflections wherein each microvillus does not interact with its neighbors.

One of the most attentive features of this new model is that it is able to take full advantage of the available information that has been gathered over the past few decades on the ultrastructure of the microvilli, their actin cytoskeleton and the physical parameters that determine both the hydrodynamic and elastic behavior. The limitation and uncertainty in the hydrodynamic model are minor since the spacing and regularity of the microvilli has been well documented. Similarly, the cytoskeletonal model for the bending of the microvilli sketched in Fig. 2.3, which idealized in the spacing of the axial actin filaments, is a quite realistic representation of the ultrastructure observation in (Maunsbach, 1973). The greatest uncertainty in the prediction of the model lies in the available measurement determining the Young's modulus E of the individual actin filament. The estimation of E has an order of magnitude uncertainty since the experimental techniques have been based on measurements of the flexural rigidity EI of single actin filament subject to either micromanupulation or Brownian deformation (Dupuis et al., 1997; Gittes et al., 1993; Kishino and Yanagida, 1988) and not direct measurement of E which is a derived quantity once the moment of itertia I of the actin filament has been estimated. The measured values of EI have varied from 15×10^3 pNnm^2 (Dupuis et al., 1997) to 73×10^3 pNnm^2 (Gittes et al., 1993) with the measurement of (Kishino and Yanagida, 1988) 17×10^3 pNnm^2 used in our calculation being close to the former. Since I varies as the fourth power of the effective radius of the filament, small variations in assumed cross-sectional geometry lead to substantial changes in I. In this study we have used the calculation in Satcher and Dewey (1996), which assumes an

effective radius of 3.5nm, since this corresponds closely to the measurements reported in Maunsbach and Christensen (1992) and Rostgaard and Thuneberg (1972). This gives a value of E of 0.14GPa. If the effective radius had been reduced 2.5nm, as assumed in Dupuis et al. (1997), E would be a factor of four larger and the microvilli tip deflections a factor of four smaller.

The theoretical predictions of our model suggest a relatively simple critical experiment that can be performed to test the basic hypothesis that the microvilli serve a mechanosensory function, namely to examine the effect of viscosity on reabsorption. If the flow rate is kept constant, but the viscosity of the perfusing fluid is increased, then the drag on the microvilli will increase and produce a larger drag on the microvilli tips. This should increase the torque on the microvilli and, if our hypothesis is correct, produce the same effect as increasing the flow rate. Additional biological information will be necessary, however, to formulate a complete signaling mechanism. While the axial actin structure of the microvillus has been known since the early 1970's, there is no equivalent information on how this microfilament skeleton is anchored into the intracellular cytoskeleton. Finally, much more needs to be learned about the relationship between the sensing mechanism and the interactions that lead to the entry of Na^+ across the apical membrane. In particular, the specific interactions between the proximal tubule cytoskeleton and the apical cell membrane Na^+/H^+ exchanger need to be elucidated.

Appendix A Slip Velocity at Microvilli Tips

In the interior of brush border the bulk flow velocity is uniform and there is no shear force at all. The dimensionless Brinkman equation (2.4) reduces to the Darcy equation and the dimensionless bulk velocity $u_{m,}$ is given by

$$u_m = -\frac{1}{\alpha^2}\frac{dp}{dz}. \tag{A1}$$

From equation (2.10) the dimensionless tip velocity is given by

$$u_{tip} = -\frac{1}{\alpha^2}\frac{dp}{dz}\cdot C_3. \tag{A2}$$

In the large α limit C_3 is given by (2.11c) and the dimensional slip velocity from (2.3) can be written as

$$U_{tip} = -\frac{K_p}{\mu}\frac{dP}{dZ}\cdot\frac{\alpha r_L}{2}. \tag{A3}$$

Using the definition of α and $r_{L,}$, one can write (A3) as

$$U_{tip} = -\frac{R_L}{2\mu}\frac{dP}{dZ}\cdot\sqrt{K_p}. \tag{A4}$$

Tsay and Weinbaum (1991) have shown that the Darcy permeability coefficient K_p is closely approximated by

$$K_p = 0.05732\times a^2\times\left(\frac{\Delta}{a}\right)^{2.377}. \tag{A5}$$

Substituting (A5) into (A4) the tip velocity is given by

$$U_{tip} = -\frac{R_L}{2\mu}\frac{dP}{dZ}\cdot\sqrt{K_p} = K\cdot\Delta^{1.189}. \tag{A6}$$

where K is a constant. Thus the tip velocity varies nearly linearly with Δ.

Appendix B

In this Appendix we develop a simple analysis to show the effect of absorption on equation (2.2). We assume that absorption across the proximal tubule is uniform.

The continuity equation for the brush border is

$$\frac{1}{R}\frac{\partial}{\partial R}(RU_{mR})+\frac{\partial U_{mZ}}{\partial Z}=0. \qquad \text{(B1)}$$

One notice that the magnitude of second term is << the first term. First, the axial length scale Z, whose value is ~ 1cm, the length of the proximal tubule, is >> the radial length scale R, 2.5μm, the thickness of the brush border. Second, the absorptive velocity U_{mR}, which is ~ 0.3μm/s at a perfusion rate of 30 nl/min, is nearly 30 times larger than the axial velocity in the brush border U_{mZ}, 10 nm/s, see Fig. 2.4. After neglecting the second term, one has

$$\frac{1}{R}\frac{\partial}{\partial R}(RU_{mR})=0. \qquad \text{(B2)}$$

Equation (B2) can be integrated such that

$$U_{mR}=\frac{R_0U_0}{R}. \qquad \text{(B3)}$$

Here R_0 is the radius of the tubule (lumen radius plus brush border height) and U_0 is the uniform absorption velocity. To obtain (B3) we have applied the boundary condition that $U_{mR}(R_0)=U_0$. Equation (B3) applies throughout the entire tubule length if we assume that absorption is uniform along the tubule length. From (B3), the radial absorption in the brush border can be modeled as the flow from a line source of uniform strength in which U_{mR} does not depend on Z.

The Brinkman equation in the radial direction for the brush border is given by

$$\frac{\partial P}{\partial R} = \mu \frac{1}{R} \frac{\partial}{\partial R}\left(R \frac{\partial U_{mR}}{\partial R} \right) - \frac{\mu_0 U_{mR}}{K_P}. \tag{B4}$$

We have neglected the axial term $\mu \frac{\partial^2 U_{mR}}{\partial^2 Z}$ in the Laplacian because its magnitude is much smaller than the radial term. Differentiating equation (B4) with respect to Z which U_{mR} is given by (B3), one has

$$\frac{\partial}{\partial Z}\left(\frac{\partial P}{\partial R} \right) = \mu \frac{1}{R} \frac{\partial}{\partial R}\left(R \frac{\partial}{\partial R}\left(\frac{\partial U_{mR}}{\partial Z} \right) \right) - \frac{\mu_0}{K_P} \frac{\partial U_{mR}}{\partial Z} = 0 \tag{B5}$$

Changing the order of differentiation, one finds

$$\frac{\partial}{\partial R}\left(\frac{\partial P}{\partial Z} \right) = 0. \tag{B6}$$

Thus, the axial pressure gradient is independent of R and equation (2.2) is also valid for an axial flow with uniform absorption. A similar analysis can also be applied to the core flow given by equation (2.1) with the result that the axial pressure gradient is constant across the tubule cross-section although the pressure from (B5) varies across the brush border and the radial velocity in this later is significantly greater than the axial velocity. One can show that the same would be true for a slowly varying axial absorption.

Table 2.1 Effects of changing flow rate in individually perfused tubules.

Ultrastructural data taken from Maunsbach (1987).

	low flow rate	control	high flow rate
flow rate (nl/min)	5	30	45
luminal diameter (μm)	17	27.7	31.6
distance between MVs (nm)	62.1	74.1	90.4
MV density (per square μm)	49.9	42.5	35.5
solid fraction	0.3175	0.273	0.226
permeability coefficient (m^2)	1.93×10^{-16}	2.93×10^{-16}	4.76×10^{-16}
α	792	955	839
total force on each MV (pN)	3.93×10^{-3}	7.40×10^{-3}	8.20×10^{-3}
total torque on each MV (pN*μm)	8.45×10^{-3}	1.59×10^{-2}	1.76×10^{-2}
effective shear force (dyn/cm^2)	1.96	3.14	2.91
maximum deflection (nm)	2.01	3.78	4.2

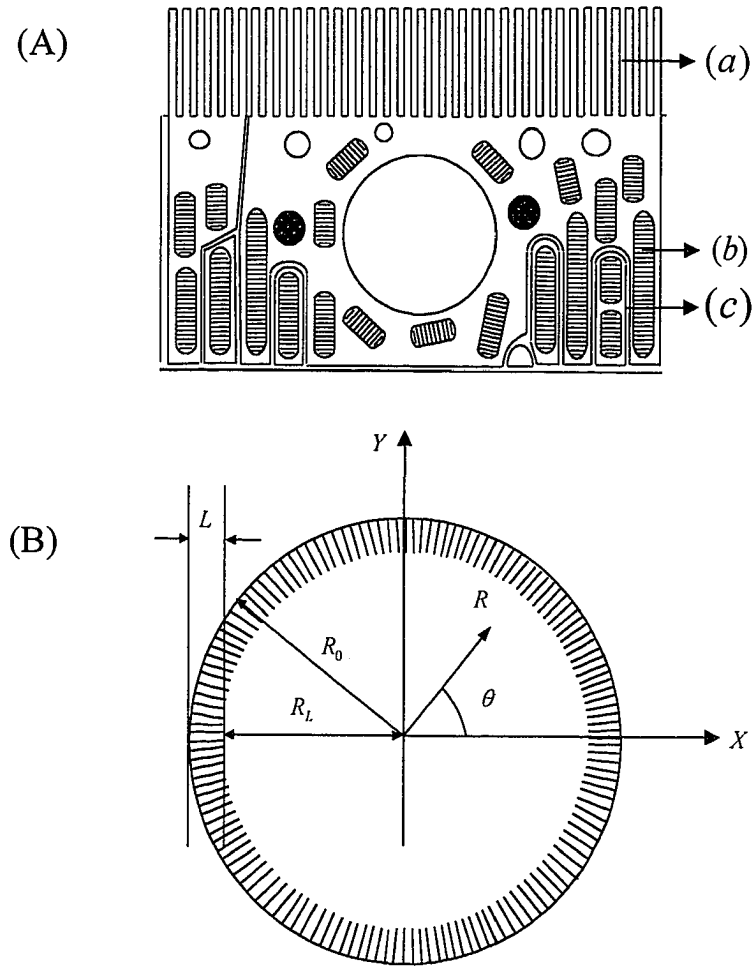

Figure 2.1 (A) Schematic diagram of an epithelial cell in proximal tubule S2 segment. The cells in this segment are characterized by densely spaced microvilli (a), numerous mitochondria (b), and extensive interdigitation of the lateral membrane near the basal surface (c). (B) Idealized mathematical model of tubule cross-sectional geometry, with brush border of thickness L.

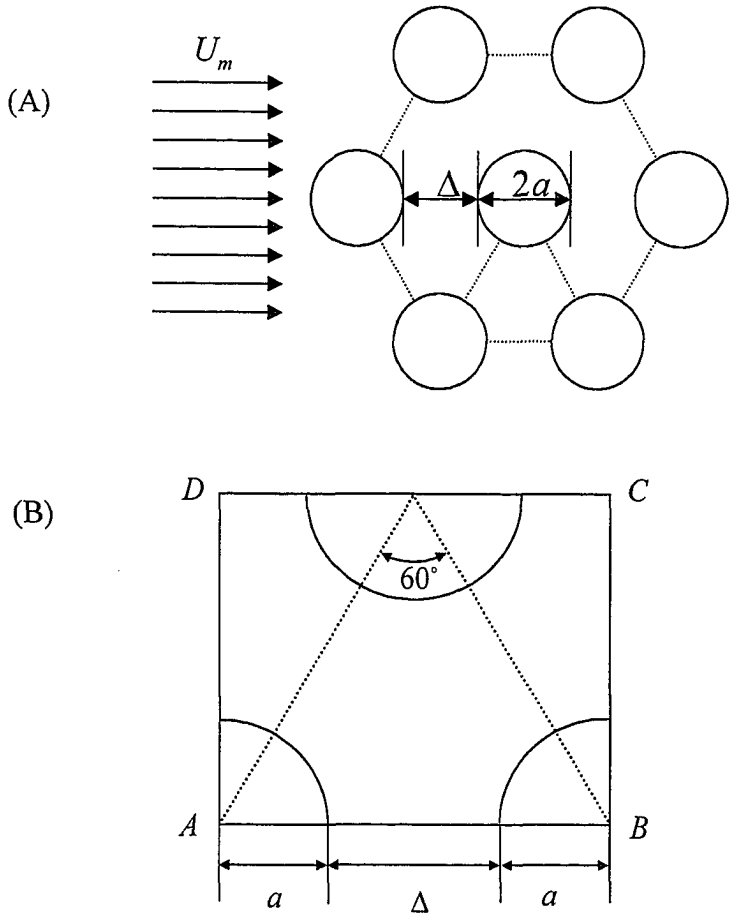

Figure 2.2 (A) Idealized model of brush border in transverse section showing hexagonal microvillus array. (B) Repetitive periodic unit of the hexagonal microvillus array. Note that this unit contains the equivalent of one microvillus.

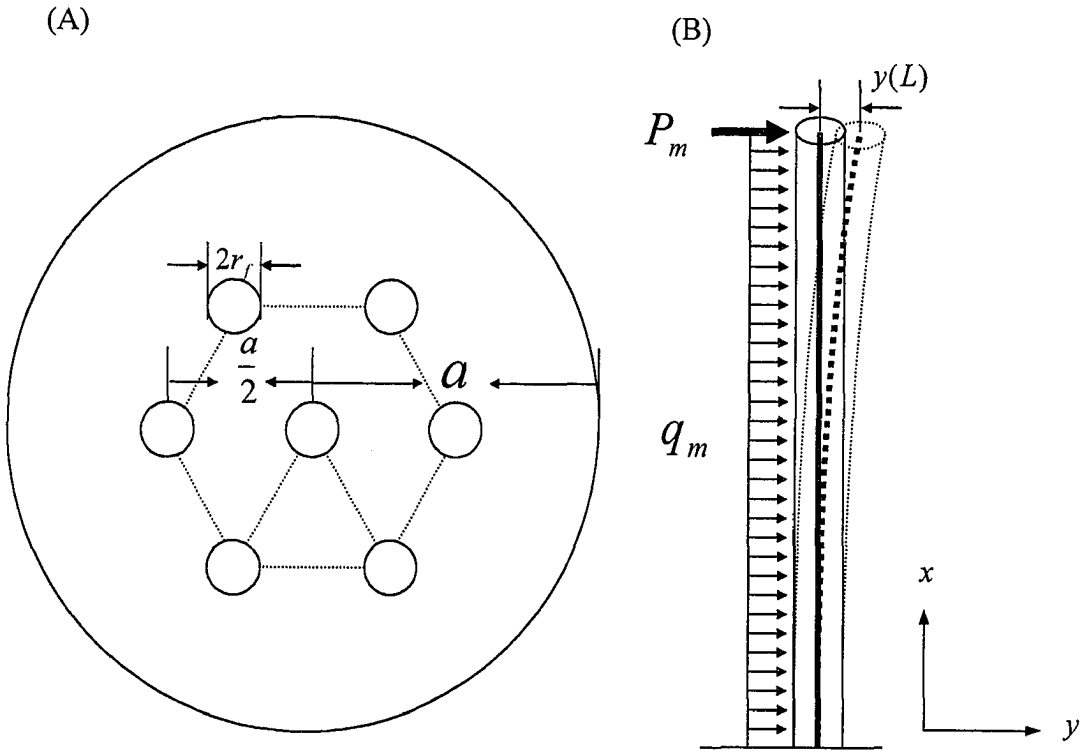

Figure 2.3 (A) Idealized structural model for the arrangement of axial F-actin filaments in microvillus cross section. The seven F-actin filaments form a hexagonal array in which the six off axis filaments are equally spaced on a circle that is the half radius of the cross-section. a is the radius of the microvillus membrane and r_f is the radius of the actin filament. (B) Geometry of the deformed microvillus showing axial deflection of its central filament. The mechanical loading is a combination of a concentrated force, P_m, acting at the tip, accounting for approximately three-quarters of the total force and a uniform loading, q_m, accounting for approximately one-quarter of the total force.

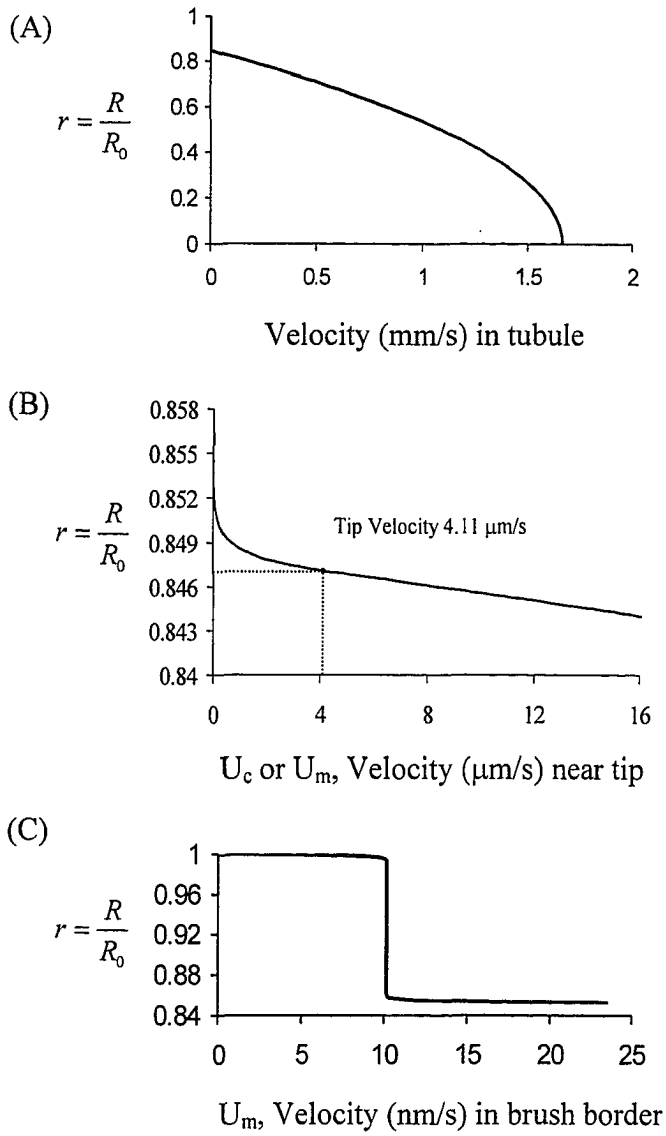

Figure 2.4 Velocity profiles (A) in lumen, (B) in tip region and (C) in central region of brush border. Tip is located at r=0.847. Note that velocity at microvilli tip is approximately 1/400 the center line velocity in core and bulk flow in brush border is approximately 1/400 of the tip velocity.

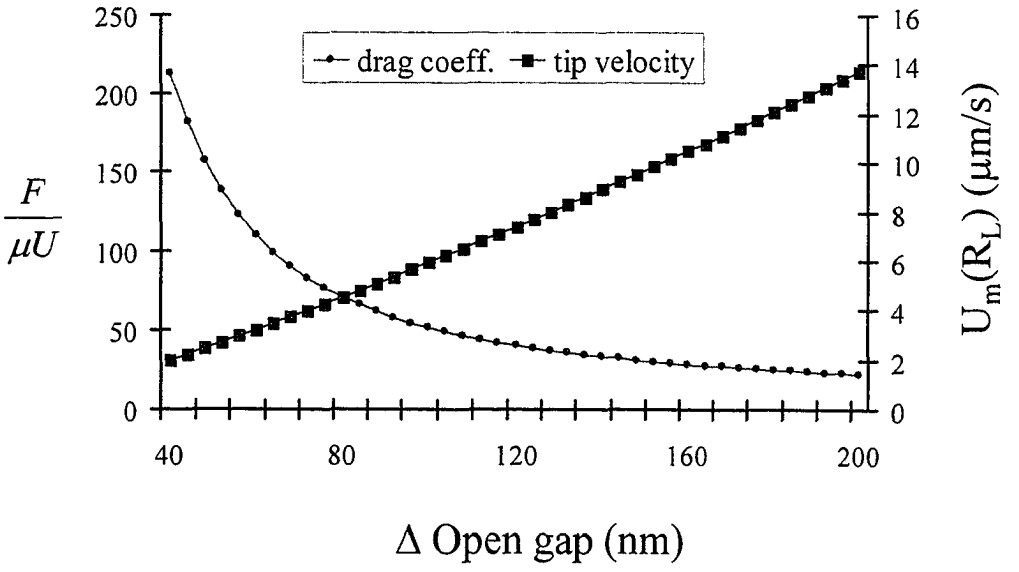

Figure 2.5 Dimensionless drag force coefficient ($F/\mu U$) and tip velocity $U_m(R_L)$ versus open gap between microvilli.

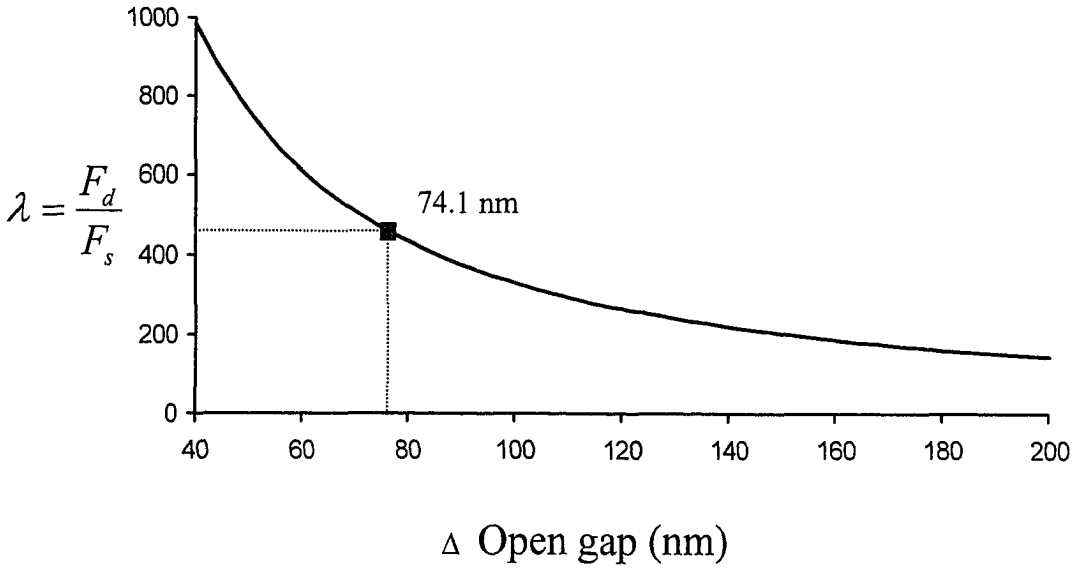

Figure 2.6 Plot of equation (25) for the ratio λ of the drag force F_d on the brush border microvilli and the shear stress F_s on the apical membrane per unit length of tubule. Note λ depend only on tubule and brush border geometry and is independent of both viscosity and flow rate. λ varies between 360 and 580 for the values of Δ measured in Maunsbach (1987).

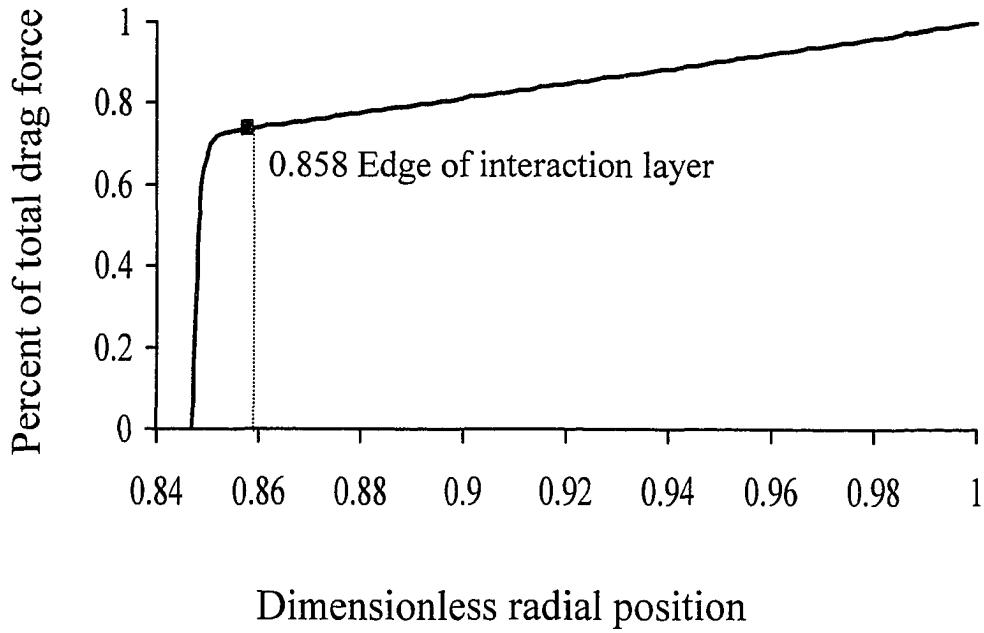

Figure 2.7 Integrated drag force distribution along the microvillus starting from the microvillus tip. Note that tip boundary layer is about 7 percent (0.18 μm) of microvillus length and 73.8 percent of the total drag force is concentrated in the tip region.

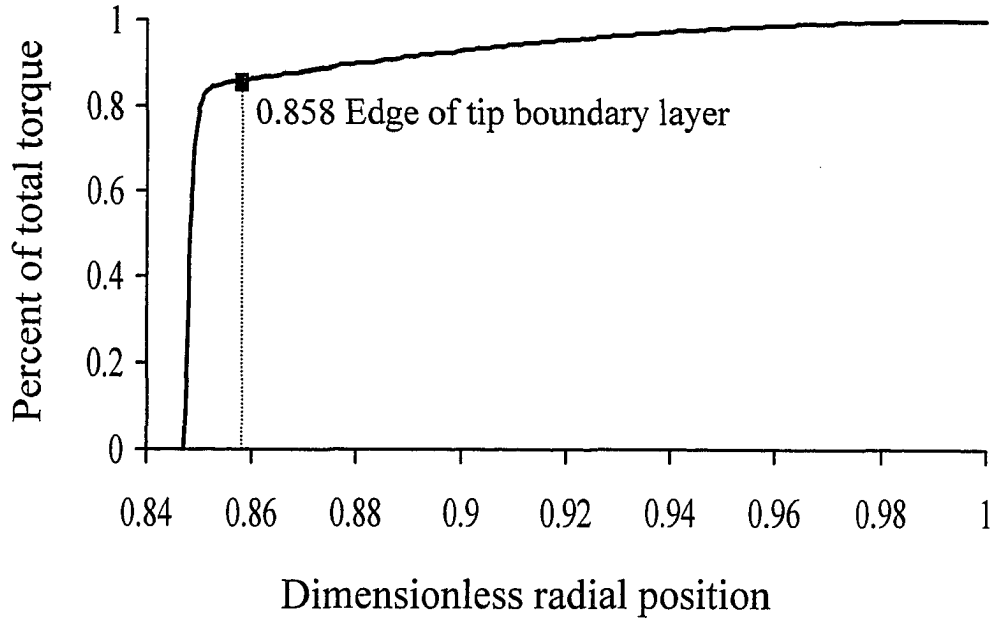

Figure 2.8 Integrated torque distribution along the microvillus starting from the microvillus tip. Note that 86.2 percent of the total torque occurs in the tip boundary layer, outer 0.18 μm of microvillus near tip.

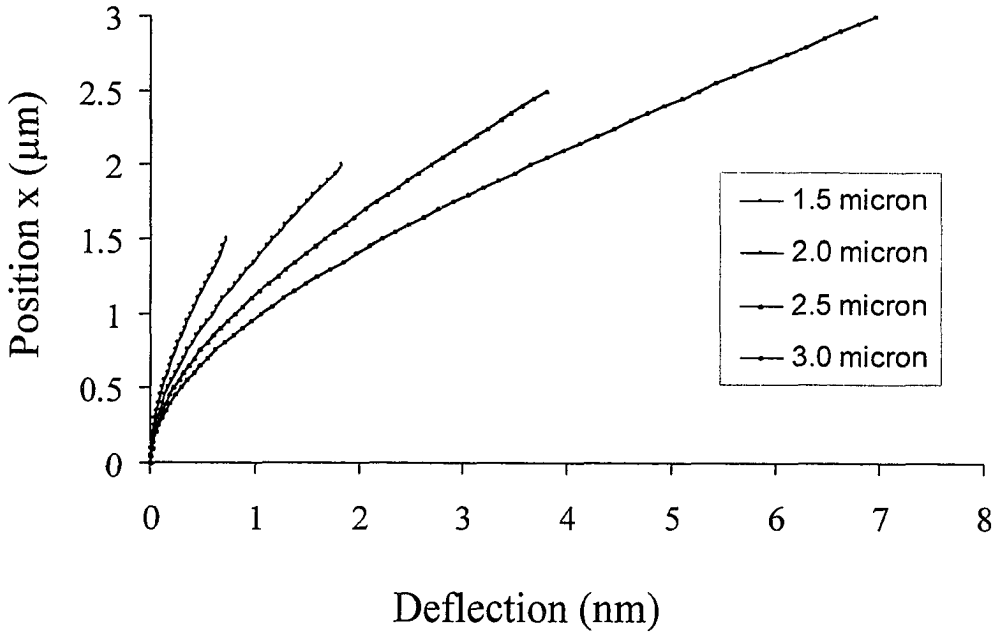

Figure 2.9 Microvillus deflection for control flow, 30 nl/min, for microvilli of four different lengths from 1.5 to 3.0 μm. $2R_L$=27.7 μm and Δ= 74.1 nm for all microvilli.

Chapter 3 Water transport across the tight junction

§ 3.1 Introduction

Water and solutes can traverse the proximal tubule epithelium of mammalian kidney via both transcellular and paracellular routes. The tight junction (TJ) complex forms the major barrier in the paracellular route, and its ability to seal the paracellular route is variable. In freeze-fracture electron micrographs, the TJ appears to be a set of long, parallel and linear fibrils which bifurcate to form an interconnected network. These fibrils consist of junction proteins of the claudin family and occludin (Tsukita and Furuse, 2000; Tsulita and Furuse, 1999; Fanning et al., 1999). Several species of claudins interspersed with occludin from one cell may copolymerize to form a strand in a side-by-side manner (Furuse et al., 1999). Strands from neighboring cells form a pair in a head-to-head homotypic or heterotypic interaction (Tsukita and Furuse, 2000; Furuse et al., 1999). Freeze-fracture electron microscopic observations show that the TJ of rat proximal tubule consists typically of a two strand complex that is shallow (~100 nm) in the apical-basal direction and that these strands exhibit discontinuities that can exceed 0.1 μm in length (Orci et al., 1981).

While there are two basic transport routes, transcellular and paracellular, the relative importance of each route for water has never been satisfactorily resolved. The paracellular route, in particular, has offered a substantial challenge since the structural correlate for the different size pores or their frequency and cross-sectional geometry are still unknown. Preisig and Berry (1985) concluded that the paracellular water permeability can not be more than 2 percent of the transepithelial water permeability.

They measured the permeabilities of mannitol and sucrose, which are believed to traverse the epithelium only via the paracellular pathway, and then used single pore/slit theory (Renkin equation) to predict the dimensions of the pores/slits which satisfied the permeabilities for both solutes. The TJ water permeability was then predicted using these pore/slit dimensions. Weinstein (1984) argued that the paracellular water permeability should be comparable to that of the transcellular pathway to accommodate the low transepithelial NaCl reflection coefficient. In his compartment model (Weinstein, 1984), the water permeability for the TJ has a value which is one and a half times that of the measured transepithelial water permeability. The additional hydraulic resistance is associated with the lateral interspace and solute polarization by the basement membrane.

The pore/slit theoretical approach was questioned by Fraser and Baines (1989) because they noted that pore/slit theory underestimated the water permeability of man-made gel membranes compared to the fiber matrix model developed by Curry and Michel (1980). They (Fraser and Baines, 1989) introduced a fiber matrix model based on the theory of Curry and Michel (1980) to estimate the TJ water and solute permeability. In their model, the TJ is modeled as a homogeneous fiber matrix gel with polymers of several nm radius which fill the space between the TJ strands. The model provides a consistent picture for rabbit proximal tubule, but when applied to the rat proximal tubule, it predicted small ion permeabilities which were an order of magnitude smaller than those measured. This model treated the TJ complex as a uniform structure without discontinuities. It, therefore, did not allow for the possibility of low-resistance large pore/slit pathways. In addition, the model was applied to a matrix that filled the space between the strands and not to the strands themselves. In the present study, it is the

strands themselves which account for most of the paracellular resistance for solute transport.

In this chapter we propose an ultrastructural model for the TJ strands, which consists of infrequent large slit breaks and numerous small circular pores. We also require that this model be consistent with the parameter selection in the compartment model in Weinstein (1984). In the next section we reconsider the single pore/slit analysis, as it applies to NaCl permeability, as well as to the passage of mannitol and sucrose. We then introduce a dual pathway model, and its additional parameters (pore/slit dimensions and frequency) are used to represent TJ attributes, which had been previously estimated (Weinstein, 1984; Weinstein, 1987). It will be argued that the pore/slit attributes are morphologically realistic.

§ 3.2 Single pore/slit model

§ 3.2.1 Solute permeabilities

We first examine a single pore/slit theory for compatibility with the transepithelial water permeability, the TJ solute permeabilities and the NaCl reflection coefficient for the entire epithelium. This means estimating the dimensions of the pores or slits in the TJ strands that are required to satisfy the measured permeabilities of both small ions and nonelectrolytes. For a pore, the critical parameters are the pore radius R_P and the total pore area per unit surface area/pore depth, A_p/δ. For a slit the corresponding parameters are the slit height W and the total slit area per unit surface area/slit depth, A_l/δ. We modify the approach in Preisig and Berry (1985), who used the TJ permeabilities of sucrose and mannitol to determine the dimensions of the paracellular pathway. In their

approach, they apply the Renkin equation to two solutes, mannitol and sucrose, whose radii are close in size, 3.6 and 4.6 Å, respectively. Alternatively, it should provide better discrimination in pore/slit dimensions to use permeabilities of solutes with large variation in their radii, such as salt and either mannitol or sucrose. NaCl permeability data has been obtained by many investigators and the radius of NaCl differs significantly from both sucrose and mannitol. Thus, we can use TJ permeability for NaCl together with that for either sucrose or mannitol to determine the dimensions of a pore/slit paracellular pathway.

In single circular pore theory, the water and solute permeabilities of the TJ strands, L_{TJ}(pore) and H_{TJ}(pore), respectively, are given by

$$L_{TJ}(pore) = \frac{A_p \times R_p^{\,2}}{8\mu\delta}, \tag{3.1}$$

$$H_{TJ}(pore) = \frac{A_p \times D_{pore}}{\delta}. \tag{3.2}$$

Here δ is the pore depth, R_p the pore radius, A_p the total pore area per unit surface area and μ the viscosity of water, whose assumed value is 0.0007 Pa·s. D_{pore} is the diffusion coefficient for a solute in a circular pore. An empirical expression, the Renkin equation (Preisig and Berry, 1985), is used to relate D_{pore} to the free diffusion coefficient, D_{free}, and a, the solute radius.

$$\frac{D_{pore}}{D_{free}} = \left(1-\frac{a}{R_p}\right)^2 \times \left(1-2.104\frac{a}{R_p}+2.09\left(\frac{a}{R_p}\right)^3-0.95\left(\frac{a}{R_p}\right)^5\right). \tag{3.3}$$

There are two multiplicative factors in equation (3.3). The first factor, $\left(1-\frac{a}{R_p}\right)^2$, is the partition coefficient, representing the steric exclusion from the pore. The second factor

describes the hydrodynamic interaction of the solute with the pore walls. From equation (3.2)

$$\frac{H_{TJ}(pore)}{D_{pore}} = \frac{A_p}{\delta}. \tag{3.4}$$

Using measured permeabilities for two distinct solute species, equations (3.3) and (3.4) provide a means of calculating R_p and A_p/δ for a single pore pathway. The left-hand side of equation (3.4) is a function of the solute permeability, H_{TJ}, solute radius, a, and pore radius R_p. If two solutes share the same transport pathway, then R_p and A_p/δ will be the same for that pathway. Thus, the right hand side of (3.4) will have the same value for these two solutes and the left-hand side of (3.4), when plotted as a function of R_p, will yield a compatible solution for R_p, provided the two curves for $\frac{H_{TJ}}{D_{pore}}$ intersect.

Preisig and Berry (1985) measured the permeabilities of sucrose and mannitol which are believed to traverse the epithelium only via the paracellular route. These measured permeabilities are: $H_{TJ}(\text{mannitol})=0.87\times10^{-5}$ cm/s, $H_{TJ}(\text{sucrose})=0.43\times10^{-5}$ cm/s. The estimated TJ permeability for NaCl is $H_{TJ}(\text{NaCl})=13\times10^{-5}$ cm/s (Weinstein, 1984). Thus, we can plot three curves for the left hand term of equation (3.4) for NaCl, mannitol and sucrose as a function of pore radius (Fig. 3.1A). The intersection of any two curves provides a compatible pore radius which satisfies the Renkin equation for those two solutes. In this calculation the Stokes-Einstein radii for NaCl, mannitol and sucrose are 1.47Å, 3.6Å and 4.6Å, respectively. Their corresponding free diffusion coefficients are 2.21×10^{-5} cm^2/s, 0.90×10^{-5} cm^2/s and 0.70×10^{-5} cm^2/s.

The solutions for the pore radius R_P obtained from the intersections of the curves in Fig. 3.1A are summarized in Table 3.1A. A_P/δ can then be found using equation (3.4)

and L_{TJ} calculated using equation (3.1). These results are also given in Table 3.1A. Our results for pore radius and water permeability which satisfy mannitol and sucrose permeabilities are the same as the results given previously by Preisig and Berry. This water permeability is less than 2 percent of the measured total transepithelial water permeability, 0.12-0.15 cm/s [††] (Preisig and Berry, 1985). Although the single pore model predicts slightly larger TJ water permeabilities, 0.0023 and 0.0028 cm/s, when computed using NaCl/mannitol and NaCl/sucrose pairs rather than a mannitol/sucrose pair, 0.0018 cm/s, the values are still less than 3 percent of the transepithelial water permeability.

Similarly, a single slit model can be used to estimate the slit height and the total area of open slit per unit surface area/slit depth. Again we assume all solutes share the same transport pathway. In the slit model, the water and solute permeability, $L_{TJ}(slit)$ and $H_{TJ}(slit)$, respectively, are given by

$$L_{TJ}(slit) = \frac{A_l \times W^2}{12\mu\delta}, \tag{3.5}$$

$$H_{TJ}(slit) = \frac{A_l \times D_{slit}}{\delta}. \tag{3.6}$$

Here δ is the depth of the slit, A_l is the total slit area per unit surface area of epithelium and W is the height of the slit. D_{slit}, the solute diffusion coefficient for an infinite slit, is

[††] Two sets of units, cm/s and cm/s/mmHg, are used in this paper to describe the water permeability. The relation between them is

$$P_f = \frac{RTL_P}{V_W}.$$

Here P_f is the water permeability in cm/s and L_P is the water permeability in cm/s/mmHg. V_W is the molar volume of water, V_W=18 cm^3/mole, R=8.3145 J/mole/^{0}K and T=310.15^{0}K. For a water permeability L_P of 1×10^{-7} cm/s/mmHg, the corresponding P_f=0.107 cm/s.

given by the Renkin equation (Preisig and Berry, 1985),

$$\frac{D_{slit}}{D_{free}} = \left(1 - \frac{2a}{W}\right) \times \left(1 - 1.004\frac{2a}{W} + 0.418\left(\frac{2a}{W}\right)^3 - 0.169\left(\frac{2a}{W}\right)^5\right). \quad (3.7)$$

The first factor in equation (3.7), $1 - \frac{2a}{W}$, describes the steric exclusion and the second the increased hydrodynamic resistance of the slit walls. From equation (3.6),

$$\frac{H_{TJ}(slit)}{D_{slit}} = \frac{A_l}{\delta}. \quad (3.8)$$

Following the same argument as in circular pore theory, we have plotted in Fig. 3.1B the left hand side of equation (3.8) versus the slit half height W/2 for three solutes, NaCl, mannitol and sucrose. The intersections of the curves provide the solutions to equation (3.8) for each solute pair. In these calculations, the solute permeabilities H_{TJ} are the same as used previously for the pore calculations. The solutions for the slit half height W/2 obtained from the intersections of the curves in Fig. 3.1B are summarized in Table 3.1B. A_l/δ can then be found using equation (3.8) and L_{TJ} calculated using equation (3.5). The results summarized in Table 3.1B are similar to those for a circular pore. L_{TJ}(slit) for the mannitol/sucrose pair is approximately 1.5 percent of the transepithelial water permeability L_p, as previously predicted in Preisig and Berry. Although L_{TJ}(slit) for NaCl/mannitol pair or NaCl/sucrose pair, 0.0018 and 0.0023 cm/s, is a little larger than that for sucrose/mannitol pair, 0.0013 cm/s, it is still less than 2 percent of L_P. Thus, neither a pore model nor a slit model predicts values for L_{TJ} which are a significant fraction of the transepithelial water permeability.

§ 3.2.2 Salt reflection coefficient, σ(NaCl)

Instead of using solute permeability pairs to determine pore or slit dimensions, one can use the transepithelial water permeability, L_P, the TJ salt permeability, $H_{TJ}(NaCl)$, and the transepithelial reflection coefficient σ for NaCl for the entire epithelium to determine the dimensions of the paracellular pathway. Experiments show that the rat proximal tubule epithelium has a reflection coefficient for NaCl that is close to 0.7 (Ullrich, 1973). Accordingly, we shall attempt to satisfy the measured values of L_p, σ and the TJ NaCl permeability, but relax the constraints on the nearly impermeant solutes, sucrose and mannitol. For a single pore/slit model for the TJ one assumes that water and NaCl will traverse the TJ sharing the same pore or slit pathway. This approach leads to pores or slits which are much larger and less frequent than the single pore/slit model just considered for paired solutes, but one finds the permeabilities for sucrose and mannitol are far too large, as we show next.

There is no directly measured value for the TJ water permeability L_{TJ}. However, a compartment model has been used to relate L_{TJ} to L_P, the measured transepithelial water permeability (Weinstein, 1984). In compartment models the properties of the entire epithelium are determined by the properties of its components, the cell barrier, the TJ barrier and the basement membrane barrier (Fig. 3.2). Conversely, the overall epithelial permeabilities will serve as constraints for determining the component parameters, and these have been displayed in Table 3.2A. The values for L_P, σ, and H used in the model of Weinstein (1984) were all taken from those compiled by Ullrich (1973). Preisig and Berry (1985) subsequently determined an overall L_P about half that found by Ullrich, and a lower value is used in the current model. The reflection coefficient for the cell

membrane is 1.0 (Pearce and Verkman, 1989; Van-der-Goot et al., 1989), and 0.0 for basement membrane (Welling and Grantham, 1972). The rate of active osmolar transport across the basolateral membrane, N, was taken to be approximately twice the rate of net epithelial sodium transport (Ullrich, 1973). For the diffusive salt permeability of tight junction, H_{TJ}, the value selected (if applied to both sodium and chloride) yields a realistic estimate for tight junctional electrical resistance (Fromter, 1979). Isotonicity of proximal tubule volume transport is embodied in the parameter, C*, which is the decrement in luminal osmolality required to yield a reabsorbate osmolality equal to that of the lumen. Experimental determinations of luminal osmolality indicate that that this value is no greater than 2-3% of blood osmolality, but more precise definition has not been possible. Its exact value may vary with peritubular protein concentration and luminal anion composition, but model calculations indicate that C* depends largely on the overall rate of sodium reabsorption relative to cell membrane water permeability (Weinstein, 1984).

For this initial calculation, consider the cell barrier and the TJ barrier in parallel, and omit for simplicity the resistance of the highly permeable basement membrane barrier. For this simplified composite pathway model, the transepithelial water permeability and the reflection coefficient for NaCl, L_P and σ, respectively, are given by (Weinstein, 1987)

$$L_P = L_C + L_{TJ}, \tag{3.9}$$

$$\sigma = \frac{L_C\sigma_C + L_{TJ}\sigma_{TJ}}{L_P}. \tag{3.10}$$

Here L_C is the water permeability of the cell barrier, L_{TJ} is the water permeability of the TJ, σ_C is the NaCl reflection coefficient of the cell barrier and σ_{TJ} is the NaCl reflection

coefficient of the TJ barrier. Reasonable values for σ and σ_C for NaCl are σ=0.7 and σ_C=1.0, as stated above. From equation (3.10) we can see that if $L_{TJ}/L_P << 1$, σ is close to 1 rather than 0.7.

Combining (3.9) and (3.10), one has

$$\frac{L_{TJ}}{L_P} = \frac{0.3}{1-\sigma_{TJ}}. \tag{3.11}$$

According to pore theory the reflection coefficient can be written as (Michel and Curry, 1999)

$$\sigma_{TJ} = (1-\phi)^2. \tag{3.12}$$

Here ϕ is the partition coefficient, which for a circular pore is given by (Michel and Curry, 1999)

$$\phi = \left(1-\frac{a}{R_P}\right)^2. \tag{3.13}$$

Combining (3.11), (3.12) and (3.13), we find that

$$L_{TJ} = \frac{0.3}{1-\sigma_{TJ}} \cdot L_P = \frac{0.3}{1-\left(1-\left(1-\frac{a}{R_P}\right)^2\right)^2} \cdot L_P. \tag{3.14}$$

From equations (3.1) and (3.2), we have two independent relations for A_P/δ

$$\frac{A_P}{\delta} = \frac{L_{TJ}(pore) \times 8\mu}{R_p^{\,2}}, \tag{3.15a}$$

$$\frac{A_P}{\delta} = \frac{H_{TJ}(NaCl)}{D_{pore}}. \tag{3.15b}$$

After we substitute equation (3.14) into equation (3.15a), the only unknown variable on the right hand side of (3.15a) is the pore radius R_P. Similarly, the only unknown on the right hand side of (3.15b) is R_P if we know the solute permeability H_{TJ} and the solute radius a (equation 3.3). If water and solute share the same transport pathway, A_p/δ must be the same for that pathway. Thus, if we plot the right hand sides of (3.15a) and (3.15b) versus the pore radius, the intersection of two curves provides the compatible pore radius (Fig. 3.3A). This compatible solution for L_P=0.15 cm/s, H_{TJ}(NaCl)=13×10^{-5} cm/s, σ=0.7 and a=0.147 nm, is R_P = 5.2 nm. Once the pore radius is determined, we can use either (3.15a) or (3.15b) to obtain A_P/δ, 6.64 cm^{-1}. Because the predicted A_P/δ now is nearly half the predicted values for NaCl/mannitol and NaCl/sucrose pair in Table 3.1A and the predicted R_P here is at least five times greater than the values predicted in Table 3.1A, there are many fewer pores in the TJ strands when we try to satisfy the measurements for NaCl and water permeability. The permeability of any solute can now be calculated using equation (3.2). The corresponding permeabilities of sucrose and mannitol are H_{TJ}(mannitol)= 4.42×10^{-5} cm/s, H_{TJ}(sucrose)=3.16×10^{-5} cm/s. These permeabilities are 5.0 (mannitol) to 7.4 (sucrose) times greater than the experimental values in Preisig and Berry (1985). The predicted pore radius R_P is much greater than the sodium radius. Thus, from equations (3.12) and (3.13), the TJ reflection coefficient for NaCl, σ_{TJ}, is close to zero. From equation (3.11), the tight junction water permeability L_{TJ} is nearly 30 percent of the transepithelial water permeability L_P.

A similar analysis can be performed for the single slit model and the slit dimensions for the TJ can be determined using the same values for L_P, H_{TJ}(NaCl) and σ

as for the circular pore. To simplify our calculation we assume the reflection coefficient of the tight junction is zero because we anticipate that the slit height W >> 2a and $\sigma_{TJ} \sim 0$. Thus, from equation (3.11), $L_{TJ} \sim 0.3\ L_P$.

From equations (3.5) and (3.6),

$$\frac{A_l}{\delta} = \frac{L_{TJ}(slit) \times 12\mu}{W^2}, \tag{3.16a}$$

$$\frac{A_l}{\delta} = \frac{H_{TJ}(NaCl)}{D_{slit}}. \tag{3.16b}$$

The right hand sides of (3.16a) and (3.16b) are plotted versus W/2 in Fig. 3.3B for the same values of L_P and H_{TJ} as for the circular pore. One finds that the compatible slit half height, W/2, is 3.2 nm and A_l/δ, from (3.16a) or (3.16b), is 6.5 cm^{-1}. This value of W/2 is at least 5 times greater than the values in Table 3.1B. The predicted slit half height W/2 =3.2 nm is much larger than the sodium radius. Thus, our assumption, that σ_{TJ} is close to zero, is valid. Once W and A_l/δ are determined, the corresponding permeabilities of sucrose and mannitol can be determined using equation (3.6). They are: H_{TJ}(mannitol)=4.6×10^{-5}cm/s, H_{TJ}(sucrose)=3.4×10^{-5}cm/s. These permeabilities are again 5.3 (mannitol) to 7.8 (sucrose) times larger than the experimentally measured values in Preisig and Berry (1985).

§ 3.2.3 Conclusion for single pore/slit model

These model calculations indicate that a single pore/slit model can not satisfy the well-documented experimental measurements for the transepithelial water permeability, the TJ solute permeability and the overall reflection coefficient for small ions for rat proximal tubule. The calculations in subsection 1) suggest that the dimensions of the

single pore/slit based on TJ solute permeability alone are rather small. This small pore/slit will offer a great resistance for water transport and account for less than three percent of the measured L_P. Thus, L_{TJ} contributes insignificantly to L_P. The calculations in subsection 2), which are based on L_P and σ for small ions for the entire epithelium, suggest that pores or slits whose dimensions are at least a factor of five larger are required to accommodate L_P and σ. However, these larger pores/slits predict a much larger solute permeability for sucrose and mannitol than the experimental values. Thus, a single pore/slit model is unable to reconcile all the experimental data.

§ 3.3 Dual pore/slit model

§ 3.3.1 TJ barrier in a compartment model

These contradictions lead to consideration of a dual-pathway ultrastructural model to reconcile the junctional permeabilities of water, ions and small nonelectrolytes. Our proposed model for the TJ strands contains two parallel transport pathways: infrequent large slit breaks formed by junction strand discontinuities and numerous small circular pores in the claudin-occludin TJ complexes. The large slit allows for a significant passage of water. Most importantly, these junctional strand breaks, which allow for flow through a double strand complex, are very few in number. This transport pathway will also allow small ions to pass, but it is not the dominant route for ions because of the very low probability that an open pathway will be formed by breaks in a TJ complex of two or more strands. Numerous small circular pores are the primary pathway for small ions. This small pore pathway allows for a solute flux for molecules < 1.0nm diameter, but offers a large resistance for the passage of water. The key idea in the model is the distinction

between volume (water) and solute transport pathways. One can not use the solute transport pathway to estimate the water permeability, nor the small pore pathway to evaluate non-electrolyte permeability and water permeability. The heterogeneity in ultrastructure also provides an alternative view to the fiber matrix model of Fraser and Baines (1989).

Experimental data from rat proximal tubule are for the transepithelial permeabilities of water and salt, and for the transepithelial NaCl reflection coefficient. Therefore, a compartment model will be used first to estimate L_{TJ} and σ_{TJ} from the whole epithelial coefficients. Of note, the cell in this model is treated as a barrier in parallel with the junctional pathway. Compartment models for rat proximal tubule epithelium were introduced to explore the potential significance of a permeable tight junction (Weinstein, 1981). The compartment model was later extended to include the compliance of the lateral intercellular space (Weinstein, 1984) and the impact of TJ convection in the epithelial transport equations (Weinstein, 1987). In this study we shall apply the 1984 compartment model to provide an estimate of the properties of the TJ barrier.

In the compartment model of Weinstein (1984) the cells and the TJ are in parallel and form a composite barrier, which are both in series with a lateral interspace basement membrane, Fig. 3.2. In this model the cell itself is a barrier, not a compartment. In Weinstein (1984) the transepithelial water permeability L_P, the transepithelial NaCl permeability, H, and the NaCl reflection coefficient, σ, for the entire epithelium are given by

$$L_p = \frac{L_{MB}(H_M + H_B)}{H_M + H_B + RTC_0 L_{MB}\sigma_M^{\,2}}, \tag{3.17}$$

$$\sigma = \frac{H_B}{H_M + H_B}\sigma_M, \tag{3.18}$$

$$H = \frac{H_B}{H_M + H_B}H_M. \tag{3.19}$$

where L_{MB} is defined as,

$$L_{MB} = \frac{L_M L_B}{L_M + L_B}. \tag{3.20}$$

Here R is the gas constant, T is absolute temperature and C_0 is a reference osmolality. Following Weinstein (1984) we replace the mean membrane osmolality with this reference osmolality C_0 (290mOsm) to avoid nonlinearities and keep accuracy. H_M, σ_M and L_M are the NaCl permeability, the NaCl reflection coefficient and the water permeability of the composite barrier formed by the cells and TJ complex. H_B and L_B are the NaCl permeability and the water permeability of the basement membrane. As in Weinstein (1984), we have assumed that the reflection coefficient of the basement membrane is zero. In our model, we assume the basement membrane has a higher permeability to water and solutes than the composite barrier formed by the cells and the TJ complex.

From equations (3.18) and (3.19), H_M can be expressed in terms of σ_M,

$$H_M = \frac{\sigma_M}{\sigma}H. \tag{3.21}$$

Using equation (3.18), H_B can be written as

$$H_B = \frac{H_M}{(\frac{\sigma_M}{\sigma} - 1)}. \tag{3.22}$$

Equation (3.17) can be written so that L_{MB} appears explicitly.

$$\frac{1}{L_{MB}} = \frac{1}{L_p} - \frac{RTC_0\sigma_M^{\,2}}{H_M + H_B}. \tag{3.23}$$

If equation (3.20) is rewritten as

$$\frac{1}{L_M} = \frac{1}{L_{MB}} - \frac{1}{L_B}, \tag{3.24}$$

L_M can be determined if L_B is prescribed and L_{MB} is evaluated using equation (3.23). All the parameters appearing in equations (3.17), (3.18) and (3.19) for the composite barrier, except L_M, can be determined if σ_M can be evaluated and L_P, σ, and H are measured. However, it is argued in Weinstein (1984) that $L_B >> L_M$ and, thus, $L_M \sim L_{MB}$. Thus, we need to obtain only one additional independent relationship for σ_M.

Water reabsorption in the proximal tubule is driven by active transport and the osmotic pressure differences that are established by this active transport. Weinstein (1984) defines a measure of transport isotonicity which is given by

$$C^* = \frac{N}{H_M + RTC_0L_{MB}\sigma_M^{\,2}} + \frac{C_0L_{MB}\sigma_M(\pi_M - \pi_S)}{H_M + RTC_0L_{MB}\sigma_M^{\,2}}. \tag{3.25}$$

Here N is the active transport flux across the basolateral cell membrane due to the sodium-potassium pump, π_M is the mucosal (luminal) oncotic pressure and π_S is the serosal (peritubular) oncotic pressure. Equation (3.25) defines the luminal osmolality difference when the transported fluid has the same osmolality as the reference osmolality C_0. We will focus on the first term and, thus, require that transport be isotonic even in the absence of peritubular protein. The value of this term defines a constraint between L_P and σ_M because H_M, H_B and L_{MB} are all functions of σ_M and L_{MB} is related to L_P through equation (3.23). Thus, σ_M can be determined if we know the transepithelial values for H,

L_P and σ along with an estimate of C*. After σ_M is determined, H_M, H_B, L_{MB} can be evaluated using equations (3.21), (3.22) and (3.23) as described previously.

Once L_M, σ_M, and H_M are determined, one next evaluates their TJ components, L_{TJ} and σ_{TJ}. These predicted values of L_{TJ} and σ_{TJ} are then used to assess the detailed TJ structure. The properties of the composite barrier consisting of the cell barrier and the TJ barrier can be expressed in terms of their individual parameters. Let L_C and L_{TJ} denote the water permeabilities of the cell and the TJ complex, H_C and H_{TJ} be their NaCl permeabilities, and σ_C and σ_{TJ} be their NaCl reflection coefficients. Then

$$L_M = L_C + L_{TJ}, \tag{3.26}$$

$$\sigma_M = \frac{L_C\sigma_C + L_{TJ}\sigma_{TJ}}{L_C + L_{TJ}}, \tag{3.27}$$

$$H_M = H_C + H_{TJ} + RTC_0(\sigma_C - \sigma_{TJ})^2 \frac{L_C L_{TJ}}{L_C + L_{TJ}}. \tag{3.28}$$

The last term on the right-hand-side in equation (3.28) describes the solute-solvent interaction for a heteroporous parallel pathway with different reflection coefficients (Weinstein, 1987).

Equations (3.26), (3.27) and (3.28) can be manipulated to provide a constraint between L_{TJ} and σ_{TJ}. From equations (3.26) and (3.27), the fractional water permeability of the cell barrier, L_C/L_M, is related to σ_{TJ} by,

$$\frac{L_C}{L_M} = \frac{\sigma_M - \sigma_{TJ}}{\sigma_C - \sigma_{TJ}}. \tag{3.29}$$

The fractional water permeability of the TJ is,

$$\frac{L_{TJ}}{L_M} = 1 - \frac{L_C}{L_M} = \frac{\sigma_C - \sigma_M}{\sigma_C - \sigma_{TJ}}. \tag{3.30}$$

From (3.30) L_{TJ}/L_M can not be less than σ_C-σ_M. Equation (3.28) can be rewritten using (3.26), (3.29) and (3.30) as

$$H_M - H_C - H_{TJ} = RTC_0(\sigma_C - \sigma_{TJ})^2 \frac{L_C}{L_M}\frac{L_{TJ}}{L_M}L_M$$

$$= RTC_0(\sigma_C - \sigma_M)(\sigma_M - \sigma_{TJ})L_M \qquad (3.31)$$

$$= RTC_0(\sigma_M - \sigma_{TJ})(\sigma_C - \sigma_{TJ})L_{TJ}\,. \qquad (3.32)$$

Equation (3.32) provides the required constraint between σ_{TJ} and L_{TJ}. This assumes that all three permeabilities on the left-hand-side of equation (3.32) are known, σ_C=1 and σ_M has been related to L_P using equation (3.25). H_M has been already determined by the compartment model in terms of H and σ_M, equation (3.21). H_C is very small (Weinstein, 1984).

H_{TJ} is independently estimated from the expression for the transepithelial electrical resistance.

$$\Omega = \frac{1}{H}\frac{RT}{\bar{C}(zF)^2} \cong \frac{1}{H_{TJ}}\frac{RT}{\bar{C}(zF)^2}\,. \qquad (3.33)$$

Here Ω is the transepithelial electrical resistance, z is the valence for NaCl (z=1), F is Faraday's constant and $\bar{C}$ is the mean ion concentration (the same reference osmolality C_0 as in equation (3.17) is used). Since the basement membrane and the composite barrier are in series in the compartment model and the conductance of the basement membrane is much larger than that of the composite barrier, the transepithelial electrical resistance is approximated by the resistance of the tight junction. The NaCl permeability H varies from 13.7 to 19.1 $\times$ 10^{-5} cm/s (the corresponding transepithelial resistance varies from 5-

7 ohm·cm^2). In this model we have selected a value for H_{TJ} which is at the lower limit for H, 13×10^{-5} cm/s.

There are two unknowns, σ_{TJ} and L_{TJ}, in equation (3.32). A simple way to solve for σ_{TJ} and L_{TJ} is to replace L_M by L_{MB} in equation (3.31), since $L_B >> L_M$ in equation (3.24). Equation (3.31) can then be approximated by

$$H_M - H_C - H_{TJ} \cong RTC_0(\sigma_C - \sigma_M)(\sigma_M - \sigma_{TJ})L_{MB}. \tag{3.34}$$

From (3.34) σ_{TJ} can be expressed explicitly as

$$\sigma_{TJ} \cong \sigma_M - \frac{H_M - H_C - H_{TJ}}{RTC_0(\sigma_C - \sigma_M)L_{MB}}. \tag{3.35}$$

Once σ_{TJ} is determined, L_{TJ} can be calculated from equation (3.32).

$$L_{TJ} = \frac{H_M - H_C - H_{TJ}}{RTC_0(\sigma_M - \sigma_{TJ})(\sigma_C - \sigma_{TJ})}. \tag{3.36}$$

§ 3.3.2 Dual pathway model for the tight junction strands

As discussed above, we propose that the TJ strands contain numerous small circular pores and infrequent large slit breaks, the former associated with junction particle pairs and the latter associated with junction strand discontinuities, as sketched in Fig. 3.4. The model predictions for the sizes of the pores and the slits strongly suggest this structure. A heteroporous model which includes solute-solvent interaction must be used because the reflection coefficients and the water permeabilities differ greatly for each pathway. Let 1 and 2 denote the two pathways, 1 for large slit breaks and 2 for small

circular pores. Based on the theory in Weinstein (1987), the composite values for the TJ, L_{TJ}, H_{TJ} and σ_{TJ}, are

$$L_{TJ} = L_1 + L_2, \tag{3.37}$$

$$\sigma_{TJ} = \frac{L_1\sigma_1 + L_2\sigma_2}{L_{TJ}}, \tag{3.38}$$

$$H_{TJ} = H_1 + H_2 + RTC_0(\sigma_1 - \sigma_2)^2 \frac{L_1 L_2}{L_1 + L_2}. \tag{3.39}$$

Here C_0 is a reference osmolality for each solute. Equation (3.39) is applied separately for NaCl, mannitol and sucrose. The last term in equation (3.39) again represents the solute-solvent interaction as in equation (3.28). For NaCl, the reference osmolality is 290 mOsm used in equation (3.17). A rough calculation indicates that the value for the interaction term for NaCl does contribute to H_{TJ} and will be retained in the calculation for NaCl. In contrast, for mannitol and sucrose, this term is small by virtue of small C_0 for these solutes. Thus, for mannitol and sucrose, the interaction term in equation (3.39) is dropped in the calculation. The magnitude of this neglected term can be estimated after the TJ ultrastructure is determined.

The water permeability and solute permeability due to the infrequent large slit breaks in the TJ strands can be expressed by

$$L_1 = \frac{A_1 \times W_1^2}{12\mu\delta_1}, \tag{3.40}$$

$$H_1 = \frac{A_1 \times D_{slit}}{\delta_1}. \tag{3.41}$$

Here δ_1 is the effective depth of the large slit breaks, A_1 is the total area of open slits per unit surface area and W_1 is the slit height. Equation (3.40) like equation (3.5) is based on infinite slit theory. D_{slit}, the solute diffusion coefficient in the large slit breaks, is given by equation (3.7).

The water permeability and solute permeability due to the small circular pores in the TJ strands can be expressed by

$$L_2 = \frac{A_2 \times R_2^{\,2}}{8\mu\delta_2}, \tag{3.42}$$

$$H_2 = \frac{A_2 \times D_{pore}}{\delta_2}. \tag{3.43}$$

Here δ_2 is the effective depth of the small circular pores, A_2 is the total area of open pores per unit surface area and R_2 is the pore radius. D_{pore}, the solute diffusion coefficient in the circular pores, is given by equation (3.3).

The expressions for the reflection coefficients for large slit break and small circular pore pathways differ. For both cases the reflection coefficient is defined in terms of the partition coefficient ϕ (Michel and Curry, 1999).

$$\sigma = (1-\phi)^2. \tag{3.44}$$

For large slit breaks (Michel and Curry, 1999)

$$\phi = \left(1 - \frac{2a}{W_1}\right). \qquad (a < W_1/2) \tag{3.45a}$$

For small circular pores (Michel and Curry, 1999)

$$\phi = \left(1 - \frac{a}{R_2}\right)^2. \tag{3.45b}$$

Four unknowns describe the geometry of the large slit break and small circular pore pathways, W_1, A_1/δ_1, R_2, and A_2/δ_2. Four constraints are needed to determine this dual pore/slit geometry. These four constraints are the TJ water permeability L_{TJ}, the TJ reflection coefficient σ_{TJ}, and the TJ NaCl and sucrose permeabilities. We relax the constraint of the TJ mannitol permeability. For sucrose we use the measured permeability values in Preisig and Berry (1985). The TJ NaCl permeability is determined from the transepithelial electrical resistance in equation (3.33) as described earlier. The estimated value for the TJ NaCl permeability, 13×10^{-5} cm/s, in Weinstein (1984) is used. There are no measured values for L_{TJ} and σ_{TJ}. However, an estimate of σ_{TJ} and L_{TJ} can be provided from the analysis of the compartment model, equation (3.35) and (3.36), as described in the previous section. After the dimensions of both large slit breaks and small circular pores are determined, the TJ mannitol permeability will be evaluated and compared with its measured value.

To further explore the dual pathway model, the fraction of the total TJ length occupied by the large slit breaks and the average spacing of small circular pores in rat proximal tubule are examined. The fraction of the total TJ length occupied by the large slit breaks in rat proximal tubule, f_1, can be expressed as

$$f_1 = \frac{SA_1}{W_1 l_{TJ}}. \tag{3.46}$$

Here l_{TJ} is the total TJ length in the selected segment of the rat proximal tubule and S the total surface area excluding the brush border of the same segment of proximal tubule. SA_1 is the total area of the large slit breaks in the same segment and $\frac{SA_1}{W_1}$ is the total

length of large slit breaks in the same segment. To calculate f_1 one must specify the slit depth δ_1 to find A_1 after A_1/δ_1 is determined.

The average spacing of the small circular pores in the rat proximal tubule, λ_2, can be expressed as

$$\lambda_2 = \frac{l_{TJ}}{\frac{SA_2}{\pi R_2^2}}. \qquad (3.47)$$

Here SA_2 is the total area of small pores in the selected segment of the rat proximal tubule and $\frac{SA_2}{\pi R_2^2}$ is the number of small pores in the same segment. Equation (3.47) provides an estimate of the average distance between pores in the TJ strand. Again we assume the pore depth δ_2 is specified after A_2/δ_2 is determined.

§ 3.4 Parameters Values

The parameter values used in the compartment model are summarized in Table 3.2A. The reference osmolality C_0= 290mOsm. T=310.15^{0}K. C*=5.94 mOsm. The active transport flux N=18.5 nmol/s/cm^2 epithelium. The sodium permeability of the cell barrier H_C is very small and the value used in Weinstein (1984), 3.1×10^{-10} cm/s, is adopted. The reflection coefficient of the basement membrane σ_B is zero. The transepithelial water permeability of proximal tubule L_P has been measured in several species using different techniques (Ullrich, 1973; Preisig and Berry, 1985; Green and Giebisch, 1989). Early measurements and methods before 1983 are summarized in Berry (1983). These and more recent experiments reveal a significant variation in L_P for rat proximal tubule. Berry (1983) reported values that varied from 0.2-0.3 cm/s ($1.87\text{-}2.80\times10^{-7}$ cm/s/mmHg). The

measured L_P by Preisig and Berry (1985) is 0.12-0.15 cm/s ($1.12\text{-}1.40\times10^{-7}$ cm/s/mmHg), depending on whether the NaCl reflection coefficient is assumed to be 1.0 or 0.7. The microperfusion measurements in Green and Giebisch (1989) provided a value for L_P of 0.10cm/s (0.94×10^{-7} cm/s/mmHg).

The measured values for σ vary from 0.59 (Green and Giebisch, 1989) to 0.7 (Ullrich, 1973). In Van der Goot et al. (1989) the NaCl and KCl reflection coefficients are measured and found to be close to unity for both plasma and intracellular membranes vesicles. In our model the cell membrane reflection coefficient $\sigma_C = 1$ and the transepithelial reflection coefficient for NaCl $\sigma = 0.68$. This transepithelial reflection coefficient for NaCl is the same as the value used in Weinstein (1984).

The measured mean values for NaCl permeability of rat proximal tubule vary between 13.3×10^{-5} cm/s (Green and Giebisch, 1989) and 24.7×10^{-5} cm/s (Ullrich, 1973). The value for the transepithelial NaCl permeability in this model is the same as the value in Weinstein (1984), $H=22.0\times10^{-5}$ cm/s. In this study we assume that the electrodiffusive NaCl flux passes nearly exclusively through the TJ and that the barrier associated with H_B offers little resistance. Thus, H_{TJ} is estimated from equation (3.33). The selected value, 13×10^{-5} cm/s, is the same as that used in Weinstein (1984). The corresponding transepithelial electrical resistance is 7.35 Ωcm^2.

The parameters for the dual pathway model are summarized in Table 3.2B. The viscosity $\mu=0.0007$Pa·S. In this calculation the Stokes-Einstein radii for NaCl, mannitol and sucrose are 1.47Å, 3.6Å and 4.6Å, respectively. Their corresponding free diffusion coefficients are 2.21×10^{-5} cm^2/s, 0.90×10^{-5} cm^2/s and 0.70×10^{-5} cm^2/s. The non-electrolyte permeability of the TJ is at least one order of magnitude smaller than the small

ion permeability. The measured permeability values for mannitol and sucrose in rat proximal tubule are 0.87×10^{-5} cm/s and 0.43×10^{-5} cm/s (Preisig and Berry, 1985). These values are adopted in our calculation.

The measured luminal epithelial surface excluding microvilli and the TJ length in S2 segment of rat proximal tubule are 96×10^{3} μm^2/mmtubule and 68.8 mm/mmtubule (Maunsbach and Christensen, 1992). We shall see that these data suggest a very torturous cell boundary. The effective depth (apical-to-basal direction) of large slit breaks is 100 nm. This is typically the spacing between the strands in the depth direction of the cleft. In proximal tubule, there is usually a two strand structure that is divided into small compartments by cross-bridging segments between the longitudinal strands. The "slit break" occurs when the breaks in each of the TJ strands coincide, providing a pathway through the TJ from lumen to lateral space.

In this study, the effective small circular pore depth is 10 nm. We assume that the space between the lateral membranes of neighboring cells will offer little resistance compared to the small pores in the TJ. This 10 nm pore depth assumes that there are 5 nm long circular pores in each strand of the two strand structure in the TJ complex.

§ 3.5 Results

We first examine the model data used by Weinstein (1984). When L_p is 2.4×10^{-7} cm/s/mmHg, σ_M from equation (3.25) has the value 0.84 for $H=22\times10^{-5}$ cm/s, $\sigma = 0.68$ and C*=5.94 mOsm. In this case, our model predicts that $\sigma_{TJ}=0.620$ and $L_{TJ}=3.02\times10^{-7}$ cm/s/mmHg. Both values are slightly smaller than the values in Weinstein (1984). In our model, L_M was replaced by L_{MB}. Since L_{MB} is always less than L_M, a smaller σ_{TJ} is

needed to balance both sides of equation (3.34). A smaller σ_{TJ} results in a smaller L_{TJ}, see equation (3.36) and Table 3.2A and 3.3A.

We next consider the results for the compartment model with a reduced transepithelial water permeability. When $L_p=1.59\times10^{-7}$ cm/s/mmHg, σ_M from equation (3.25) has the value 0.94 for $H=22\times10^{-5}$cm/s, $\sigma=0.68$ and C*=5.94 mOsm. The NaCl permeability of the composite barrier, H_M, is 30.5×10^{-5} cm/s and the water permeability, L_{MB}, is 5.66×10^{-7} cm/s/mmHg. The value of H_B from this calculation is 79.3×10^{-5}cm/s, or six times greater than H_{TJ}, close to the value used previously. There is some security to this value, in the sense that H_B is the key parameter to determine the osmotic gradient against which the proximal tubule can transport water. Model predictions of the magnitude of this gradient have been found to be coherent with experimental determination (Green et al., 1991). After replacing L_M with L_{MB}, $\sigma_{TJ}=0.0079$ and $L_{TJ}=0.34\times10^{-7}$ cm/s/mmHg, see Table 3.2A and 3.3A.

Equation (3.25) introduces uncertainty in the model since C* is not known precisely. In Fig. 3.5 we have plotted the relation between σ_M, L_P and C* for three values of C*. Increasing L_P results in a decreasing σ_M when C* is kept constant, while increasing C* results in a nearly uniform downward shift of σ_M for all L_P. Improper combinations of L_P and C* will result in a value of σ_M which exceeds unity and is physically impossible. When L_P is 2.4×10^{-7} cm/s/mmHg and C*=5.94mOsm, $\sigma_M=0.84$, the value used in Weinstein (1984) is recovered.

σ_{TJ} can be estimated from equation (3.35) if one replaces L_M with L_{MB} in equation (3.31). In Fig. 3.5 we plot the relation between σ_M, L_P and σ_{TJ} for two values of

σ_{TJ}, 0.0 and 0.05. σ_{TJ} <<1 because this is required for any pore or slit that admits a substantial water flow. As shown in Fig. 3.5, a compatible value for L_P to satisfy both C*=5.94 mOsm and $0<\sigma_{TJ}<0.05$ is approximately 1.6×10^{-7} cm/s/mmHg. A sensitivity analysis, which will be described later in this section, has been performed to show how the dual pore-slit geometry varies as a function of C* and σ_{TJ}. For each value of C* there is a family of solutions in a narrow range of σ_{TJ} near zero which enable one to satisfy the TJ water permeability and reflection coefficient predicted by the compartment model and the TJ permeability for NaCl and sucrose. We shall also show that the dual pore-slit geometry is insensitive to C* for a specified value of σ_{TJ}. When C* =5.94mOsm one finds that this family of solutions will also independently satisfy the measured permeability for mannitol if σ_{TJ}=0.0079 and $L_{TJ}=0.336\times10^{-7}$ cm/s/mmHg. This solution is defined as a best-fit and the results for this case are summarized in Table 3.3A.

These theoretically estimated values for σ_{TJ} and L_{TJ} and the TJ solute permeabilities for NaCl and sucrose are used to predict the four unknowns describing the geometry of the dual pathway model. The predicted results are listed in Table 3.3B. The predicted gap height of the large slit breaks is 19.6nm. A_1/δ_1 for these breaks is 0.525 cm^{-1}. The predicted small pore radius is 0.668 nm and the pore area per unit surface area over the pore depth, A_2/δ_2, is 15.8 cm^{-1}. σ_1 for the large slit breaks is very close to zero, 2.26×10^{-4}, while σ_2 for the small circular pores is 0.153. The predicted TJ mannitol permeability is 0.89×10^{-7}cm/s. Thus, this pore/slit geometry provides excellent agreement for the measured permeability of mannitol.

The reported values for the rat proximal tubule area and the total TJ length (Maunsbach and Christensen, 1982) are used to provide the estimation of the fraction of

the total TJ length occupied by the large slit breaks and the average spacing of the small circular pores. We first assume that the effective depth of the large slit pathway is 100nm. This value for δ_l assumes that the gap height of the pathway through the strands is nearly uniform as observed in endothelial junctions (Adamson and Michel, 1993). However, since the average length of the breaks observed in individual strands is typically 100nm, coincident breaks in a dual strand structure are rare (see discussion). Then, if the surface area per millimeter tubule is $S=96 \times 10^3$ μm^2/mmtubule and $l_{TJ}=68.8$ mm/mmtubule, $f_l=3.75\times10^{-4}$. This implies that only 0.0375 percent of l_{TJ} is occupied by aligned large slit breaks. For small circular pores, if we assume the pore depth is 10nm, then $f_2=20.2$ nm. This implies that on average there is a small pore every 20.2 nm.

An important prediction of the dual pathway model is that 95.0 percent of TJ water permeability, L_{TJ}, is accommodated by the infrequent large slit breaks while only 5.0 percent is accounted for by the far more numerous small circular pores. In contrast to L_{TJ}, nearly 91.2 percent of H_{TJ} for NaCl is accounted for by these numerous small circular pores. Only 8.65 percent of H_{TJ} is accounted for by the large slit breaks. The solute-solvent coupling term in equation (3.39) accounts for the remaining 0.16 percent. The model predicts that only 21.7 percent of the sucrose transport is through the small circular pores and 78.3 percent through the large slit breaks. The contribution of the large slit breaks to the predicted TJ permeability for mannitol is 49.2 percent. The model, thus, predicts that nearly one half of the mannitol transport is through the large slit breaks.

Fig. 3.5 provides the essential link between the compartment and the dual pore/slit models. In the compartment model, one has the freedom to choose large values of σ_{TJ},

such as 0.65 in Weinstein (1984). These larger values are not compatible with the dual pathway model because most of the water passes through the large slit breaks and the reflection coefficient for this pathway is close to zero. Thus, even if the reflection coefficient for small pores is close to unity, σ_{TJ} in equation (3.38) would still be small because little water passes through the small pore pathway. We shall show that the largest realizable σ_{TJ} is limited to roughly 0.03.

Four unknowns are required to define the dual pathway in the TJ strands, W_1, A_1/δ_1, R_2 and A_2/δ_2. However, the measured values for the TJ salt, sucrose and mannitol permeability and the compartment model predictions for σ_{TJ} and L_{TJ}, provide five constraints for predicting the dimensions of the dual pathway geometry. We, therefore, need to relax one of the constraints. The logical choice is to relax either the mannitol or sucrose permeability since the radii of both these solutes are close in size and, thus, do not provide strong independent constraints, as already emphasized in the single pathway model. We, thus, chose the TJ water, salt and sucrose permeability values, but relaxed the constraint on mannitol permeability. This choice has the advantage that it satisfies the constraints on σ_{TJ} and L_{TJ} required by both the compartment and pore/slit models and thus unifies the two approaches.

In Table 3.4 we have listed the predicted dimensions of the dual pathway for several different combinations of L_P and C*. In Table 3.4A, we vary C* from 4 mOsm to 8 mOsm while maintaining σ_{TJ} nearly constant. Although L_P varies significantly with C*, there are only minor changes in L_{TJ} from 0.33 to 0.34 $\times 10^{-7}$ cm/s/mmHg. This can be explained using equation (3.36). Because $\sigma_{TJ} << 1$ and σ_M varies from 0.92 to 0.96, equation (3.36) can be approximately rewritten using equation (3.21) as

$$RTC_0 L_{TJ} \cong \frac{H_M - H_{TJ}}{\sigma_M} = \frac{H}{\sigma} - \frac{H_{TJ}}{\sigma_M}. \tag{3.48}$$

where H_C is very small and has been neglected. Since σ_M changes little, L_{TJ} undergoes minor changes. Thus, the dual pathway geometry is insensitive to C* if both L_{TJ} and σ_{TJ} are nearly constant. We then conclude that keeping σ_{TJ} constant and varying C* does not significantly alter pore/slit geometry although L_P changes significantly. L_P is determined primarily by the transcellular pathway and the changes in C* are associated with the water permeability of the cell membranes. $L_{TJ} << L_M$ and most of water enters through the transcellular pathway.

In Table 3.4B, we predict the dimensions of the dual pathway by keeping C*=5.94 mOsm and letting σ_{TJ} increase from 0.00666 to 0.0304. Equation (3.48) predicts that the changes in L_{TJ} are very small and the changes in L_P even smaller since L_C is maintained constant and $L_{TJ} << L_C$. When $\sigma_{TJ}=0.0304$ and $L_{TJ}=0.352\times10^{-7}$ cm/s/mmHg, the pore spacing λ_2 is only 0.17 nm larger than the pore diameter 0.63 nm. When $\sigma_{TJ}=0.00666$ and $L_{TJ}=0.3350\times10^{-7}$ cm/s/mmHg, the small pore spacing is 40.2 nm and the large slit gap height is 29.5 nm. Thus, the upper bound of the physiological range for σ_{TJ} is slightly larger than 0.03; otherwise the small pores would form a continuous narrow slit which is not compatible with recent views of the claudin-occludin structure of the TJ strand (Fanning et al., 1999; Furuse et al., 1999). The realizable lower bound is 0.006, otherwise the large slit height will be greater than 30 nm, the value significantly greater than the typical 20nm gap height observed for the large slit breaks in endothelial TJs (Adamson and Michel, 1993). These results for small pore spacing and large slit height are plotted in Fig. 3.6.

Since the physically realizable range of σ_{TJ} is from 0.0067 to 0.03, one expects that small changes in σ_{TJ} can produce large changes in pore/slit geometry. In fact, one expects there to be an important transition in behavior as the permeability to NaCl of the small pore increases. Since $\sigma_2 >> \sigma_1$, σ_{TJ} will be dominated by the second term in equation (3.38) when the small pore is small enough for σ_2 to significantly exceed zero. Although σ_2 will decrease as the small pore increases in size, the first term for large slit breaks will always be less than 3% of the second term. The large increase in gap height as σ_{TJ} approaches 0.006 is due to the increase in salt permeability through the small pore pathway from 86.6% to 96.1% as the small pore radius increases. From Table 3.4B, the salt permeability through the large slit pathway decreases at the same time from 11.1% to 3.8% due to the three fold decrease in slit area (A_1/δ_1) while there is only a small change in water permeability through the same pathway. The large increase in gap height as σ_{TJ} approaches 0.006 is needed to maintain the nearly constant value of L_{TJ} required by the compartment model.

Varying σ_{TJ} along constant C* curve and varying C* along a constant σ_{TJ} curve in Fig. 3.5 have very different effects. The former produces large changes in small pore radius and spacing, modest changes in large slit height and area, minor changes in L_{TJ} and negligible changes in L_P. In contrast, varying C* while holding σ_{TJ} and L_{TJ} nearly constant has little effect on pore/slit geometry but a substantial effect on transcellular permeability L_P.

The foregoing sensitivity analysis is summarized in Fig. 3.6 where we have plotted the predicted results for large slit breaks (Panel A), small circular pores (Panel B)

and the evaluated mannitol permeability (Panel C) from the dual pathway model. In Panel A, we plot the large slit height and spacing versus σ_{TJ}. The large slit spacing is defined as the average length of TJ strand between two large slit breaks if their average length was 200nm. If f_l is the fraction of the total length occupied by the large slit breaks, T is the average length of a large slit break, the large slit break spacing Δ is given by

$$\Delta = \frac{T}{f_l}. \tag{3.49}$$

One observes that the large slit height and spacing are nearly constant when $\sigma_{TJ} >$ 0.015. When $\sigma_{TJ}>0.015$, the small pore radius is less than the sucrose radius. Thus, 100 percent of sucrose permeability is associated with the large slit break pathway. Because the sucrose radius is much less than the large slit height, the transport area available for sucrose transport is nearly constant, see equation (3.6). The water permeability through the large slit pathway changes little, thus, the large slit height and spacing are nearly constant.

In contrast, the small pore radius and the small pore spacing continue to decrease when σ_{TJ} increases from 0.015 to 0.03. In equation (3.27), σ_{TJ} is mainly determined by the second term (small pore pathway) and the contribution of the first term (large slit breaks) can be neglected. One can increase σ_{TJ} by either increasing the reflection coefficient σ_2 of the small pore pathway, or increasing the water permeability L_2 of the small pore pathway or both. However, the small pore pathway has little capacity to allow for a large water permeability, as shown in Preisig and Berry. We also show in Table 3.4B that the fractional TJ water permeability through the small pore pathway never exceeds 6.6 percent of the TJ water permeability. Thus, the more likely way for σ_{TJ} to

increase is to increase σ_2 by decreasing the pore radius. However, this also greatly increases the steric exclusion and the hydrodynamic resistance for salt transport, see equation (3.3). One has to increase the total pore area to maintain the measured TJ salt permeability. Thus, the small pores will decrease in size but be more frequent, and their spacing will greatly decrease. When $\sigma_{TJ}>0.03$, the small pores nearly overlap and form a continuous slit in contradiction to the observed ultrastructure of the TJ strands. From the standpoint of steric exclusion, σ_{TJ} could approach L_2/L_{TJ}, but as noted above, the realistic upper limit is approximately 0.03.

The evaluated mannitol permeability in Panel C is nearly constant and less than the experimental measurements when σ_{TJ} varies from 0.015 to 0.03. In this range of σ_{TJ}, the predicted small pore radius is close to the mannitol radius, and the steric exclusion and the hydrodynamic resistance greatly limit the mannitol permeability through the small pore pathway. Most of the TJ mannitol permeability is due to the large slit breaks. Since the large slit height and spacing change little in this range of σ_{TJ}, the mannitol permeability does not change significantly. At the lower limit σ_{TJ} can not be <0.006. In this limit, the small pore radius increases rapidly and allows for a large increase in sucrose and mannitol permeability that exceeds the experimental measurements in Preisig and Berry. Again, we find that the realizable range of σ_{TJ} is from 0.006 to 0.03. If we use the measured mannitol permeability as an independent constraint on σ_{TJ}, one finds that the measured value, 0.87×10^{-5} cm/s in Preisig and Berry, can be achieved with high precision when $\sigma_{TJ}=0.0079$. At this value of σ_{TJ}, the large slit spacing is 533μm and the small pore spacing is 20.2nm. This is the best-fit solution whose results were discussed earlier in Table 3.3A.

§ 3.6 Discussion

In this chapter we have proposed a new ultrastructural model for the TJ strands in rat proximal tubule epithelium which attempts to satisfy the measured permeabilities for water, NaCl and nonelectrolytes. To achieve this, we have developed a dual pathway model which combines infrequent large slit breaks and numerous small circular pores in the TJ strand. The TJ water permeability and reflection coefficient are used together with the TJ NaCl and sucrose permeability to provide insight into the structure and function of the TJ complex. While dual pathway models have been proposed in the past, nearly all of these models have been based on heterogeneous circular pore theory, which is not an adequate description of the large slit breaks observed in the TJ strands. The present model is intended to provide a more realistic description of the actual TJ strand ultrastructure which includes our latest understanding of its molecular composition.

Single pore/slit models

The single pore/slit pathway model in Preisig and Berry (1985) was developed to satisfy only the measured permeabilities of mannitol and sucrose. The radii of mannitol and sucrose differed by only 1 Å and this limited an accurate determination of the pore radius or slit height in the TJ strands. The model further assumed that all the mannitol and sucrose molecules traverse the TJ via the same pore/slit ultrastructure. Our model allows that this may not be the case. In our proposed dual pathway model, the small pores account for nearly one half of the mannitol flux, but, 78.3 percent of the sucrose follows a second pathway, namely, large slit breaks in the TJ strand. The single pore/slit theory is unable to accommodate any substantial water permeability.

We also examined the capacity of single pore/slit theory to satisfy TJ NaCl permeability and either mannitol or sucrose permeability, since these solutes differ significantly in size. This approach leads to the prediction that the pore radius/slit height is smaller than predicted in Preisig and Berry, but the available transport area is three times larger (Table 3.1). Thus, the predicted water permeability of the TJ is a little larger than the predicted water permeability of the paracellular pathway in Preisig and Berry. However, this predicted TJ water permeability is still less than 3 percent of the entire transepithelial water permeability.

In addition, we tried to jointly satisfy the TJ water and NaCl permeability using a single pore/slit model while relaxing the constraints on mannitol and sucrose permeabilities. This approach leads to significantly larger pores/slits in the TJ strand. However, it predicted a mannitol and sucrose permeability which was approximately five times larger than the measured values. In summary, we confirm that a single pore/slit model can not simultaneously satisfy the measured values for the transepithelial water permeability, the transepithelial NaCl reflection coefficient, and the paracellular mannitol and sucrose permeabilities. The greater flexibility of a dual pathway model is needed to reconcile these discrepancies.

Relationship of dual pathway model for TJ ultrastructure to compartment model of proximal tubule

The effort to determine the dimensions of the dual pathway pore-slit structure using the TJ water, NaCl, and sucrose permeabilities and the TJ reflection coefficient is limited by the fact that there are no measured values for the TJ water permeability, $L_{TJ,}$

and the TJ reflection coefficient, σ_{TJ}. However, estimated values for TJ parameters are available from a compartment model of rat proximal tubule epithelium (Weinstein, 1984). In the dual pathway model the small circular pore and the large slit break pathways are in parallel. The water permeability of the circular pores (5.0 percent) is small and the solute reflection coefficient of these small pores is close to 0.153 for NaCl. In contrast, the reflection coefficient for the large slit breaks will approach zero while its contribution to L_{TJ} will be large (95.0 percent). Thus, the composite reflection coefficient of the TJ, σ_{TJ}, will be much less than unity (0.0079). This prediction from the dual pathway model is a contradiction to the estimated value for the TJ reflection coefficient in Weinstein (1984), σ_{TJ}=0.65. We had to find a new set of parameter values to be used in the dual pathway model, but which would be consistent with the compartment model. The compartment model remains necessary to provide a relationship between the transepithelial reflection coefficient for NaCl, σ=0.68, and the reflection coefficient for the TJ.

The measured transepithelial water permeability, L_P, NaCl permeability, H, and the transepithelial NaCl reflection coefficient, σ, along with the constraint of isotonic transport C*, are first used to predict the composite luminal membrane NaCl permeability, H_M, NaCl reflection coefficient, σ_M, and water permeability, L_M. This model can also provide a constraint between L_{TJ} and σ_{TJ}, equation (3.32). σ_{TJ} is first determined using equation (3.35) by assuming $L_M \approx L_{MB}$. L_{TJ} is then determined using the constraint, equation (3.32). The predicted value for L_{TJ} is 21.2 percent of the transepithelial water permeability. This estimate of σ_{TJ} and L_{TJ} is then applied in the dual

pathway model of the TJ to determine the dimensions of the pores and slits in the TJ strand.

With respect to the model prediction of the magnitude of tight junctional water flux, one may note the observations of Schnermann et al. (1998), who found that mice, genetically defective for the proximal tubule cell membrane water channel, aquaporin-1, had a reduction in proximal tubule epithelial water permeability of nearly 80% compared with control mice. That finding has been used by some to conclude that 20% is an upper limit on TJ water flow in proximal tubule. Although this is compatible with the present work (but not with Weinstein, 1984), it must be acknowledged that there are no measurements of solute reflection coefficients in any strain of mouse, so constraints on the size and locus of the water pathways are unknown.

Large slit breaks

Our combined dual slit/pore model predicts that there will be infrequent large slit breaks in the TJ strands. These large slit discontinuities in the TJ strands are responsible for the large increase in the TJ water permeability above that predicted in Preisig and Berry (1985). The predicted length of the large slit breaks is only a small fraction ($\sim 3.75 \times 10^{-4}$) of the entire length of the TJ strands in the rat proximal tubule, but they account for 95.0 percent of the TJ water permeability, 78.3 percent of the TJ sucrose permeability and nearly half of the TJ mannitol permeability. However, these large slit breaks account for only 8.7 percent of the TJ NaCl permeability. Thus, they form a secondary route for the passage of small solutes.

The total TJ length has been reported in Maunsbach and Christensen (1992), 68.8 mm/mmtubule. There are approximately 300 cells in an S2 segment of 1mm length in rat proximal tubule. Thus, the average length of the TJ surrounding one cell is 2×68.8mm/300=459 μm where the factor of two reflects the sharing of the TJ between neighboring cells. Since the predicted fractional length of a large slit pathway is 3.75×10^{-4}, then the length of a large slit in one cell is $459\mu m \times 3.75 \times 10^{-4} = 172$ nm. If a typical large slit break in an individual TJ strand of a two strand junctional complex is 200 nm in length, as observed in Orci et al. (1981), then, our model predicts that one such slit can be found on average in 200/172 or every 1.2 cells.

The above estimate of the open fractional length is based on an examination of the TJ complex and its compartment structure as observed in Figs. 13 and 17 in Orci et al. (1981). One notes that the TJ in rat proximal tubule is typically a two-strand structure with polygonal compartments that are roughly 100 nm on a side with traverse segments interspersed between the basic longitudinal strands. Occasionally, more than one transverse compartment can separate the two longitudinal strands. Large slit breaks that allow for water passage are created when a break in one strand happens to be aligned with a break in the second strand. Only when this occurs is there an open water pathway across the two-strand complex. This is a rare event due to the interspersed compartmental structure. If this compartmental organization were absent water could enter at a break at any location in the first strand, travel in the channel between strands, and eventually leave through a distant break in the second strand. However, with compartments that are roughly of the same length as the breaks, the probability of finding a through pathway is the product of finding overlapping breaks in each strand. Thus, if the probability of

finding a 100nm break in the first strand is 0.01, the likelihood of finding two overlapping breaks in two strands in series is 10^{-4}. Since the predicted probability of finding an open pathway through a dual strand structure is 3.75×10^{-4}, the likelihood of finding a break in each strand is 1.94 percent.

Multiple TJ strands can be found in both epithelium and endothelium. However, in most continuous capillaries, endothelial TJs do not form small polygonal compartments. The tight junction ultrastructure in capillary endothelium has been best quantified in frog mesentery capillary where there are, on average, 1.4 strands per cross section, but only one nearly continuous strand (Adamson and Michel, 1993). The average length of the large slit breaks in frog mesentery capillary is 150 nm. This is of the same order as the 200nm TJ discontinuities observed in proximal tubule (Orci et al., 1981). The slit height in frog mesentery capillary, 20 nm, is very close to the predicted gap height, 19.6 nm, in the present model. The frequency of the large slit breaks in frog mesentery, one open slit of 150 nm length in 4320 nm (Hu et al., 1999), or a probability 150/4320=0.035, is about two fold greater than the result predicted herein, 0.0194 for finding a 172 nm break in either strand of a two strand complex.

The important insight that the TJ strands of rat proximal tubule might have discontinuities was deduced from the paper of Adamson and Michel (1993) in which it was demonstrated by both serial sectioning and the tracer wakes of lanthinum that penetrated the TJ of frog mesentery that discontinuities of significant length could exist in the particle strands comprising the TJ. This conclusion cannot be definitively deduced from the particle patterns observed in freeze fracture since one does not have double replicas in which particle gaps in the E-face can be matched in a mirror image with a gap

in the P-face. Since the water permeability coefficient of frog mesentery and rat proximal tubule are of the same order this provides a clue that such breaks might also be present in the proximal tubule, although the comparable ultrastructural studies have not yet been performed. Finally, the large slit breaks should be viewed as dynamic rather than static structures, since the TJ strands may break and reform, either in response to regulatory signals or to pharmacological agents. Adamson et al. (1998) has observed that both the average number of TJ strands and the water permeability can be modulated by cAMP in frog mesentery capillaries, but the situation in epithelia is less certain

Small circular pores

In addition to the infrequent large slit breaks in the TJ strand, our model also predicts that there are numerous small circular pores in the TJ strands. These numerous small circular pores are the primary pathways for small solutes. Our model predicts that 91.2 percent NaCl flux across the TJ is accommodated via this pathway. Half of the mannitol transport can traverse via this pathway, whereas nearly one fifth of the sucrose flux goes by this route. Our model also suggests that there is one circular pore every 20.2 nm in the TJ strands. It must be acknowledged that the calculations of this paper utilize an equivalent non-electrolyte reflection coefficient for NaCl, despite the fact that the fluxes are ionic in nature, and could be influenced by the pore charge. More specifically, one may ask whether the pore size determined using this equivalent nonelectrolyte reflection coefficient is meaningful, given the possible charge effects. The larger issue of relating overall salt coefficients to the component ionic coefficients has been addressed (Kedem and Leaf, 1966). However, the reliability of the equivalent pore radius obtained

from the neutral salt has never been investigated. Despite this uncertainty, the calculations of this paper suggest that the equivalent small pore is actually smaller than that estimated by Preisig and Berry, and thus it remains a poor candidate for the water pathway. The structural correlates for the small pores are sketched in Fig. 3.4. On average, there is roughly one circular pore associated with each particle pair in the TJ strand, assuming that junction particles are spaced every 20 nm along a TJ strand, an average value in Figs. 13 and 17 of Orci et al. (1981). The pore could be formed by particle pairs in apposing membranes as shown in Fig. 3.4A or formed by the interstices of adjacent particles, as shown in Fig. 3.4B.

Recently, a dual pathway model for the TJ has been demonstrated for intestinal cell monolayers in vitro (Watson et al., 2001). PEGs (polyethylene glycols) of increasing radius are used as paracellular probes to detect the paracellular pathway in Caco-2 and T84 cell lines by measuring their permeability. A restrictive pore (radius 0.43-0.45 nm) and a nonrestrictive pore responsible for permeability of large molecules are found in both cell lines. A mathematical model was developed to analyze the permeability of different size PEGs. In that model, however, pore size was determined by considering only steric exclusion and the hydrodynamic resistance due to the pore walls was neglected.

The TJ strands may be viewed as chains of particles, with typical spacing of these particles, as seen in freeze-fracture electron micrographs, being of the order of 20 nm (Orci et al., 1981). These particles are thought to be the integral proteins of the claudin family and occludin (Furuse et al., 1993; Furuse et al., 1998A; Fanning et al., 1999). Occludin is believed to be a functional component of the TJ (McCarthy et al., 1996) and a

possible determinant of the TJ permeability in endothelial cells (Hirase et al., 1997). Claudin-1 and claudin-2 were the first members of the claudin family to be identified and could reconstitute TJ strands (Furuse et al., 1998A; Furuse et al., 1998B;). When claudin-2 is introduced into the Madin-Darby-Canine-Kidney I (MDCK-I) cells, a conversion from a very tight junction to a leaky junction is observed (Furuse et al., 2001). Claudin-1 and claudin-4 are abundant in MDCK-I cells which have very "tight" junctions, while claudin-2 expression is found in MDCK-II cells which have a much leakier TJ than MDCK-I cells, although the number of strands in these two cell type is similar (Furuse et al., 2001). This suggests that claudin-2 could be responsible for the leakiness of the MDCK-II cells and the formation of small pores between apposing TJ strands. Indeed, when the claudins expressed in MDCK cells are selectively modified, the paracellular conductance of small electrolytes can be modulated, including the anion/cation selectivity preference (Colegio et al., 2002). Claudin-2 exists throughout the proximal tubule and in a contiguous early segment of the thin descending limb of long-looped nephrons in mouse kidney (Enck et al., 2001). Thus, claudin-2 may be a key component of the paracellular pores in the TJ of the mouse proximal tubule and the integral protein responsible for its leaky permeability properties for small ions. Homotypic interactions between claudin-2 in apposing TJ strands or heterotypic interactions between claudin-2 and claudin-1 are possible candidates for the small circular pores in the present model (Furuse et al., 1999).

Relation to prior theory

The picture of proximal tubule water flow provided by this analysis is different in several important ways from the view derived from the compartment model of Weinstein (1984). These differences are featured in Tables 3.2 and 3.3. In this model, the tight junction water permeability is only 6.3% or (0.336/5.314) that of the cellular pathway, although L_{TJ} is 21.2 percent of L_P, and the tight junction reflection coefficient is near zero. This means that even with a hypertonic lateral interspace, there will be little transjunctional flux of water. In Weinstein (1984), the water permeabilities of cell and junction were nearly equal, and small increases in interspace salt concentration could drive large transjunctional water flows. Thus, in the present model, the composite luminal membrane reflection coefficient (σ_M) is substantially higher than that used previously. This occurs despite the fact that the overall salt reflection coefficients, σ=0.68, are the same for both models. Here, the constraint on the overall reflection coefficient is accommodated by virtue of the smaller basement membrane solute permeability, and thus more solute polarization within the lateral interspace. The departure from previous parameters is mandated by the assumed pore structure, and the obligation that a large non-discriminatory water pore has a high solute permeability. In the present model, we have fashioned what seems to be the largest tight junctional water flow possible, and this still yields a high composite luminal reflection coefficient.

One difficulty with the present dual pore/slit formulation, however, is that there is no apparent way to accommodate the finding of substantial differences among the ionic reflection coefficients. The careful experiments of Fromter et al. (1973) provided values of 0.7, 0.5, and 1.0 for the overall reflection coefficients of Na^+, Cl^- and HCO_3^-. These differences in reflection coefficients were predicted to yield a force for proximal tubule

water reabsorption when luminal HCO_3^- concentrations are less than and Cl^- concentrations are greater than their concentration in peritubular fluid. These predictions were confirmed experimentally (Schafer et al., 1975). Although this is a nonelectrolyte pore/slit model, and the observations relate to ions, it is difficult to see how charge effects could turn the large pore into a discriminatory pathway for which small ions will have non-zero reflection coefficient. Indeed, one prediction from this model is that claudins impact only the small-pore properties (ionic conductance). To our knowledge, there have been no measurements of water permeability or reflection coefficients in cultured epithelia in which claudins have been modified. Our model suggests that modification of claudins should have little effect on the water transport pathway. In sum, the very small reflection coefficient of the tight junction is a major difference with the earlier work (Weinstein, 1984), but was necessary to bring this model into compatibility with pore theory. Weinstein's choice of reflection coefficient did attempt to satisfy compatibility with measured ionic reflection coefficients. Unfortunately, the means to reconciling these two constraints is not apparent. Despite this limitation, the added flexibility of the present model provides an approach that fits conceptually into recent views of the molecular structure of the TJ strands and the junction particle patterns observed in freeze-fracture electron micrograph studies of the TJ complex.

Table 3.1 Compatible pore radius (R_P) or half slit height (W/2) for solute pairs and their corresponding water permeability (L_{TJ}) based on a single pore model (A) or a single slit model (B).

(A)

Solute pair	R_P (nm)	A_P/δ (cm^{-1})	$L_{TJ} \times 10^3$ (cm/s)
Mannitol/NaCl	0.80	14.1	2.31
Sucrose/ NaCl	0.95	12.1	2.77
Mannitol/sucrose	1.41	3.50	1.78
Preisig and Berry (1985)	1.40	3.56	1.8

(B)

Solute pair	W/2 (nm)	A_l/δ (cm^{-1})	$L_{TJ} \times 10^3$ (cm/s)
Mannitol/ NaCl	0.457	12.6	1.79
Sucrose/ NaCl	0.552	10.8	2.25
Mannitol/sucrose	0.769	3.19	1.29
Preisig and Berry (1985)	0.800	3.16	1.40

Table 3.2 (A) Parameter values used in the compartment model

	Parameters In Weinstein (1984)	Parameters In Present Model
C_0 (mOsm)	290	290
Viscosity μ (Pa·s)		7×10^{-4}
Temperature (^{0}K)		310.15
N (active transport flux) (10^{-6} mmol/s/cm^2 epithelium)	18.5	18.5
H_C (10^{-10} cm/s)	3.1	3.1
σ_C	1	1
σ_B	0	0
C* (mOsm)	5.94	5.94
Lp (transepithelial water permeability) (10^{-7} cm/s/mmHg)	2.40	1.59
H (transepithelial NaCl permeability) (10^{-5} cm/s)	22.0	22.0
σ (transepithelial reflection coefficient for NaCl)	0.68	0.68
H_{TJ} (TJ NaCl permeability) (10^{-5} cm/s)	13.0	13.0

Table 3.2 (B) Parameter values used in the dual pathway model for the ultrastructure of the tight junction strands

Parameter	
NaCl radius (nm)	0.147
Mannitol radius (nm)	0.360
Sucrose radius (nm)	0.460
D_{free} (10^{-5} cm^2/s) for NaCl	2.21
D_{free} (10^{-5} cm^2/s) for mannitol	0.90
D_{free} (10^{-5} cm^2/s) for sucrose	0.70
H_{TJ} for NaCl (10^{-5} cm/s)	13.0
H_{TJ} for mannitol (10^{-5} cm/s)	0.87
H_{TJ} for sucrose (10^{-5} cm/s)	0.43
δ_1 (nm), large slit depth	100
δ_2 (nm), small pore depth	10
*S (luminal surface of rat proximal tubule) (μm^2/mmtubule)	96,000
*L (the total TJ length of rat proximal tubule) (mm/mmtubule)	68.8

* from Maunsbach and Christensen (1992).

Table 3.3 (A) Predicted values in the compartment model

	Parameters In Weinstein (1984)	Results in Present model
σ_M (composite membrane reflection coefficient)	0.84	0.94
H_M (composite membrane NaCl permeability) (10^{-5} cm/s)	27	30.5
H_B (basement membrane NaCl permeability) (10^{-5} cm/s)	117	79.3
L_{MB} (10^{-7} cm/s/mmHg)	7.2	5.7
σ_{TJ} for NaCl	0.65	0.0079
L_{TJ} (10^{-7} cm/s/mmHg)	3.7	0.34
L_C (10^{-7} cm/s/mmHg)	4.3	5.3

Table 3.3 (B) Predicted results in the dual pathway model for the ultrastructure of the tight junction strands

	Predicted values
W_1 (nm)	19.6
A_1/δ_1 (cm^{-1})	0.525
R_2 (nm)	0.668
A_2/δ_2 (cm^{-1})	15.8
f_1 ($\times 10^{-4}$)	3.75
λ_2 (nm)	20.2
σ_1	0.000226
σ_2	0.153
L_1(Water)	95.0%
L_2(Water)	5.0%
H_1(Salt)	8.7%
H_2(Salt)	91.2%
H_1(Sucrose)	78.3%
H_2(Sucrose)	21.7%
H_{TJ}(Mannitol) (10^{-5} cm/s)	0.89
H_1(Mannitol)	49.2%
H_2(Mannitol)	50.8%

Table 3.4 (A) Dual pathway model predictions obtained by varying C* and L_P but holding σ_{TJ}~0.0078

$L_P(10^{-7}$ cm/s/mmHg)	1.52	1.65
C* (mOsm)	8.00	4.00
$L_{TJ}(10^{-7}$ cm/s/mmHg)	0.331	0.341
σ_{TJ}	0.00783	0.00772
W_1 (nm)	19.8	19.8
A_1/δ_1 (cm^{-1})	0.507	0.519
R_2 (nm)	0.685	0.673
A_2/δ_2 (cm^{-1})	15.4	15.7
f_1 ($\times 10^{-4}$)	3.58	3.66
λ_2 (nm)	21.85	20.73
σ_1	0.000222	0.000220
σ_2	0.147	0.151
L_1(Water)	94.8%	95.0%
L_2(Water)	5.2%	5.0%
H_1(Salt)	8.4%	8.6%
H_2(Salt)	91.5%	91.3%
H_1(Sucrose)	75.5%	77.4%
H_2(Sucrose)	24.5%	22.6%
H_{TJ}(Mannitol) (10^{-5} cm/s)	0.92	0.90

Table 3.4 (B) Dual pathway model predictions obtained by decreasing σ_{TJ} and requiring C*=5.94 mOsm.

C* mOsm)	5.94	5.94	5.94	5.94	5.94
σ_{TJ}	0.0304	0.0136	0.00840	0.00771	0.00666
L_P (10^{-7} cm/s/mmHg)	1.595	1.590	1.5885	1.5883	1.5880
L_{TJ}(10^{-7} cm/s/mmHg)	0.352	0.340	0.336	0.335	0.335
W_1 (nm)	17.5	17.4	18.8	19.0	29.5
A_1/δ_1 (cm^{-1})	0.679	0.680	0.569	0.505	0.227
R_2 (nm)	0.313	0.440	0.624	0.685	0.848
A_2/δ_2 (cm^{-1})	88.0	31.7	17.2	15.4	12.8
f_1 ($\times 10^{-4}$)	5.40	5.46	4.22	3.54	1.08
λ_2 (nm)	0.797	4.37	16.3	21.9	40.2
σ_1	0.00028	0.00029	0.00024	0.00022	0.0001
σ_2	0.517	0.310	0.173	0.147	0.100
L_1(Water)	94.2%	95.7%	95.3%	94.9%	93.4%
L_2(Water)	5.8%	4.3%	4.7%	5.1%	6.6%
H_1(Salt)	11.1%	11.2%	9.4%	8.3%	3.8%
H_2(Salt)	86.6%	88.3%	90.4%	91.5%	96.1%
H_1(Sucrose)	100%	100%	84.5%	75.4%	65.0%
H_2(Sucrose)	0%	0%	15.5%	24.6%	35.0%
H_{TJ}(Mannitol)(10^{-5} cm/s)	0.56	0.63	0.83	0.92	1.17

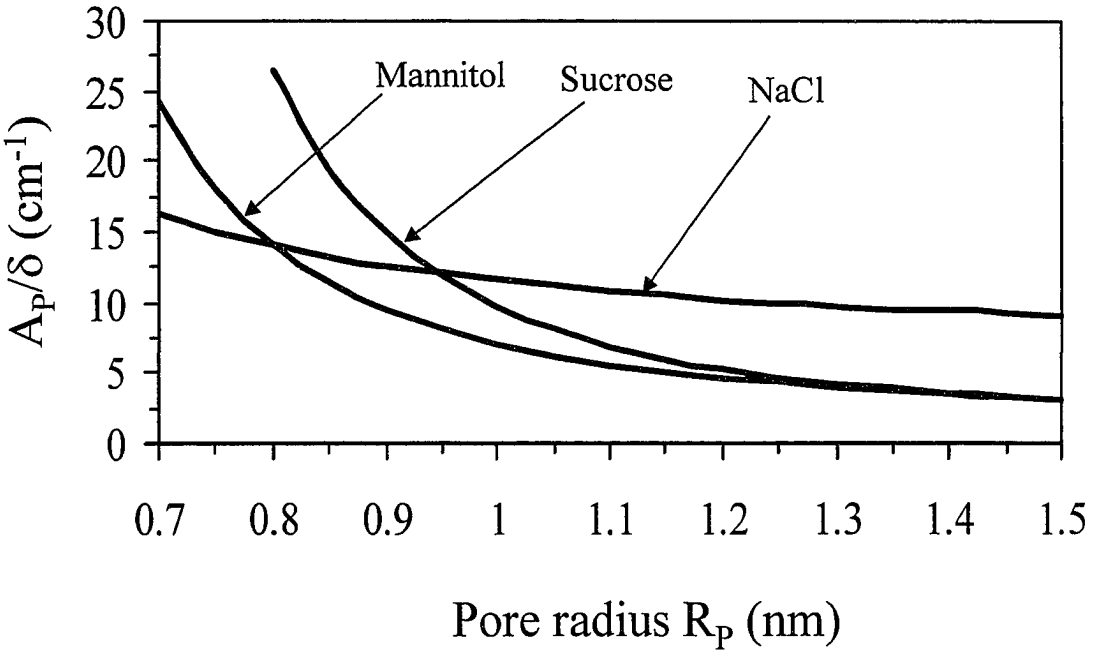

Figure 3.1 (A) Plot of equation (3.4) for A_P/δ (or H_{TJ}/D_{pore}) for NaCl, mannitol and sucrose as a function of pore radius. The compatible solutions for the mannitol/sucrose pair are 1.41nm, the NaCl/mannitol pair, 0.80nm, the NaCl/sucrose pair, 0.95nm.

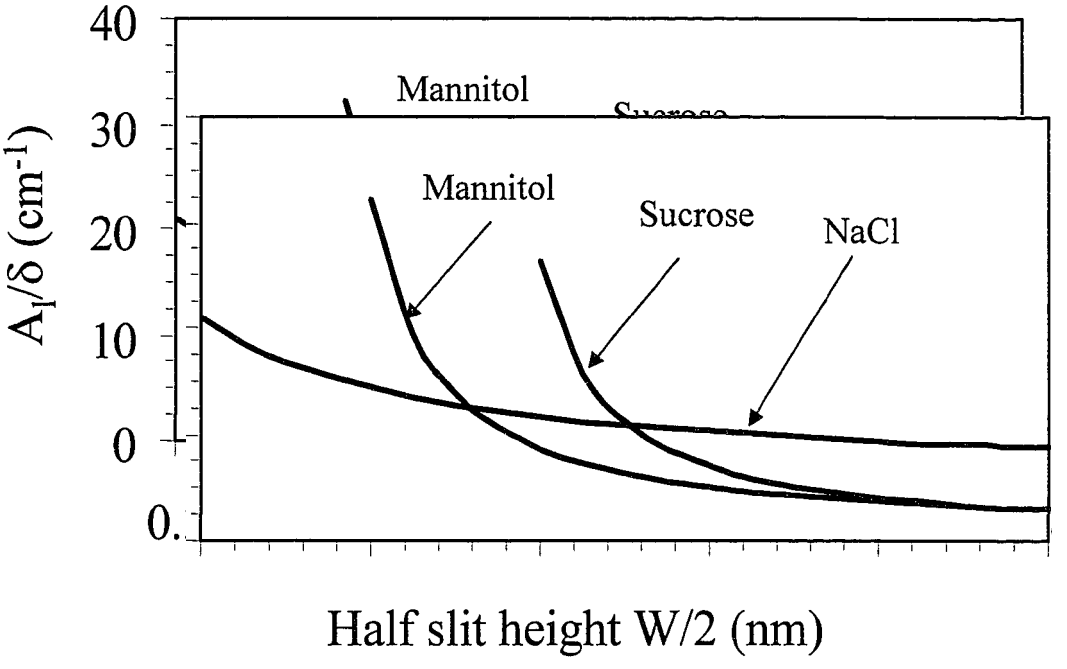

Figure 3.1 (B) Plot of equation (3.8) for A_I/δ (or H_{TJ}/D_{slit}) for NaCl, mannitol and sucrose as a function of half slit height. The compatible solution for the mannitol/sucrose pair is 0.77 nm, the NaCl/mannitol pair, 0.46nm, the NaCl/sucrose pair, 0.55nm.

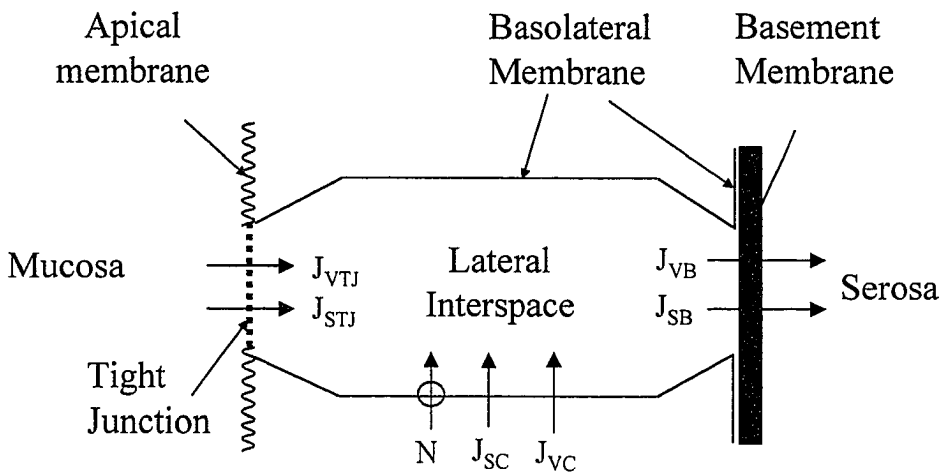

Figure 3.2 Compartment model for rat proximal tubule epithelium. The cell and the tight junction are in parallel and form a composite barrier. The cell barrier has the ability to actively transport sodium. This composite barrier is in series with the basement membrane. In our model, the reflection coefficient of the basement membrane for NaCl is zero and the water and solute permeability of the basement membrane is much larger than that of the composite luminal barrier.

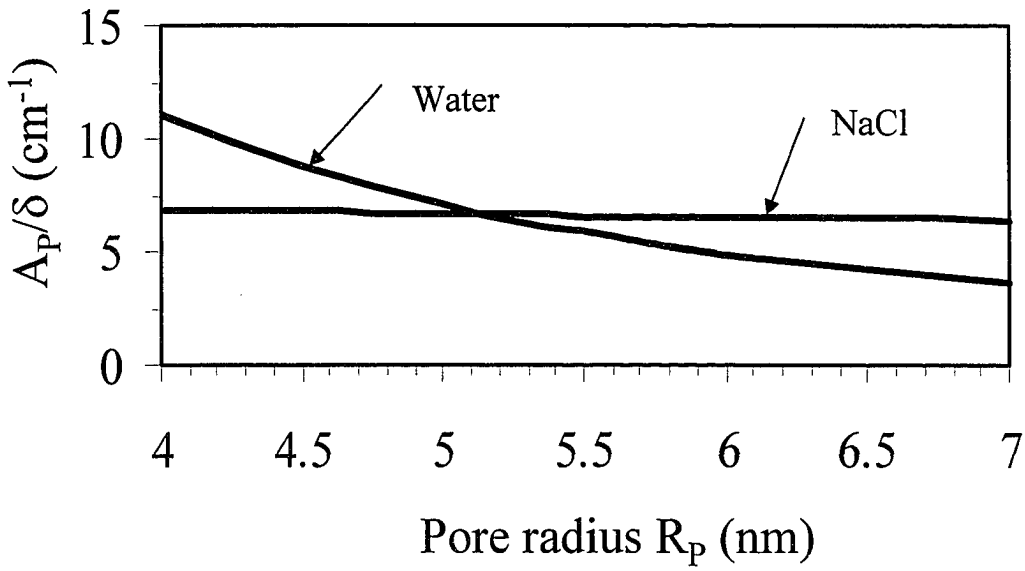

Figure 3.3 (A) Plot of equations (3.15a) and (3.15b) as a function of pore radius. The compatible pore radius is 5.17 nm. In calculation L_p=0.15 cm/s, σ=0.70, H_{TJ} =13 × 10^{-5} cm/s.

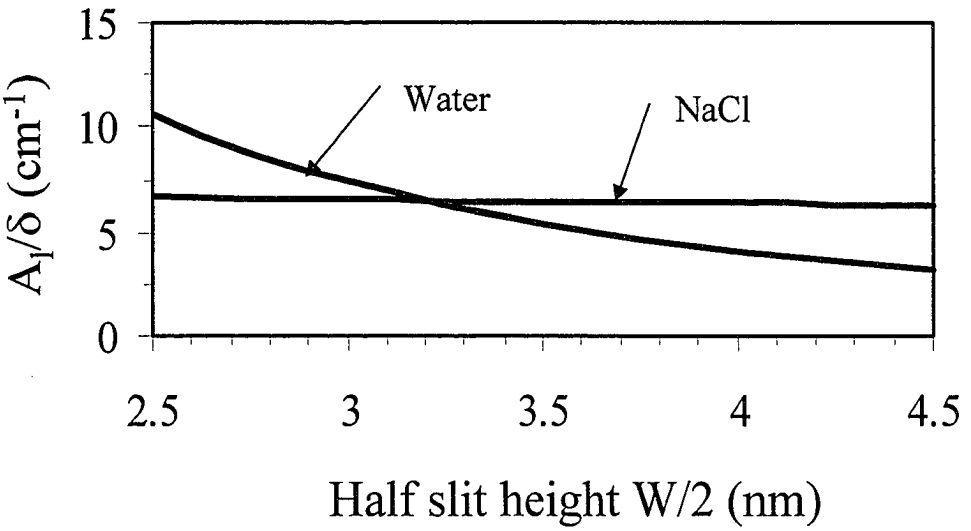

Figure 3.3 (B) Plot of equations (3.16a) and (3.16b) as a function of half slit height. The compatible half slit height is 3.2 nm. In calculation L_p=0.15 cm/s, σ=0.70, $H_{TJ}=13 \times 10^{-5}$ cm/s.

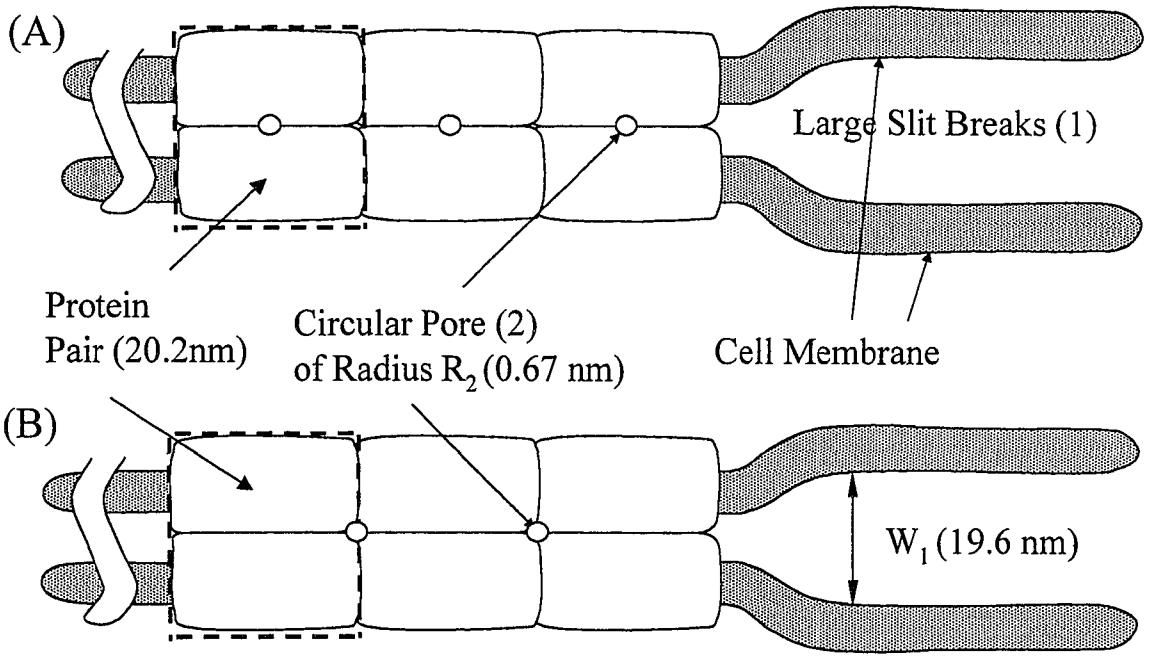

Figure 3.4 Two possible ultrastructural models for the TJ strand based on the present predictions of the dual pathway model. There are infrequent large slit breaks and numerous small circular pores associated with particle pairs in the TJ strand. The circular pore is either in the middle (A) or between two neighboring particle pairs (B). In the dual pathway model, there is one pore every 20 nm in the TJ strands. In this figure the particle spacing is assumed to be 20 nm.

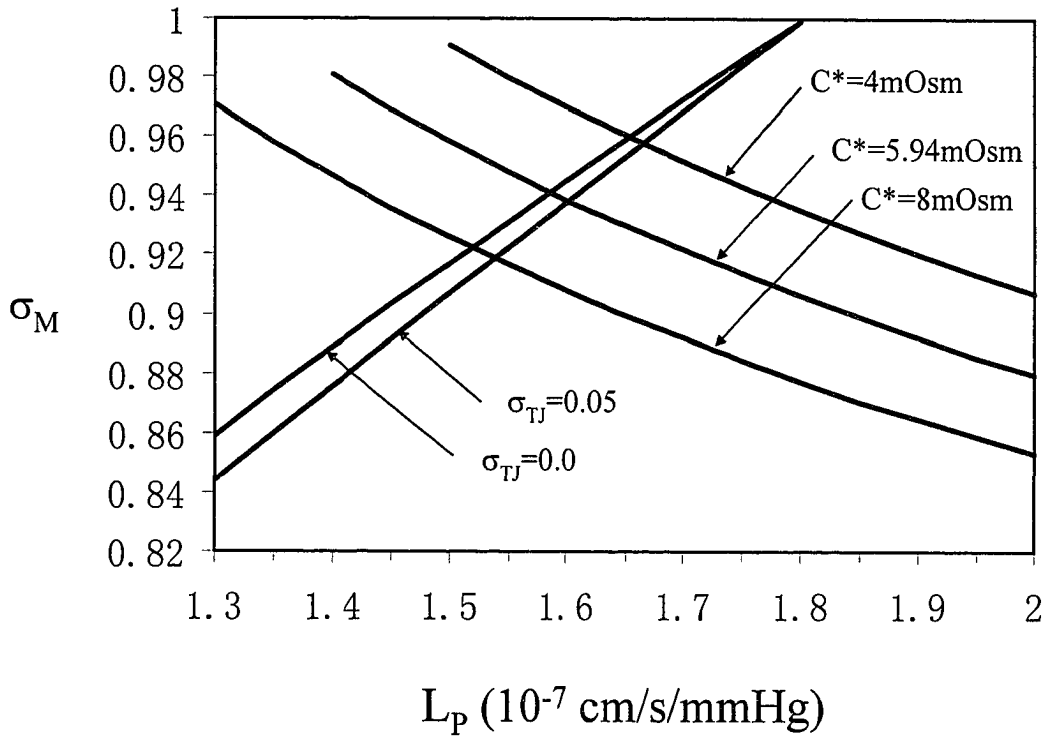

Figure 3.5 Relations between L_P and σ_M for three C* values, 4mOsm, 5.94 mOsm and 8 mOsm, and two σ_{TJ} values, 0.0 and 0.05. In this figure, the curves for two σ_{TJ} values intersect at a point where $L_P=1.8\times10^{-7}$ cm/s/mmHg and $\sigma_M=1.0$.

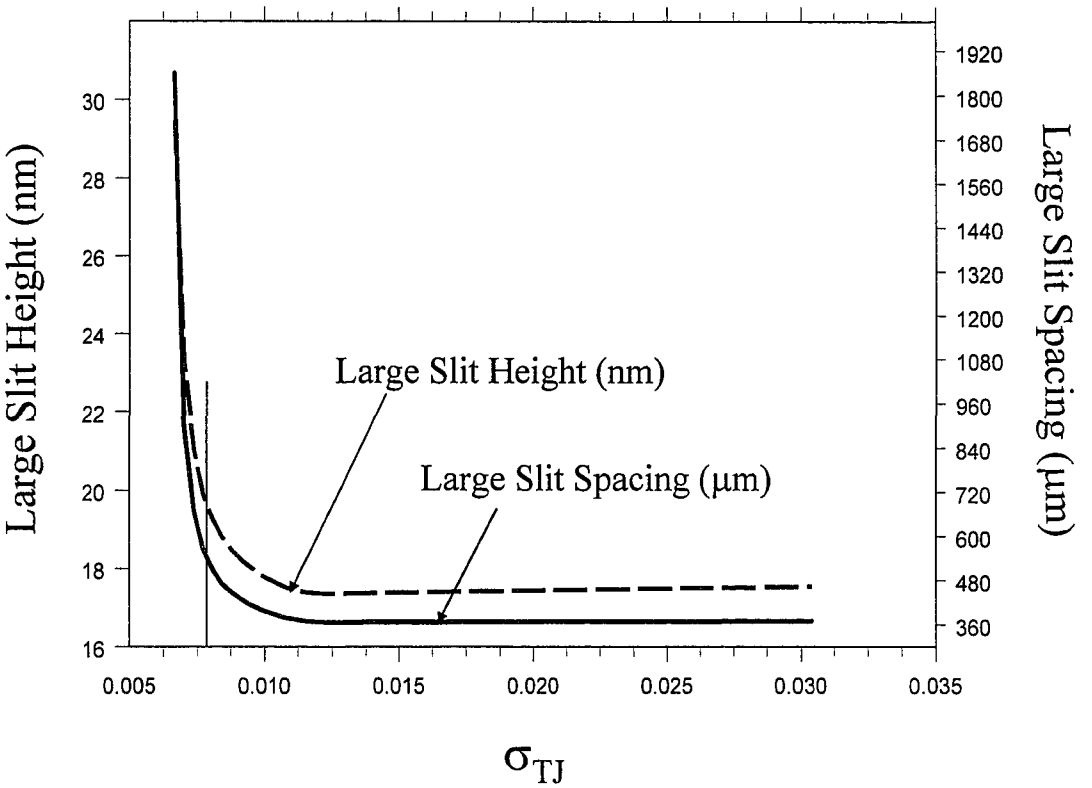

Figure 3.6 (A) Large slit height and spacing versus σ_{TJ}. The definition of large slit spacing is given in equation (3.49) where T=200nm.

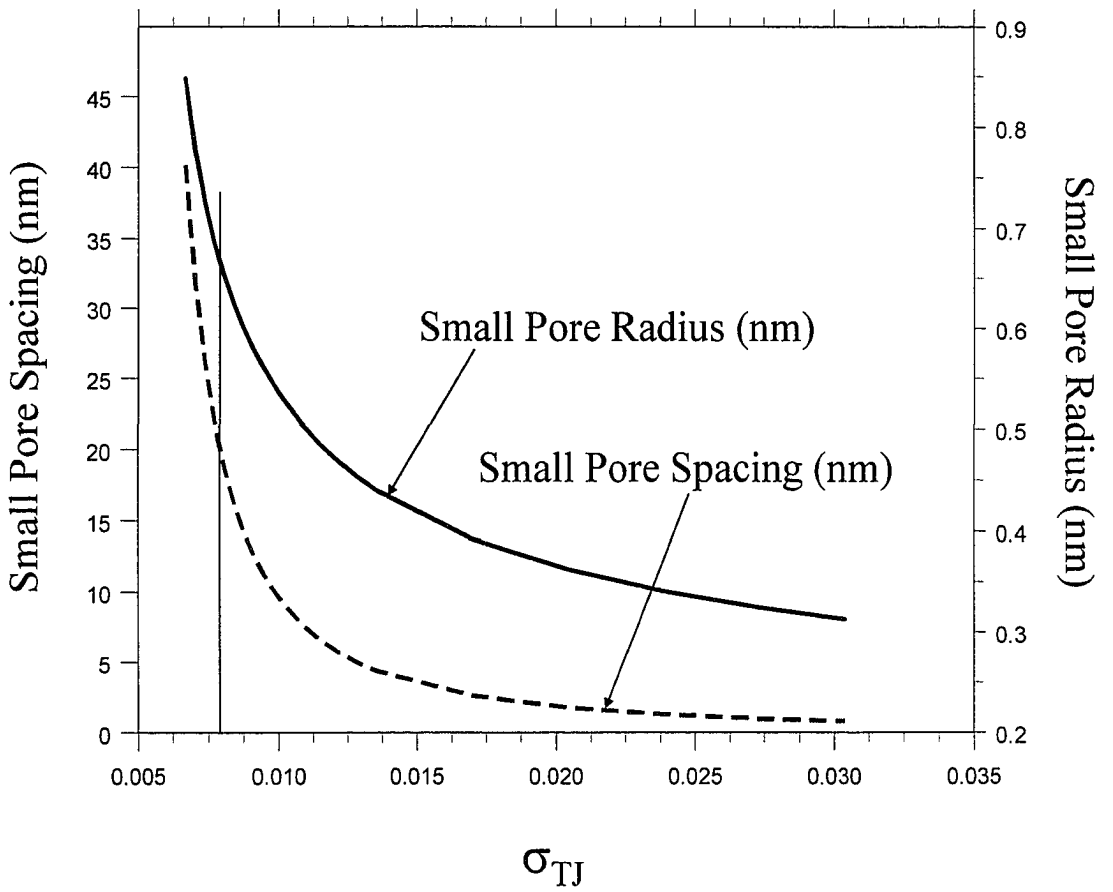

Figure 3.6 (B) Small pore radius and spacing versus σ_{TJ}.

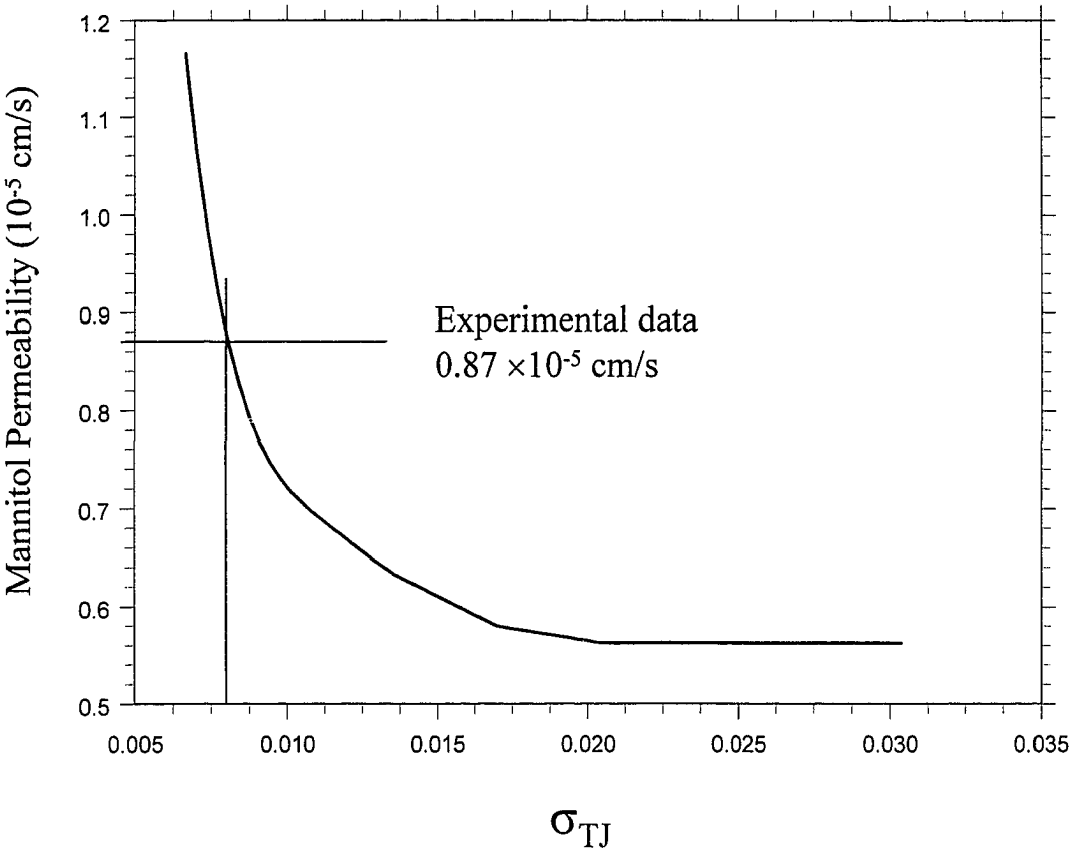

Figure 3.6 (C) Predicted mannitol permeability in the dual pathway model versus σ_{TJ}.

Chapter 4 Conclusion

In this dissertation we explored two long-standing mysteries in rat kidneys: the afferent mechanism in glomerulotubular balance and the contribution of the TJ to the total transepithelial water and solute transport. In Chapter 2 we proposed that the microvilli constituting the brush border in rat proximal tubule, from a mechanical viewpoint, are suitable for sensing the flow rate and converting this information into a cytoskeletal signal for reabsorption and, thus, capable of acting as mechanosensors. To examine this hypothesis quantitatively, we have developed an elastohydrodynamic model to predict the forces and torques along each microvillus and its resulting elastic bending deformation. This model indicates that: (1) the spacing of the microvilli is so dense that there is virtually no axial velocity within the brush border and that drag forces on the microvilli are at least 200 times greater than the shear force on the cell's apical membrane at the base of the microvilli; (2) of the total drag on a 2.5 micron microvillus, 74 percent appears within 0.2 microns from the tip; and (3) assuming that the structural strength of the microvillus derives from its axial actin filaments, then a luminal fluid flow of 30 nl/min produces a deflection of the microvillus tip which varies from about 1 to 5 percent of its 90 nm diameter depending on the microvilli length. The microvilli in this model appear as a set of stiff bristles, in a configuration in which changes in drag will produce maximal torque. Thus, the microvilli are physically suitable for sensing the flow rate and capable of serving as the afferent mechanism in glomerulotubular balance. This chapter has been published in Guo et al. (2000).

In this mechanosensory model we propose a new function for the microvilli in addition to amplify the reabsorption area for transport. This hypothesis is based on the observation that the brush border microvilli are of remarkable uniformity of length and of unusual hexagonal regularity in spacing. Such uniformity and regularity is not a prerequisite for a transport function. However, from a mechanical viewpoint, such uniformity and regularity would make sense if the microvilli were relatively stiff and acted as mechanotransducers to sense the flow rate in the tubule lumen. Another attractive feature of this new model is that it is able to take advantage of the large body of ultrastructural information that has been gathered over the past four decades, i.e. the ultrastructure of the epithelial cell in the proximal tubule, the ultrastructure of the actin filament bundle in the microvillus and the flow dependent geometry of the microvilli array. This information allows us to quantitatively examine the proposed new hypothesis in our elastohydrodynamic model in Chapter 2.

The total force acting on a single microvillus is rather small, see Table 2.1. Forces of the order of 0.01pN are too small to induce any biochemical responses. However, the total torque acting on a single microvilli varies from 9 pN·μm to 18 pN·μm depending on the flow rate, see Table 2.1. Torques of this order of magnitude can be found in the rotary motion of F1-synthase (40 pN·μm) or the sliding motion of actin filaments (5 pN·μm) (Noji et al., 1997; Suzuki et al., 1996). It is possible that such a torque acting on a single microvillus can be transmitted to the cortical cytoskeleton via the actin filaments in the terminal web, the initial step in triggering a biochemical response. There is also a 40 fold force amplification due to the resisting moment acting at the base of microvillus, see discussion in Chapter 2.

Brush border microvilli can be also found in mammalian small intestine. Superficially, there appears to be a close similarity between the brush border microvilli in the small intestine and the kidneys. Both have microvilli of roughly the same dimensions, 0.1 μm diameter and 2 μm length, which are arranged in a regular hexagonal array. However, from a structure-function viewpoint, the small intestine and the proximal tubule differ greatly although they have transport as their principal function. The microvilli on the apical surface of the epithelial cell of the intestinal villi are essentially shielded from the movement of the chime in the lumen of the intestine by the protruding villi, which are convoluted and themselves closely packed. The chime is driven by a slow peristaltic motion and it is only the digestive juices that slowly seep across the intestinal microvilli. The fact that the microvilli in the small intestine are shielded from flow makes it unlikely that these brush border microvilli function as flow stimulated mechanotransducers. This is pointed out in Weinbaum et al. (2001). In contrast to the microvilli in the small intestine, the microvilli in the proximal tubule are directly exposed to the fluid flow in the lumen of the convoluted proximal tubule.

There are also several structural differences between the brush border microvilli in the intestine and the kidney which strongly suggest a difference in function as a possible mechanotransducer. The actin filament bundle in the intestine is significantly stiffer (30 axial actin filaments compared to 6-10 in the rat kidneys), the microvilli are more closely spaced (nearly touching in the intestine compared to a 74 nm spacing at control flow conditions in the rat kidney) and the kidney epithelia have numerous clathrin coated pit regions which make for a more rigid supporting structure at the microvillus base (Rodman et al., 1986). The closely spaced microvilli in the intestine can easily touch

one another during peristaltic contractions, whereas the microvilli in the kidney, undergo only small non-contacting displacements at their tips.

Another ultrastructural feature observed on the luminal side of the small intestine is the glycocalyx. This layer is located at the luminal side of the brush border. It has many functions. It acts as a protective coating for cells exposed to deleterious environments (as is the case in the intestine) and also as an "ion trap" to mediate the steepness of the ionic gradient between the intracellular and extracellular environments. In small intestine the microvilli are thought to have some degree of enzymatic activity, and actually participate in digestion. In rat kidneys an irregular and amorphous cell coat can be observed to attach to the outer leaflet of the plasma membrane of the microvilli. These cell coats are neglected in the present mechanotransduction model for the brush border microvilli in Chapter 2 and are a possible direction of future research.

In Chapter 3 a dual pathway model is proposed for transport across the tight junction (TJ) strands in rat proximal tubule epithelium: large slit breaks formed by widely dispersed discontinuities in the TJ complex, and numerous small circular pores identified with the claudin-2 component of the TJ strand. This dual pathway model is developed as a new component of a compartment model for proximal tubule epithelium, Weinstein (1984), in order to provide a new ultrastructural view of the movement of water, ions, and nonelectrolyte solutes across proximal tubule. The model predicts the dimensions of both the large slit breaks and circular pores, which are required to satisfy estimates of TJ permeabilities. The predicted gap height of the large slit breaks is 19.6 nm and the predicted fraction of these breaks for a dual strand complex is only 0.04 percent of the

total length of the TJ in proximal tubule. The small pores are predicted to be circular pores with radius 0.668 nm that could be associated with the interstices between particle pairs in apposing TJ strands. On average there is one small pore every 20.2 nm along TJ strands. These numerous small, circular pores account for 91.2 percent of the TJ NaCl permeability, but only 5.0 percent of the TJ water permeability. The infrequent large slit breaks in the TJ strand account for 95.0 percent of the TJ water permeability, but only 8.7 percent of the TJ NaCl permeability. Small nonelectrolytes, such as sucrose and mannitol (4.6Å and 3.6 Å radius), can pass through both the large slit breaks and the small pores. For sucrose 78.3 percent of the transport is accommodated via the large slit breaks and 21.7 via the small pores. For mannitol, the transport is split nearly evenly between the two pathways, 50.8 and 49.2 percent. In the ultrastructural model developed herein, the water permeability of the TJ is 21.2 percent of the entire transepithelial water permeability and thus an order of magnitude greater than the single pore/slit theory results computed by Preisig and Berry (1985). The proposed dual pathway model for the TJ provides the first detailed ultrastructural model which reconciles the existence of the large slit breaks observed in the freeze-fracture electron microscopic pictures in Orci et al. (1981), and the latest information on the molecular structure of the TJ. However, it is difficult to see how to extend this model to accommodate the findings of substantial differences among the ionic reflection coefficient. This chapter has been published in Guo et al. (2003).

In Chapter 3 we first use a compartment model to provide an estimate of the TJ water permeability and the TJ reflection coefficient for small ions with a revised estimate for the transepithelial water permeability. The dual pore/slit pathway allows for a small

TJ reflection coefficient (0.008). This small TJ reflection coefficient is not included in the original compartment model of Weinstein (1984). A compatible transepithelial water permeability L_P, 1.59×10^{-7} cm/s/mmHg, is predicted in Fig 3.5 to satisfy both the requirements of a dual pathway model and the estimated active transport driving force. With this revised value for L_P, the compartment model predicts a TJ water permeability of 0.34×10^{-7} cm/s/mmHg, which is 21.2 percent of the transepithelial water permeability.

The value for the TJ water permeability predicted herein, 0.34×10^{-7} cm/s/mmHg (0.036cm/s), is close to the measured transepithelial water permeability (0.033cm/s) of isolated microperfused S2 segments of proximal tubule from AQP1 knockout mice (Schnermann et al., 1998). The measured value of the transepithelial water permeability of the same segment from wild mice is 0.15 cm/s, a value close to that used in the present study. Because AQP1 accounts for most of water transport via the transcellular route, the measured value in AQP1 knockout mice could primarily reflect the water permeability of the TJ. However, a quantitative model similar to the one developed in this study can not be applied because there is no available data for the transepithelial permeability and the transepithelial reflection coefficient for small ions in AQP1 knockout mice.

Another approach that could be used to predict the dimensions of the pore/slit in the proposed ultrastructural model is that instead of using the predicted water permeability of the TJ from the compartment model, additional solute permeability measurements can be used to determine the dimensions of the pores/slits in the TJ strands assuming that there is still a dual pore/slit pathway. These solutes could include mannitol and sucrose (Preisig and Berry, 1985) and sodium ions, as in the present study, plus chloride ions and urea (Green and Giebiesch, 1989) or other solutes. An important

extension of the present model would be to include the effect of charge. However, the predictive ability of the present model would be greatly limited if only small ions and small sized solutes are included in determination of the dimensions of the dual pore/slit pathway.

Although measured permeabilities for small solutes such as mannitol, sucrose, urea and ions such as sodium and chloride are available, there is little data for medium sized solutes. In our dual pathway model for the TJ in rat proximal tubule, there are two transport pathways in the TJ, large slit breaks and small circular pores. The predicted radius of the small circular pores is only 0.668 nm, a value too small to allow for the passage of medium sized solute (1 nm or so in radius). Thus, one expects that the large slit breaks will be the dominant pathway for these medium sized solutes. This can be inferred by the predicted results for sucrose transport. The large slit breaks account for 78.3 percent of the sucrose flux, while the small circular pores provide for the remaining 21.7 percent. Because the predicted gap height of the large slit breaks is 19.6 nm, a value much larger than the size of medium solute molecules, transport of medium sized solutes should occur as bulk flow within a limited transport area.

Recently, 24 polyethylene glycols (PEG) oligomers of increasing molecular radius (0.35-0.74nm) were used as paracellular probes to measure the solute permeability and functional TJ modeling in intestinal cell monolayers, Caco-2 and T84 cell lines, *in vitro* (Watson et al., 2001). These paracellular probes could possibly be used in the future to explore the solute permeability of rat proximal tubule. Another possible paracellular probe is ficoll (Ohlson et al., 2001). Ficoll is a spherical nonflexible molecular with no net molecular charge. Furthermore, the Stokes-Einstein radius for ficoll can vary from 1.2

to 7.2 nm. These paracellular probes could be used to provide the missing permeability data for medium sized solutes.

In Chapter 3 we proposed a dual pore/slit model to describe transport across the TJ complex based on the electron microscopic observations of the TJ. This model has provided greater flexibility in fitting the measured permeability data than either the fiber matrix model or the single pore/slit model, which we have shown are unable to reconcile the existing measured permeability data. The proposed dual pore/slit model, to my knowledge, is the first time that two different structures, small circular pores and large slit breaks, have been combined in a model for the TJ in rat proximal tubule. Furthermore, model calculations show that this dual pathway for the TJ is realistic and fits into both the TJ morphology observed in electron microscopic studies and recent views of the molecular structure of the TJ strands.

Two pore models have been used in the past to describe the glomerular barrier and the monolayers of cell lines from intestine (Katz et al., 1999; Watson et al., 2001). A two pore model was proposed in Watson et al. (2001) to explain the measured permeability data of PEG (24 ployethylene glycols) oligomers of different size in monolayers of Caco-2 and T84 cell lines. A model of equal or higher complexity was also used to describe the glomerular barrier, i.e., a two-pore-and-fiber matrix model (Katz et al., 1999). A two slit model was previously proposed to describe the TJ in capillary endothelium (Fu et al., 1994). However, the predicted dimensions of the small slits in that study were physically unlikely, because the small slit pathway formed a continuous slit of 2 nm gap height in the TJ strands surrounding the entire endothelial cell (Fu et al., 1998).

In summary, in this dissertation, we first propose a new function for brush border microvilli in rat proximal tubule, namely that they act as mechanosensors and can serve as the afferent mechanism in glomerulotubular balance, in addition to their widely accepted transport function. We have taken advantage of the existing large body of the ultrastructural information of the proximal tubule, the flow dependent geometry of the microvilli array and the ultrastructure of the actin filament bundle in the microvilli to quantitatively examine this hypothesis using a novel elastohydrodynamic model. This model demonstrates that the microvilli act as stiff bristles, produce a maximal torque and could convert flow information in the lumen into biochemical signals for reabsorption. We also show that the uniformity in microvilli length and the regularity of the microvilli array can be explained from a mechanical viewpoint if the microvilli are required to sense the flow rate and act as mechanosensors. We further suggest that the force or the torque acting on the terminal web may trigger the biochemical signaling required to activate the Na^+/H^+ transporters on the microvilli membrane to enhance sodium reabsorption and thus volume reabsorption. In Chapter 3 we proposed a dual pore/slit pathway for the TJ strands in rat proximal tubule and demonstrated that this dual pathway model has the ability to reconcile existing permeability measurements in rat proximal tubule. In order to determine the dimensions of the dual pathway, we adopt a compartment model with revised parameter values to provide an estimate of the TJ water permeability and the TJ reflection coefficient for salt. This leads to the conclusion that the water permeability of the TJ in the paracellular route contributes 21.2 percent of the total transepithelial water permeability. We then use these theoretically predicted values for TJ water permeability and TJ reflection coefficient for salt with the measured TJ permeability for sucrose and

small ions to determine the dimensions of the large slit breaks and small circular pores in the dual pathway. We find that these predictions fit conceptually into recent updated views of the molecular structure of the TJ strands and the junction particle patterns observed in freeze-fracture electron micrograph studies of the TJ complex.

Bibliography

1. Adamson RH, Liu B, Fry GN, Rubin LL and Curry FE. Microvascular permeability and number of tight junctions are modulated by cAMP. Am J Physiol 274:H1885-H1894, 1998.

2. Adamson RH and Michel CC. Pathways through the intercellular clefts of frog mensenteric microvessels, J. Physiol., (London), 466: 303-327, 1993.

3. Alpern RJ, Cogan MG and Rector FC Jr. Flow dependence of proximal tubular bicarbonate absorption. Am. J. Physiol. 245:F478-F484, 1983.

4. Bartoli E, Conger JD and Earley LE. Effect of intraluminal flow on proximal tubular reabsorption. J. Clin. Invest. 52:843-849, 1973.

5. Basmadjian D, Dykes DS and Baines AD. Flow through brush borders and similar protuberant wall structures. J. Membr. Biol. 56:183-190, 1980.

6. Beer FP and Johnston ER Jr. Mechanics of Material (2nd Ed.). New York: McGraw-Hill, 1992, p. 486.

7. Bendayan M. Ultrastructural localization of actin in muscle, epithelial and secretory cells by applying the protein A-gold immunocytochemical technique. Histochem. J. Jan:15(1); 39-58, 1983.

8. Berry CA. Water permeability and pathways in the proximal tubule, Renal fluid Electrolyte Physiol., 14, F279-294, 1983.

9. Bird R, Stewart W and Lightfoot E. Transport Phenomena. Wiley, New York, 1960.

10. Brenner BM, Falchuk KH, Keimowitz RI and Berliner RW. The relationship between peritubular capillary protein concentration and fluid reabsorption by the renal proximal tubule. J. Clin. Invest. 48:1519-1531, 1969.

11. Cantiello HF. Role of actin filament organization in cell volume and ion channel regulation. J. Exp. Zool. 279:425-435, 1997.

12. Chan YL, Biagi B and Giebisch G. Control mechanisms of bicarbonate transport across the rat proximal convoluted tubule. Am. J. Physiol. 242: F532-F543, 1982.

13. Claude P. Morphological factors influencing transepithelial permeability: a model for the resistance of the zonulae occludens. J. Membrane. Biol., 39: 219-232, 1978.

14. Claude P. and Goodenough D.A. Fracture faces of zonulae occludents from "tight" and "leaky" epithelia. J. Cell. Bio., 58: 390-400, 1973.

15. Colegio OR, van Itallie CM, McCrea HJ, Rahner C and Anderson JM. Claudins create charge-selective channels in the paracellular pathway between epithelial cells. Am J Physiol Cell Physiol 283:C142-C147, 2002.

16. Curran PF and MacIntosh JR. A model system for biological water transport. Nature, 193:347-348, 1962.

17. Curry FE and Michel CC. A fiber matrix model of capillary permeability, Microvasc. Res., 20, 96-99, 1980.

18. Davies PF. Flow-mediated endothelial mechanotransduction. Physiol. Rev. 75:519-560, 1995.

19. Dewey CF Jr. Bussolari SR, Gimbrone MA Jr. and Davies PF. The dynamic response of vascular endothelial cells to fluid shear stress. J. Biomech. Engr. 103:177-85, 1980.

20. Diamond JM. The mechanism of isotonic water transport. J. Gen. Physiol., 48:15-42, 1964.

21. Dupuis DE, Guilford WH, Wu J and Warshaw DM. Actin filament mechanics in the laser trap. J. Muscle Res. Cell Motil., 18:17-30, 1997.

22. Earley LE and Schrier RW. Intrarenal control of sodium excretion by hemodynamic and physical factors. In: Handbook of Physiology. Section 8:Renal Physiology, edited by J. Orloff and R.W. Berliner, pp. 721-762. American Physiological Society, Washington, D.C., 1973.

23. Ebnet K, Suzuki A, Horikoshi Y, Hirose T, Meyer Zu Brickwedde MK, Ohno S and Vestweber D. The cell polarity protein ASIP/PAR-3 directly associates with junctional adhesion molecule (JAM). EMBO J., 20:3738-48, 2001.

24. Edwards A, Deen WM and Daniels BS. Hindered transport of macromolecules in isolated glomeruli. I. Diffusion across intact and cell-free capillaries. Biophys J., 72:204-13, 1997.

25. Enck AH, Berger UV and Yu AS. Claudin-2 is selectively expressed in proximal nephron in mouse kidney, Am. J Physiol: Renal Physiol., 281:F966-74, 2001.

26. Fanning AS, Mitic LL and Anderson JM. Transmembrane proteins in the tight junction barrier. J Am Soc Nephrol., 10:1337-45, 1999.

27. Fraser WD and Baines AD. Application of a fiber-matrix model to transport in renal tubules, J. Gen. Physio., 94, 863-879, 1989.

28. Fromter E. Solute transport across epithelia: What can we learn from micropuncture studies on kidney tubules? J Physiol (London) 288:1-31, 1979.

29. Fromter E, Rumrich G and Ullrich K. Phenomenologic Description of Na, Cl and HCO3 absorption from proximal tubules. Pf. Arch. 343:189-220, 1973.

30. Fu BM, Adamson RH and Curry FE. Test of a two-pathway model for small-solute exchange across the capillary wall. Am J Physiol., 274:H2062-73, 1998.

31. Fu BM, Weinbaum S, Tsay RY and Curry FE. A junction-orifice-fiber entrance layer model for capillary permeability: application to frog mesenteric capillaries. J Biomech Eng., 116:502-13, 1994.

32. Furukawa R and Fechheimer M. The structure, function and assembly of actin filament bundles. Int. Rev. Cytol., 175:29-90, 1997.

33. Furuse M, Fujita K, Hiiragi T, Fujimoto K and Tsukita S. Claudin-1 and -2: novel integral membrane proteins localizing at tight junctions with no sequence similarity to occludin. J Cell Biol., 141:1539-50, 1998A.

34. Furuse M, Furuse K, Sasaki H and Tsukita S. Conversion of zonulae occludentes from tight to leaky strand type by introducing claudin-2 into Madin-Darby canine kidney I cells, J Cell Biol., 153:263-72, 2001.

35. Furuse M, Hirase T, Itoh M, Nagafuchi A, Yonemura S, Tsukita S and Tsukita S. Occludin: a novel integral membrane protein localizing at tight junctions, J Cell Biol., 123:1777-88, 1993.

36. Furuse M, Sasaki H, Fujimoto K and Tsukita S. A single gene product, claudin-1 or -2, reconstitutes tight junction strands and recruits occludin in fibroblasts, J Cell Biol., 43:391-401, 1998B.

37. Furuse M., Sasaki H. and Tsukita S. Manner of interaction of heterogeneous claudin species within and between tight junction strands. J. Cell Bio., 147: 891-903, 1999.

38. Gao L, Joberty G and Macara IG. Assembly of epithelial tight junctions is negatively regulated by Par6. Curr Biol., 12:221-5, 2002.

39. Gertz KH and Boylan JW. Glomerular-tubular balance. In: Handbook of Physiology. Section 8:Renal Physiology, edited by J. Orloff and R.W. Berliner, pp. 763-790. American Physiological Society, Washington, D.C., 1973.

40. Gittes F, Micky B, Nettleton J and Howard J. Flexural rigidity of microtubules and actin filaments measured from thermal fluctuation in shape. J. Cell. Biol. Vol. 120, Number 4, 923-934, Feb. 1993.

41. Green R and Giebisch G. Reflection coefficients and water permeability in rat proximal tubule. Am. J. Physiol., 257: F658-668, 1989.

42. Green R, Giebisch G, Unwin R and Weinstein, AM. Coupled water transport by rat proximal tubule. Am J Physiol 261:F1046-F1054, 1991.

43. Green R, Moriarty RJ and Giebisch G. Ionic requirements of proximal tubular fluid reabsorption: Flow dependence of fluid transport. Kidney Int. 20:580-587, 1981.

44. Green R, Windhager EE and Giebisch G. Protein oncotic pressure effects on proximal tubular fluid movement in the rat. Am. J. Physiol. 226:265-276, 1974.

45. Guo P, Weinstein AM and Weinbaum S. A hydrodynamic mechanosensory hypothesis for brush border microvilli. Am J Physiol Renal Physiol. 279:F698-712, 2000.

46. Guo P, Weinstein AM, Weinbaum S. A dual-pathway ultrastructural model for the tight junction of rat proximal tubule epithelium. Am J Physiol Renal Physiol., 285:F241-257, 2003.

47. Haberle DA, Shiigai TT, Maier G, Schiffl H and Davis JM. Dependency of proximal tubular fluid transport on the load of glomerular filtrate. Kidney Int. 20:18-28, 1981.

48. Haberle DA and von Baeyer H. Characteristics of glomerulotubular balance. Am. J. Physiol. 244: F355-F366, 1983.

49. Hassen OE and Hermann L. The presence of an axial structure in the microvillus of the mouse convoluted proximal tubule cell. Lab. Invest. 11:610-616, 1962.

50. Heiskala M, Peterson PA and Yang Y. The roles of claudin superfamily proteins in paracellular transport. Traffic. 2:93-8, 2001.

51. Hirase T, Staddon JM, Saitou M, Ando-Akatsuka Y, Itoh M, Furuse M, Fujimoto K, Tsukita S and Rubin LL. Occludin as a possible determinant of tight junction permeability in endothelial cells, J Cell Sci., 110 :1603-1613, 1997.

52. Hu XP and Weinbaum S. A new view of starling's hypothesis at the microstructural level, Microvascular Research, 58, 281-304, 1999.

53. Kamiya A, Bukhari R and Togawa T. Adaptive regulation of wall shear stress optimizing vascular tree function. Bull. Math. Biol. 46: 127-137, 1984.

54. Katz MA, Schaeffer RC Jr., Gratrix M, Mucha D and Carbajal J. The glomerular barrier fits a two-pore-and fiber-matrix model: derivation and physiologic test, Microvascular Research, 57:227-243, 1999.

55. Kaysen JH, Campbell WC, Majewski RR, Goda FO, Navar GL, Lewis FC, Goodwin TJ and Hammond FO. Select de novo gene and protein expression during renal epithelial cell culture in rotating wall vessels is shear dependent. J. Membr. Biol. 168:77-89, 1999.

56. Kedem O. and Leaf A. The relation between salt and ionic transport coefficients. J Gen Physiol 49:655-662, 1966.

57. Kishino A and Yanagida A. Force measurements by micro manipulation of a single actin filament by glass needles. Nature. 334: 74-76, 1988.

58. Knight TF, Senekjian HO, Sansom SC and Weinman EJ. Proximal tubule glucose efflux in the rat as a function of delivered load. Am. J. Physiol. 238: F499-F503, 1980.

59. Knox FG and Haas JA. Factors influencing renal sodium reabsorption in volume expansion. Rev. Physiol. Biochem. and Pharm. 92:75-113, 1982.

60. Knox FG, Mertz JI, Burnett JC Jr. and Haramati A. Role of hydrostatic and oncotic pressures in renal sodium reabsorption. Circ. Res. 52:491-500, 1983.

61. Krahn TA and Weinstein AM. Acid/base transport in a model of the proximal tubule brush border: impact of carbonic anhydrase. Am. J. Physiol. 270: F344-F355, 1996.

62. Kurashima K, D'Souza S, Szaszi K, Ramjeesingh R, Orlowski J and Grinstein S. The apical Na^+/H^+ exchanger isoform NHE3 is regulated by the actin cytoskeleton. J. Biol. Chem. 274(42): 29843-29849, 1999.

63. Kwon TH, Hager H, Nejsum LN, Andersen ML, Frokiaer J and Nielsen S. Physiology and pathophysiology of renal aquaporins. Semin Nephrol., 21:231-238, 2001.

64. Lamprecht G, Weinman EJ and Yun C-HC. The Role of NHERF and E3KARP in the cAMP-mediated inhibition. J. Biol. Chem. Nov.6. vol. 273 (45):29972-8, 1998.

65. Larson RE and Higdon JJL. Microscopic flow near the surface of two-dimensional porous media. Part 2: Transverse flow. J. F. M. 178: 119-136, 1987.

66. Lehoux S, Tronc F and Tedgui A. Mechanisms of blood flow-induced vascular enlargement. Biorheology, 39:319-324, 2002.

67. Lewy JE and Windhager EE. Peritubular control of proximal tubular fluid reabsorption in the rat kidney. Am. J. Physiol. 214:943-954, 1968.

68. Linshaw MA, Fogel CA, Downey GP, Koo EWY and Gotlieb AI. Role of cytoskeleton in volume regulation of rabbit proximal tubule in dilute medium. Am. J. Physiol. 262: F144-F150, 1992.

69. Liu F-Y and Cogan MG. Flow dependence of bicarbonate transport in the early (S1) proximal convoluted tubule. Am. J. Physiol. 254: F851-F855, 1988.

70. Louvard D. The function of the major cytoskeletal components of the brush border. Curr. Opin. Cell Biol., 1:51-57, 1989.

71. Ma TY, Hoa NT, Tran DD, Bui V, Pedram A, Mills S. and Merryfield M. Cytochalasin B modulation of Caco-2 tight junction barrier: role of myosin light chain kinase. Am J Physiol Gastrointest Liver Physiol., 279:G875-85, 2000A.

72. Ma TY, Tran D, Hoa N, Nguyen D, Merryfield M and Tarnawski A. Mechanism of extracellular calcium regulation of intestinal epithelial tight junction permeability: role of cytoskeletal involvement. Microsc Res Tech., 51:156-68, 2000B.

73. Maddox DA, Fortin SM, Tartini A, Barnes WD and Gennari FJ. Effect of acute changes in glomerular filtration rate on Na^+/H^+ exchange in rat renal cortex. J. Clin. Invest. 89:1296-1303, 1992.

74. Martin-Padura I, Lostaglio S, Schneemann M, Williams L, Romano M, Fruscella P, Panzeri C, Stoppacciaro A, Ruco L, Villa A, Simmons D and Dejana E. Junctional adhesion molecule, a novel member of the immunoglobulin superfamily that distributes at intercellular junctions and modulates monocyte transmigration. J Cell Biol., 142:117-27, 1998.

75. Maunsbach AB. Ultrastructure in the proximal tubule. In: Handbook of Physiology. Renal Physiology, edited by J. Orloff and R.W. Berliner and S.R. Geiger, Section 8, chapter 2, pp. 31-79. American Physiological Society, Washington, D.C., 1973.

76. Maunsbach AB and Christensen EI. Functional ultrastructure of the proximal tubule. Chapter 2 in Handbook of Physiology, Section 8: Renal Physiology, ed. by E.E. Windhager. New York, Oxford Univ. Press. p. 41-107, 1992.

77. Maunsbach AB, Giebisch GH and Stanton BA. Effects of flow rate on proximal tubule ultrastructure. Am. J. Physiol. 253: F582-F587, 1987.

78. McCarthy KM, Skare IB, Stankewich MC, Furuse M, Tsukita S, Rogers RA, Lynch RD and Schneeberger EE. Occludin is a functional component of the tight junction. J Cell Sci., 109:2287-2298, 1996.

79. Michel CC and Curry FE. Microvascular Permeability, Physiological Reviews, 79: 703-761, 1999.

80. Mokady AJ, Mestel AJ and Winlove CP. Flow through a charged biopolymer layer. J.F.M. vol383. pp. 353-378, 1999.

81. Mooseker MS and Tilney LG. Organization of an actin-filament-membrane complex. Filament polarity and membrane attachment in the microvilli of intestinal epithelial cells. J. cell Biol., 67:725-743, 1975.

82. Morita K, Furuse M, Fujimoto K and Tsukita S. Claudin multigene family encoding four-transmembrane domain protein components of tight junction strands. Proc. Natl. Acad. Sci., 96:511-6, 1999.

83. Moustakas A, Theodoropoulos PA, Gravanis A, Haussinger D and Stournaras C. The cytoskeleton in cell volume regulation. Contrib. Nephrol. 123:121-134, 1998.

84. Noji H, Yasuda R, Yoshida M and Kinosita K Jr. Direct observation of the rotation of F1-ATPase. Nature. 386:299-302, 1997.

85. Ohlson M, Sorensson J and Haraldsson B. A gel-membrane model of glomerular charge and size selectivity in series. Am. J. Physiol. Renal Physiol., 280:F395-F405, 2001.

86. Orci L, Humbert F, Brown D and Perrelet A. Membrane ultrastructure in urinary tubules, in: international review of cytology, edited by Bourne G.H., Danielli J.F. and Jeon K.W., volume 73, Academic press, New York, 1981.

87. Patrie KM, Drescher AJ, Welihinda A, Mundel P and Margolis B. Interaction of two actin-binding proteins, synaptopodin and alpha-actinin-4, with the tight junction protein MAGI-1. J Biol Chem., 277:30183-30190, 2002.

88. Pearce D and Verkman AS. NaCl reflection coefficients in proximal tubule apical and basolateral membrane vesicles. Measurement by induced osmosis and solvent drag. Biophys J 55:1251-1259, 1989.

89. Peterson OW, Gushwa LC and Blantz RC. An analysis of glomerular-tubular balance in the rat proximal tubule. Pf. Arch. 407:221-227, 1986.

90. Preisig PA. Luminal flow rate regulates proximal tubule H^+-HCO_3^- transporters. Am. J. Physiol. 262: F47-F54, 1992.

91. Preisig PA and Berry CA. Evidence for transcellular osmotic water flow in rat proximal tubule, Am J Physiol., 249:F124-131, 1985.

92. Richardson IW, Licko V, and Bartoli E. The nature of passive flows through tightly folded membranes. J. Membr. Biol. 11:293-308, 1973.

93. Rodman JS, Mooseker M and Farquhar MG. Cytoskeletal proteins of the rat kidney proximal tubule brush border. Eur J Cell Biol., 42:319-27, 1986

94. Romano G, Favret G, Federico E, and Bartoli E. The effect of intraluminal flow rate on glomerulotubular balance in the proximal tubule of the rat kidney. Exp. Physiol. 81:95-105, 1996.

95. Rostgaard J and Qvortrup K. Electron microscopic demonstrations of filamentous molecular sieve plugs in capillary fenestrae. Microvasc Research. 53:1-13, 1997.

96. Rostgaard J, and Thuneberg L. Electron microscopic observation the brush border of proximal tubule cells of mammalian kidney. Z. Zellforsch. 132:473-496, 1972.

97. Saitou M, Fujimoto K, Doi Y, Itoh M, Fujimoto T, Furuse M, Takano H, Noda T and Tsukita S. Occludin-deficient embryonic stem cells can differentiate into polarized epithelial cells bearing tight junctions. J Cell Biol., 141:397-408, 1998.

98. Sako Y, Nagafuchi A, Tsukita S and Kusumi A. Cytoplasmic regulation of the movement of E-cadherin on the free cell surface as studied by optical tweezers and single particle tracking: corralling and tethering by the membrane skeleton. J. Cell Biol. Mar. 9:140 (5): 1227-40, 1998.

99. Sangani AS and Acrivos A. Slow flow past periodic array of cylinders with application to heat transfer. J. Multiphase Flow. Vol 8 No.3 pp 193-206, 1982.

100. Satcher R. and Dewey JCF. Theoretical estimates of the mechanical properties of the endothelial cell cytoskeleton. Biophys. J. 71:109-118, 1996.

101. Schafer, J.A., Patlak, CS, and Andreoli, TE. A component of fluid absorption linked to passive ion flows in the superficial pars recta. J. Gen. Physiol., 66:445-471, 1975.

102. Schnermann J, Chou CL, Ma T, Traybor T, Knepper A and Verkman AS. Defective proximal tubule fluid reabsorption in transgenic aquaporin-1 null mice. Proc. Natl. Acad. Sci., 95:9660-9664, 1998.

103. Schnermann J, Wahl M, Liebau G and Fischbach H. Balance between tubular flow rate and net fluid reabsorption in the proximal convolution of the rat kidney. Pf. Arch. 304:90-103, 1968.

104. Simon DB, Lu Y, Choate KA, Velazquez H, Al-Sabban E, Praga M, Casari G, Bettinelli A, Colussi G, Rodriguez-Soriano J, McCredie D, Milford D, Sanjad S and Lifton RP. Paracellin-1, a renal tight junction protein required for paracellular Mg2+ resorption. Science. 285:103-106, 1999.

105. Suzuki N, Miyata H, Ishiwata S and Kinosita K Jr. Preparation of bead-tailed actin filaments: estimation of the torque produced by the sliding force in an in vitro motility assay. Biophys J., 70:401-408, 1996.

106. Tsay R-Y. and Weinbaum S. Viscous flow in a channel with periodic cross-bridging fibres: Exact solutions and Brinkman approximation. J. Fluid Mech. 226, 125-148, 1991.

107. Tsukita S and Furuse M. Pores in the wall: claudins constitute tight junction strands containing aqueous pores. J. Cell Bio., 149: 13-16, 2000.

108. Tsukita S and Furuse M. Occludin and claudins in tight-junction strands: leading or supporting players? Trends Cell Biol., 9:268-273, 1999.

109. Tsukita S and Furuse M. Overcoming barriers in the study of tight junction functions: from occludin to claudin. Genes Cells., 3:569-573, 1998.

110. Ullrich KJ. Permeability characteristic of the mammalian nephron, 1973. In: Handbook of Physiology. Section 8: Renal Physiology, edited by J. Orloff and R.W. Berliner, pp. 378-398, American Physiological Society, Bethesda.

111. Vallon V, Schwark JR, Richter K and Hropot M. Role of Na^+/H^+ exchanger NHE3 in nephron function: micropuncture studies with S3226, an inhibitor of NHE3. Am J Physiol Renal Physiol., 278:F375-379, 2000.

112. Van De Goot FG, Podevin RA and Corman BJ. Water permeabilities and salt reflection coefficients of luminal, basolateral and intracellular membrane vesicles isolated from rabbit kidney proximal tubule, Biochem. Biophys. Acta, 986, 332-340, 1989.

113. Walsh SV, Hopkins AM, Chen J, Narumiya S, Parkos CA and Nusrat A. Rho kinase regulates tight junction function and is necessary for tight junction assembly in polarized intestinal epithelia. Gastroenterology. 121:566-579, 2001.

114. Walsh SV, Hopkins AM and Nusrat A. Modulation of tight junction structure and function by cytokines. Adv Drug Deliv Rev., 41:303-313, 2000.

115. Watson CJ, Rowland M and Warhurst G. Functional modeling of tight junctions in intestinal cell monolayers using polyethylene glycol oligomers. Am J Physiol Cell Physiol., 281:C388-397, 2001.

116. Weinbaum S, Guo P and You L. A new view of mechanotransduction and strain amplification in cells with microvilli and cell processes. Biorheology. 38:119-142, 2001.

117. Weinstein AM. Chloride transport in a mathematical model of the rat proximal tubule. Am. J. Physiol. 263: F784-F798, 1992.

118. Weinstein AM. Glomerulotubular balance in a mathematical model of the proximal nephron. Am. J. Physiol. 258: F612-F626, 1990.

119. Weinstein AM. Convective paracellular solute flux: a source of ion-ion interaction in the epithelial transport equations, J Gen. Physiol., 89, 501-518, 1987.

120. Weinstein AM. Transport by epithelia with compliant lateral intercellular spaces: asymmetric oncotic effects across the rat proximal tubule, Am J Physiol., 247:F848-862, 1984.

121. Weinstein AM and Stephenson JL. Models of coupled salt and water transport across leaky epithelia, J membrane Biol., 60:1-20, 1981.

122. Welling LW and Grantham JJ. Physical properties of isolated perfused renal tubules and tubular basement membranes. J Clin Invest 51:1063-1075, 1972.

123. Welling LW and Welling DJ. Surface areas of brush border and lateral cell walls in the rabbit proximal tubule. Kidney Int. 8, 343-348, 1975.

124. Welling LW, Welling DJ, Holaspple JW and Evan AP. Morohometric analysis of distinct microanatomy near the base of proximal tubule cells, Am. J. Physiol.: Renal Fluid Electrolyte Physiol., 253:F126-F140, 1987.

125. Wilcox CS and Baylis C. Glomerular-tubular balance and proximal regulation. In: The Kidney. Physiology and Pathophysiology, edited by D.W. Seldin and G. Giebisch, pp. 985-1012. Raven Press, New York, 1985.

126. Wong KR, Berry CA and Cogan MG. Flow dependence of chloride transport in rat S1 proximal tubules. Am J. Physiol. 269:F870-F875, 1995.

127. Zarins CK, Zatina MA, Giddens DP, Ku DN and Glagov S. Shear stress regulation of artery lumen diameter in experimental atherogenesis. J. Vasc. Surg. 5:413-420, 1987.